

# **Study of Inhomogeneities in the Solar Atmosphere**

**A THESIS**

**Submitted for the award of Ph. D. Degree of  
MOHANLAL SUKHADIA UNIVERSITY**

**in the  
Faculty of Science  
by  
Brajesh Kumar**



**Under the Supervision of**

**Dr. K. Venugopalan  
Professor**

**DEPARTMENT OF PHYSICS  
FACULTY OF SCIENCE  
MOHANLAL SUKHADIA UNIVERSITY  
UDAIPUR**

**2007**

## DECLARATION

I hereby declare that the work incorporated in the present thesis entitled “**Study of Inhomogeneities in the Solar Atmosphere**” is my own work and is original. This work (in part or in full) has not been submitted to any University for the award of a Degree or a Diploma.

  
**Brajesh Kumar**

## CERTIFICATE

I feel great pleasure in certifying that the thesis entitled **“Study of Inhomogeneities in the Solar Atmosphere”** embodies a record of the results of investigation carried out by Brajesh Kumar under my guidance.

I am satisfied with the analysis of data, interpretation of results and conclusions drawn.

He has completed the residential requirement as per rules.



**Dr. K. Venugopalan**

**Professor**

Department of Physics,  
M. L. Sukhadia University,  
Udaipur – 313 002, INDIA.

**(Supervisor)**



**Dr. P. Venkatakrishnan**

**Senior Professor**

Udaipur Solar Observatory,  
Physical Research Laboratory,  
Dewali, Badi Road,  
Udaipur - 313 004, INDIA.

**(Co-Supervisor)**

## Acknowledgements

It is of great pleasure to thank my supervisors Prof. K. Venugopalan and Prof. P. Venkatakrishnan for their valuable guidance throughout this work. They have given me lots of encouragement and confidence in pursuing this thesis. Their aspiration to carry out excellent research work has always been a source of inspiration for me. It has been a great experience working with them. I express my sincere thanks to them for having given me this opportunity.

I thank the Director, Prof. J. N. Goswami, Physical Research Laboratory for providing me all the necessary facilities to carry out my thesis work.

I would like to express my gratitude to Dr. R. Sridharan and Mr. A. Raja Bayanna for fruitful discussions related to estimation of atmospheric “seeing” and development of solar adaptive optics system at Udaipur Solar Observatory (USO). I am also thankful to Dr. B. Ravindra for our collaborative work on flare related velocity flows.

Thanks to Prof. Ashok Ambastha, Dr. Nandita Srivastava, and Dr. Shibu Mathew of USO for their help at various stages of my thesis. I am also thankful to the faculty members and the staff of Department of Physics, University College of Science, and PG Studies Section of Mohan Lal Sukhadia University for their co-operation during my thesis work.

I am thankful to my colleagues Mr. Sanjay Gosain, Mr. A. Raja Bayanna and the research students, Mr. Nirvikar Dashora, Mr. Sanjeev Tiwari, Mr. Ram Ajor Maurya, Mr. Anand Joshi and Mr. Rohan Eugene Louis for their help and company at USO.

I express my sincere thanks to the all observing staff of USO, Mr. Laxmilal Suthar, Mr. Naresh Jain, Mr. Dalchand Purohit, and Mr. Jagdish Singh Chauhan for their cooperation in acquiring H-alpha data extensively used in this thesis for estimation of atmospheric “seeing”. I am also thankful to Mr. Tilak Joshi and Mr. Manish

Makwana for their help in these observations while they worked as Telescope Operator Trainee at USO.

The development of Image Stabilization System (ISS) for solar observations is a part of Adaptive optics (AO) system to be built for Multi-Application Solar Telescope (MAST) proposed for USO. I am thankful to Dr. R. Sridharan, Mr. A. Raja Bayanna, Dr. Shibu K. Mathew, Mr. Rohan Eugene Louis, Mr. Sudhir Gupta, and Late B. L. Paneri for sharing the different tasks related to the development of ISS under the valuable guidance of Prof. P. Venkatakrishnan. We all are thankful to Prof. C. U. Keller for sharing his expertise on AO system operational at Kitt Peak, NSO, USA. We are also thankful to Dr. K. S. N. Rao, CEERI, Pilani and Prof. A. R. Ganesan, Dept. of Physics, IIT, Chennai for visiting our lab and giving valuable suggestions for the improvement in our AO system.

I am deeply indebted to the SOHO/MDI teams for the use of their data. SOHO is a joint ESA and NASA program for international cooperation. I also wish to acknowledge the use of data from GOES, TRACE and RHESSI for studying the flare related velocity flows. The interesting results related to "Doppler ribbons" observed in SOHO/MDI Dopplergrams are complemented with the use of H-alpha data from ARIES, Nainital, India. I am very much thankful to Dr. Wahab Uddin and his colleagues for providing me these data for such an interesting study.

I thank the USO staff Mr. Raju Koshy, Mr. Rakesh Jaroli, Mr. C. P. Suthar, Mr. Sudhir Kumar Gupta, Mr. Naresh Jain, Late B. L. Paneri, Mr. Laxmilal Suthar, Mr. Dalchand Purohit, Mr. Shankarlal Paliwal, Mr. Jagadish Singh Chouhan and Mr. Ramachandra Carpenter for their help at various stages of my work.

Finally, this thesis is dedicated to my family. Without their encouragement and support, it would have been a difficult task to finish this thesis. I bow to the departed soul of my mother, who had been a source of great inspiration for me all the time.

  
**Brajesh Kumar**

# Contents

<b>List of Figures</b>	<b>iv</b>
<b>List of Tables</b>	<b>viii</b>
<b>Abstract</b>	<b>ix</b>
<b>1 Introduction</b>	<b>1</b>
1.1 The Inhomogenous Sun . . . . .	3
1.2 Observations of the evolution of inhomogeneities in the Sun . . .	6
1.3 Earth's atmospheric turbulence and astronomical seeing . . . . .	7
1.4 Adaptive optics for solar observations . . . . .	9
1.5 Motivation of the thesis . . . . .	10
<b>2 Estimation of atmospheric “seeing” using solar <math>H\alpha</math> images</b>	<b>12</b>
2.1 Introduction . . . . .	12
2.2 The observational data . . . . .	14
2.3 Analysis and Results . . . . .	15
2.4 Summary and Discussions . . . . .	22
<b>3 Development of an Image Stabilization System for solar ob- servations at Udaipur Solar Observatory</b>	<b>28</b>
3.1 Introduction . . . . .	28
3.2 Optical setup . . . . .	31
3.3 Overall description of the system . . . . .	33
3.3.1 Hardware . . . . .	34
3.3.1.1 Digital to analog converter . . . . .	34

3.3.1.2	Piezoelectric stage, its controller and mirror as- sembly . . . . .	34
3.3.1.3	Data acquisition system . . . . .	35
3.3.2	Software . . . . .	35
3.3.2.1	Universal tracker . . . . .	35
3.3.2.2	Control software . . . . .	38
3.4	Aperture size, system calibration and tuning . . . . .	39
3.4.1	Aperture size . . . . .	39
3.4.2	System calibration and tuning . . . . .	39
3.5	Results and Discussions . . . . .	44
3.5.1	G-band observations using the Image Stabilization System	46
3.5.2	Estimation of atmospheric “seeing” using G-band images	47
3.6	Limitations and Future plans . . . . .	50
<b>4</b>	<b>Analysis of enhanced velocity signals observed during solar flares</b>	<b>54</b>
4.1	Introduction . . . . .	54
4.2	The observational data . . . . .	56
4.3	Analysis and Results . . . . .	57
4.3.1	Space-time diagrams . . . . .	57
4.3.2	Power maps . . . . .	59
4.3.3	<i>rms</i> map of velocity signals . . . . .	65
4.4	Summary and Discussions . . . . .	70
<b>5</b>	<b>Signature of photospheric “Doppler ribbons” beneath <math>H\alpha</math> flare ribbons observed during an intense 4B/X17.2 solar flare</b>	<b>73</b>
5.1	Introduction . . . . .	73
5.2	The observational data . . . . .	74
5.2.1	SOHO/MDI data . . . . .	75
5.2.2	ARIES data . . . . .	75
5.3	Analysis and Results . . . . .	77

5.3.1	H $\alpha$ observations . . . . .	77
5.3.2	SOHO/MDI observations . . . . .	80
5.3.3	Correlation between SOHO/MDI observations and H $\alpha$ observations . . . . .	82
5.4	Discussions and Conclusions . . . . .	82
<b>6</b>	<b>Summary, Conclusions and Future plans</b>	<b>85</b>
6.1	Present Work . . . . .	86
6.1.1	Site characterization using solar H $\alpha$ images . . . . .	86
6.1.2	An Image Stabilization System for solar observations at USO . . . . .	89
6.1.3	Study of enhanced velocity signals observed during ma- jor solar flares . . . . .	91
6.1.4	First detection of photospheric “Doppler ribbons” during an intense 4B/X17.2 solar flare . . . . .	94
6.2	Future Directions . . . . .	95
6.2.1	High resolution observations with MAST and SOLAR-B/ Hinode . . . . .	95
	<b>Appendix:A</b>	<b>97</b>
	<b>Appendix:B</b>	<b>99</b>
	<b>Bibliography</b>	<b>101</b>
	<b>List of Publications</b>	<b>110</b>



# List of Figures

1.1	Butterfly diagram showing the positions of the sunspots for each rotation of the Sun since May 1874. . . . .	2
1.2	The image of white solar corona taken at High Altitude Observatory on 11 July 1991. . . . .	4
1.3	A series of soft X-ray images of the Sun showing the evolution of corona in X-ray with the solar cycle. . . . .	4
1.4	Extremely fine structure coronal arcade of loops observed by TRACE of a flaring solar active region. . . . .	5
1.5	A series of photospheric magnetograms of the Sun showing the evolution of longitudinal magnetic field with the solar cycle. . .	6
1.6	Velocity image obtained by SOHO/MDI showing the expanding solar quake associated with a large X-class flare. . . . .	11
2.1	The mean Wiener spectrum obtained from 100 short exposure (3 ms) $H\alpha$ (6563 Å) images. . . . .	16
2.2	Typical short exposure images of the Sun taken in $H\alpha$ line-center (6563 Å), blue wing (6563–0.5 Å), and red wing (6563+0.5 Å) of $H\alpha$ obtained at USO. . . . .	17
2.3	Plot showing the normalized atmospheric cut-off frequency ( $f_c$ ) for the burst of $H\alpha$ images taken at USO. . . . .	19
2.4	Plots showing the histogram distribution of $r_0$ for the years 2005 and 2006. . . . .	20
2.5	Plots showing the mean value of $r_0$ for each day for the years 2005 and 2006. . . . .	21

2.6	Plots showing the smoothed version of the mean seeing ( $\theta \approx \lambda/\text{mean}(r_0)$ ) for each day for the years 2005 and 2006. . . . .	23
2.7	Plot showing the quantity $\sqrt{\theta_{dry}^2 - \theta_{filled}^2}$ for each day for the years 2005 and 2006. . . . .	23
2.8	Plots showing the diurnal variation of seeing weighted by mean value of $r_0$ for each day for the years 2005 and 2006. . . . .	25
3.1	15 cm Zeiss Coudé Telescope being used as the light feed for prototype Adaptive optics system at USO. . . . .	32
3.2	Schematic of the optical layout inside the Adaptive optics laboratory. . . . .	33
3.3	Plots illustrating the components of image motion with the change in voltage applied to the channels of tip-tilt system . . .	40
3.4	Plots of image motion along $X$ axis in open and closed loop operations of the tip-tilt system. . . . .	44
3.5	Plots of image motion along $Y$ axis in open and closed loop operations of the tip-tilt system. . . . .	45
3.6	G-band observations of a sunspot (active region NOAA 10923) taken on 15 November 2006 using the Image Stabilization System of USO. . . . .	48
3.7	Plots showing the normalized atmospheric cut-off frequency ( $f_c$ ) for the burst of G-band images taken in open and closed loop observations. . . . .	49
3.8	Plot showing the relative improvement in speed of FFTW over FFT for various array sizes. . . . .	51
4.1	Space-time map showing the velocity fluctuations in and around active region NOAA 10486 on 28 October 2003. . . . .	58
4.2	Space-time map showing the velocity fluctuations in and around active region NOAA 10486 on 29 October 2003. . . . .	60
4.3	Space-time map showing the velocity fluctuations in and around active region NOAA 9415 on 6 April 2001. . . . .	61

4.4	Power maps in 2–4 mHz band computed from the SOHO/MDI Dopplergrams for 28 & 29 October 2003 and 6 April 2001 flare events. These are for before and spanning the flare. . . . .	62
4.5	Power maps in 5–6.5 mHz band computed from the SOHO/MDI Dopplergrams for 28 & 29 October 2003 and 6 April 2001 flare events. These are for before and spanning the flare. . . . .	63
4.6	RMS maps computed from the SOHO/MDI Dopplergrams for 28 & 29 October 2003 and 6 April 2001 flare events. These are for before and spanning the flare. . . . .	66
4.7	Plots showing the velocity signals of a single pixel obtained before, during and after the flare events of 28 & 29 October 2003 and 6 April 2001. . . . .	67
4.8	Contours of RHESSI hard X-ray flux in the range 100–300 keV and TRACE 1600 Å image overlaid upon the <i>rms</i> Doppler images of 28 & 29 October 2003 and 6 April 2001 flare events. . .	68
5.1	Sequence of H $\alpha$ filtergrams taken at ARIES showing the evolution of 4B flare in active region NOAA 10486 on 28 October 2003. . . . .	76
5.2	SOHO/MDI white light image overlaid with the contours of simultaneously observed longitudinal magnetic fields in the active region NOAA 10486 on 28 October 2003. . . . .	77
5.3	Sequence of SOHO/MDI Dopplergrams showing the signature of Doppler ribbons in the active region NOAA 10486 on 28 October 2003 during the impulsive phase of 4B/X17.2 flare event. . . .	78
5.4	Sequence of SOHO/MDI Dopplergrams overlaid with the H $\alpha$ flare intensity contours during the impulsive phase of 4B/X17.2 flare in the active region NOAA 10486 on 28 October 2003. . . .	79
5.5	H $\alpha$ filtergram obtained at ARIES showing the locations of flare kernels in the active region NOAA 10486 on 28 October 2003. .	80

5.6	Plots of Doppler velocity and H $\alpha$ relative intensity in the flare kernels depicted in Figure 5.5. . . . .	81
6.1	Block diagram of a feedback controller. . . . .	100

# List of Tables

3.1	Observed Bandwidth of 70–100 Hz for various runs in the two channels of the tip-tilt system during closed loop tracking of sunspots. . . . .	43
4.1	Details of the active regions and the X-ray class of the flares observed. . . . .	56

# Abstract

This thesis is based on a study of inhomogeneities in the solar atmosphere. The thesis consists of six chapters. The Chapter I is a brief introduction to the Sun's environment with an emphasis on the role of inhomogeneities in the dynamics of the solar atmosphere. The Sun can be observed from both, ground and space based telescopes. Space based observations are free from atmospheric effects; they are however expensive and short lived. Ground based facilities can stably operate for longer time and are convenient for future upgradations, apart from being less expensive relative to space based observational facilities. However, it is very necessary to develop proper observing techniques like adaptive optics to support the ground based observations in order to compensate the atmospheric effects. Thus, with the help of such observing facilities we can continuously monitor the dynamic activities of the Sun over several solar cycles with progressively improved techniques. This would refine our understanding of the physics involved in the various interesting solar phenomena and also help in precise Space Weather predictions.

The Chapter II is concerned with the measurement of atmospheric “seeing”, the so called ‘Fried’s parameter’. This parameter gives the quantitative measure of astronomical seeing of the given site and hence severely influences the quality of the recorded image in ground based observations, the larger its value, the better is the image quality. For this purpose, short exposure (3 ms) high resolution  $H\alpha$  (6563 Å) images of the Sun taken in burst mode with the 15 cm refractor Spar telescope located at the lake site of Udaipur Solar Observatory (USO) have been extensively used to quantify the seeing conditions prevailing at the lake site during the different months of the years 2005 and 2006. Spectral ratio technique (von der L  he, 1984) has been used to estimate the Fried’s parameter ( $r_0$ ) at this site. It is noteworthy to mention that the lake was dry during the observing period in 2005, while it overflowed during our observations in 2006 due to good monsoon rains. The seeing in the presence of water shows improvement in  $r_0$  by about 1.0 cm with respect to previous year’s

dry condition and mean  $r_0$  varies between 4.0–4.5 cm as evident from the data obtained between January–June, 2006. Thus, the episodic conditions of the lake provided an unique opportunity to study the atmospheric “seeing” in two different conditions. The estimates of  $r_0$  obtained in our analysis helped in determining the optimum size of the Multi-Application Solar Telescope (MAST) proposed for USO. It also helped in the design and development of a prototype Adaptive optics system at USO. Further, the long-term investigation of variation of  $r_0$  has shown that dome contributes to the degradation of “seeing” during the different epochs of the seasonal changes.

The Chapter III describes an Image Stabilization System (ISS) that has been developed and demonstrated for solar observations in the visible wavelength at USO with a 15 cm Coudé-refractor, which is the Phase I of the development of a low-order Adaptive optics system for the MAST at USO. Degradation of image quality at the focal plane of ground based telescopes due to atmospheric turbulence has been an important issue for astronomers. Adaptive optics is a technique exploited for the correction of such perturbations in real time thereby providing nearly stable images. Our ISS consists of a high speed camera (955 frames per second) and frame grabber system for sensing the overall tilt of the wave-front, a piezo-controlled mirror for correcting the tilt and an Intel Pentium 4 computer operating on Linux platform for controlling various devices. The software for operating the system is based on C-language. The first results indicating the capability of the system to limit the image motion within a fraction of the diffraction limit are presented. The system has a closed loop correction bandwidth in the range of 70 to 100 Hz. The root mean square image motion in the closed loop is about 0.1 arc-sec and is better than that in the open loop operation by a factor of 10 to 20. The hardware and software developments and key issues concerning optimum system performance have been addressed along with possible future improvements.

The Chapter IV is dedicated to the study of influence of solar flares on the velocity oscillations in the solar photosphere. The velocity oscillations appearing

on the solar surface are potential diagnostic tool for understanding the internal structure and dynamics of the Sun. Hence, it would be interesting to study the interaction of these velocity oscillations with the transient phenomenon, viz. flares taking place in the solar atmosphere. Solar flares are known to release large amount of energy. It is believed that the flares can excite velocity oscillations in active regions. We studied the changes in velocity signals in three active regions which have produced large X-class flares. The enhanced velocity signals appeared during the rise time of the GOES soft X-ray flux. These signals are located close to the vicinity of the hard X-ray source regions as observed with RHESSI. The power maps of the active region show enhancement in the frequency regime 5–6.5 mHz, while there is feeble or no enhancement of these signals in 2–4 mHz frequency band.

The Chapter V describes the first detection of photospheric “Doppler ribbons” associated with an intense 4B/X17.2 solar flare. The super active region NOAA Active Region 10486 which appeared on the solar disk in October 2003 produced lot of space weather related activity. This was one of the largest flares of solar cycle 23, which occurred near the Sun’s center and produced extremely energetic emission almost at all wavelengths from  $\gamma$ -ray to radio-waves. The flare was associated with a bright/fast-halo Earth directed CME, strong type II, type III and type IV radio bursts, and an intense radio burst. This flare was observed with space based solar Observatories viz., SOHO, TRACE and several other ground based Observatories including USO and ARIES in India in  $H\alpha$  wavelength. Here, we report the first detection of an interesting solar photospheric phenomenon, viz., “Doppler ribbons” or localized velocity enhancements, which were seen to accompany the solar chromospheric H-alpha ribbons during this super flare. These velocity enhancements exactly match the H-alpha brightness enhancements in space, and are delayed by approximately one minute in time. We interpret these Doppler enhancements as due to plasma shock being launched at the site of explosive chromospheric evaporation, which reaches the photosphere after approximately one minute. The



excitation of three minute oscillations in the photosphere after the flare, as discussed in the Chapter IV, is a clear signature of the response of the solar atmosphere to a pressure pulse in the form of a “wake”. Such Doppler ribbons have not been detected following weaker flares. Thus, the circumstance of the abnormally high electron flux available in the 4B/X17.2 flare of 28 October 2003, has given rise to this rare phenomenon.

In Chapter VI, the summary and conclusions of the present studies along with the direction of the future research work are presented. A detailed bibliography is also given in the end.

# Chapter 1

## Introduction

The Sun, the nearest star to our Earth, is known to be in existence for nearly 4.5 billion years. It has nurtured life on the planet Earth. This is why the Sun caught the imagination of early man leading to a variety of myths (Bhatnagar, and Livingston, 2005). It has always occupied a central position in the evolution of different civilizations. Besides these, it displays a gamut of interesting phenomena, ranging from a few hundred kilometers to several thousands of kilometers in spatial scale, from few milliseconds to several decades in time scale, and from thousands of degrees to several million degrees in temperature. Our Sun is a source of enormous photon flux, which is a great advantage for detailed study even with small telescopes and simple equipments.

The Sun has been widely regarded as the ‘Rosetta Stone’ of astronomy. This is a very appropriate description since our star has provided a ready-made laboratory for studying a variety of processes and phenomena operating both within and outside this object. Solar studies have also served as a valuable guide for the development of the theory of structure and evolution of stars in general and pulsating stars in particular. The proximity of our Sun has enabled a close enough scrutiny of its atmospheric layers and provided data of high spatial resolution of its surface features which is currently not possible

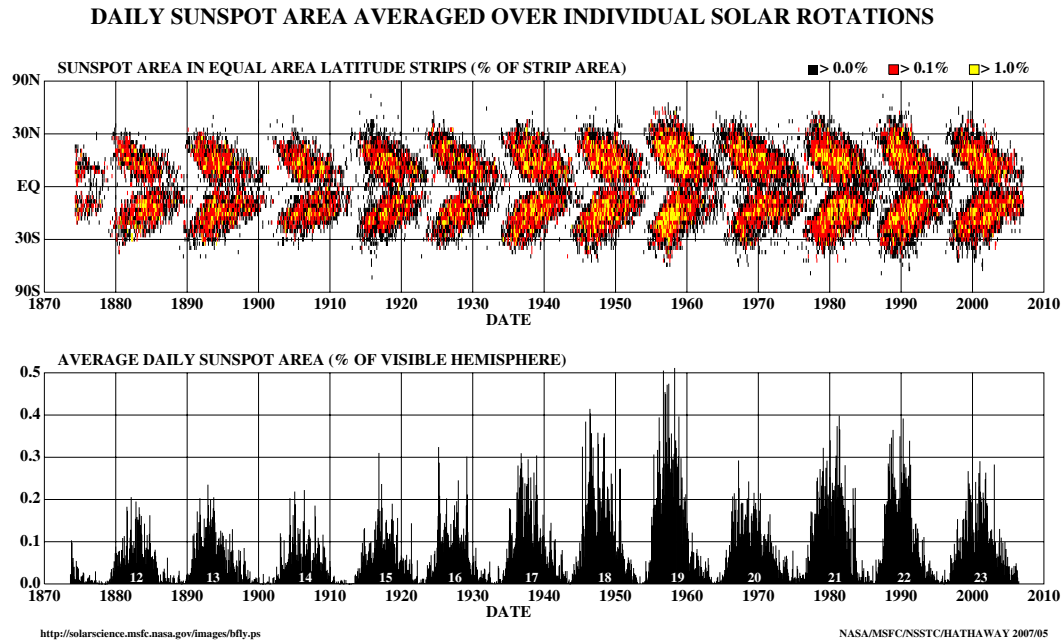


Figure 1.1: Top panel: Butterfly diagram showing the positions of the sunspots for each rotation of the Sun since May 1874. It shows that these bands first form at mid-latitudes, widen and then move toward the equator as each cycle progresses. Bottom panel: The 11-year sunspot cycle for the same period as above.

for other stars in the cosmos.

More than a century ago, all that was known about the Sun was from the study of its face and the visible layers. Indeed, the early astronomers had noticed that the solar disk is dotted with dark blotches. These sunspots were, in fact, known to the Chinese and Greek astronomers, but it was Galileo who first made scientific observations of the passage of these dark spots across the solar disk. The appearance of the sunspots first in mid-latitudes ( $\sim 30^\circ$ ) and then their migration towards the equator following a cycle with a period of approximately 11 years, has been systematically observed and encapsulated in the well-known “butter-fly diagram” due to Maunder as shown in Figure 1.1. Astronomers keep track of the spots appearing and disappearing on the visible disk of the Sun, hoping to gain insight into the processes that derive the solar cycle as well as to link solar activity with terrestrial climatic changes. Observational techniques and instruments used for solar observations evolve with time and reveal the finer details of the activities taking place in the Sun.

## 1.1 The Inhomogeneous Sun

The presence of the localized inhomogeneities in the solar atmosphere leads to the departure from “Quiet Sun” model. Hence, the Sun is no more a static quiescent ball of self gravitating plasma, but a very complex dynamical system. There is a well-defined hierarchy of magnetic elements at the solar surface: magnetic flux tubes or fibrils, faculae, pores, plages and sunspots. Sunspots were the first significant markings observed on the face of the Sun, in the vicinity of which were also noticed the bright, irregular patches called faculae. Later observations made in chromospheric spectral lines revealed the presence of bright areas known as plages overlying the regions of enhanced magnetic fields. There are also widely separated concentrations of magnetic elements or fibrils with field strength of 100-200 G, over scales of the general order of 100 km.

The solar atmosphere displays a rich variety of features and complex phenomena which can be witnessed in their awesome splendour during the occurrence of a total solar eclipse. The chromosphere appears fleetingly just before and after totality as a fiery red ring around the disk and lingers for several seconds before disappearing. At totality, the pearly white solar corona comes into view which changes its shape with the activity cycle, forming a jagged ring around the Sun at the peak of the activity cycle and transforming into trailing plumes and streamers by the end of the cycle. Figure 1.2 illustrates white corona taken at High Altitude Observatory (HAO), Boulder, Colorado on 11 July 1991, during the descending phase of solar activity cycle 22. The corona is an extremely hot, tenuous and inhomogeneous region of the solar atmosphere consisting of complex loop structures with radiation emitted mainly in the UV and X-ray wavelengths. Figure 1.3 shows the evolution of X-ray corona as the solar cycle progresses.

Contrary to thermodynamic expectations, the outer atmosphere of the Sun is hotter than the visible photospheric layers from which much of the solar radiation is emitted. The temperature at the surface of the Sun where the

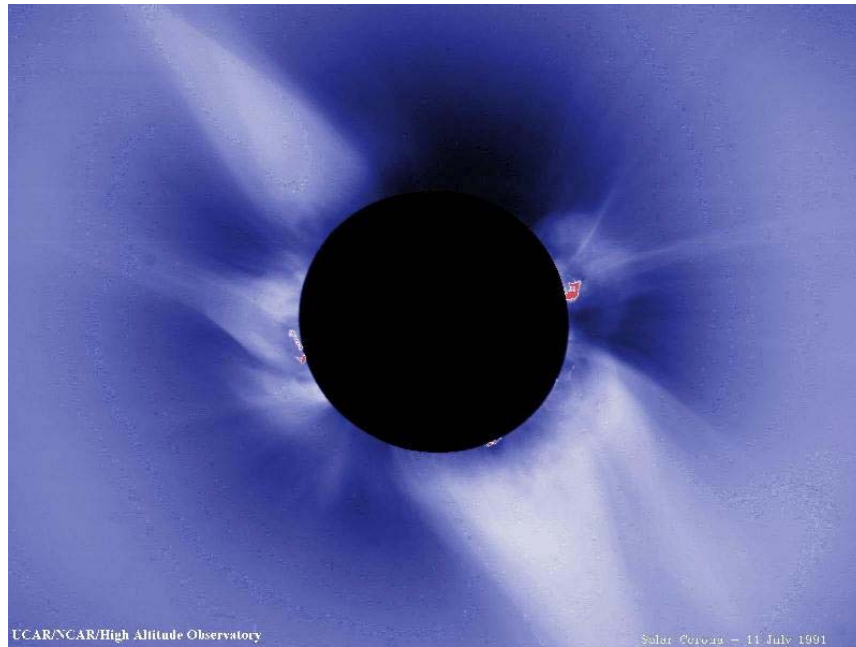


Figure 1.2: The image of white solar corona taken at High Altitude Observatory (HAO), Boulder, Colorado on 11 July 1991, during the descending phase of solar cycle 22.

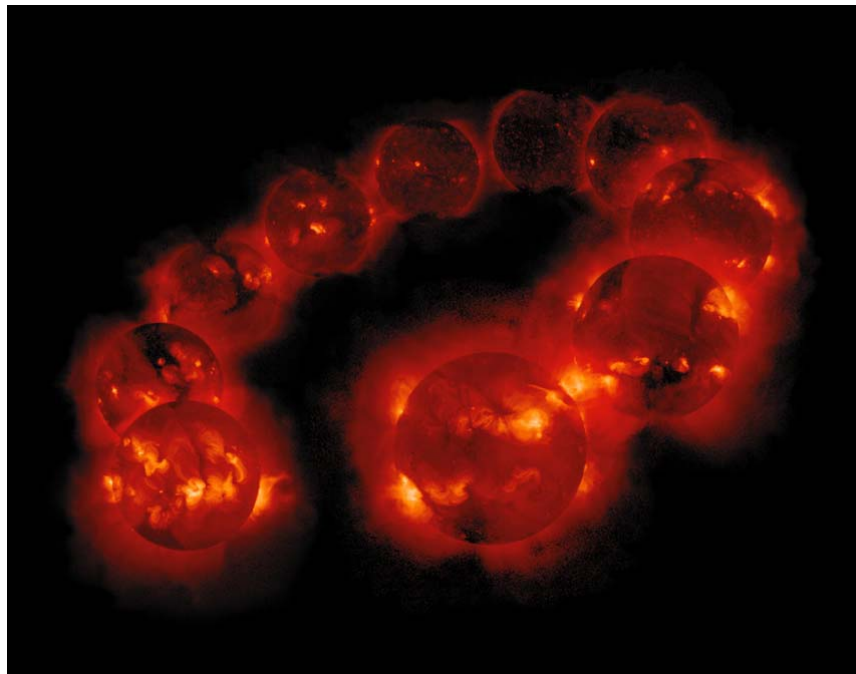


Figure 1.3: A series of soft X-ray images of the Sun for the period between 8 January 1992 and 25 July 1999 showing the corona in X-ray as the solar cycle progresses. These are obtained with the Solar X-ray Telescope on YOHKOH spacecraft.

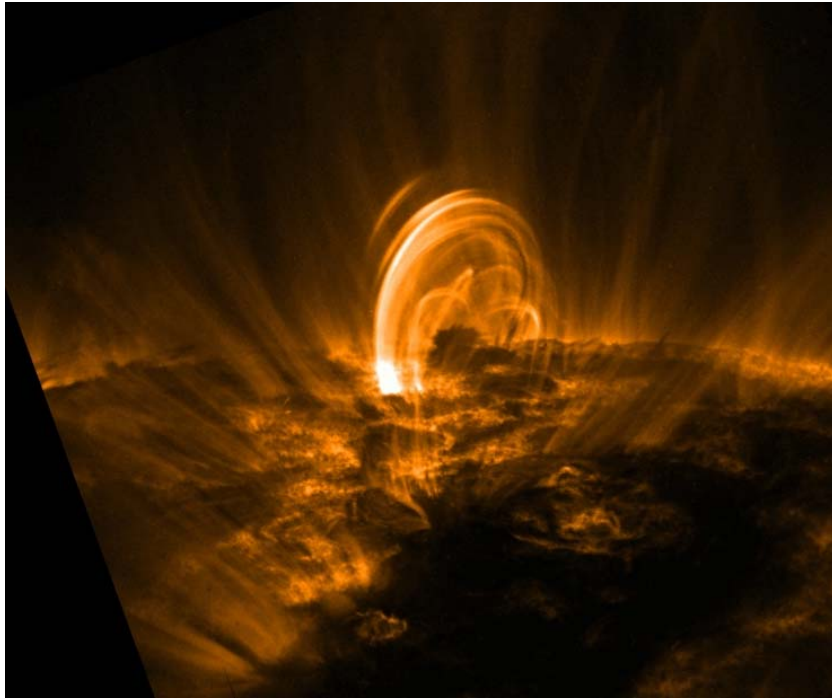


Figure 1.4: Extremely fine structure coronal arcade of loops observed by TRACE of a flaring solar active region.

particle density is about  $10^{17} \text{ cm}^{-3}$  is approximately 5700 K, which decreases to a value of 4200 K at about 500 km above the photosphere and then rises up to a value of several tens of thousand degrees in the chromospheric layers made up of the network and active regions, at heights of around a few thousand km above the visible surface. The overlying coronal regions have temperatures approaching  $(1-2) \times 10^6 \text{ K}$  and are composed mainly of protons and electrons with number densities typically of order  $10^8 \text{ cm}^{-3}$  with an admixture of small amounts of heavier ions. Both the chromosphere and corona are observed to be highly structured and show clear evidence of association with the solar magnetic fields. High resolution images from Transition Region and Coronal Explorer (TRACE) spacecraft show that a large part of the corona has fine-structure down to sub-arcsec scale (Figure 1.4).

In the interior, it is the solar material that controls the magnetic field lines, while outside the solar body it is the magnetic field that dictates the behaviour of the plasma causing a variety of dynamic and transient phenomena. In fact, the magnetic field serves as an effective agent and provides a con-

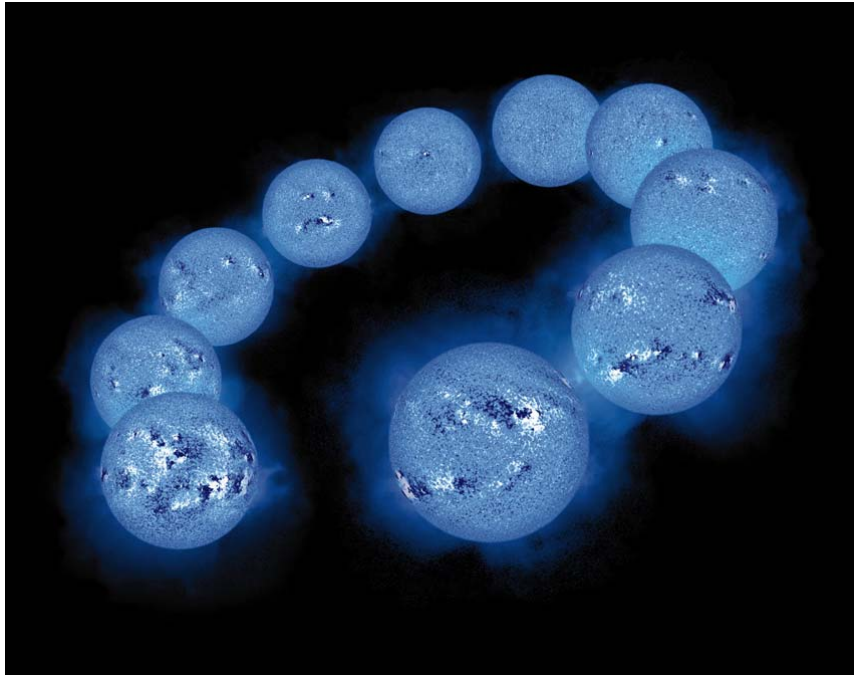


Figure 1.5: A series of photospheric magnetograms recorded at Kitt Peak, NSO, USA, showing the solar activity cycle from 8 January 1992 to 25 July 1999. Black and white patches represent opposite polarities of line-of-sight magnetic field on the Sun.

duit to transport of energy from sub-photospheric motions and waves to the chromospheric/coronal regions and at other times acts as a trigger displaying spectacular events in the form of flares. Prominences of various kinds (e.g., quiescent, loop, hedgerow, eruptive, etc.) are seen to rise above active regions on the solar surface, providing striking evidence for the presence of magnetic fields in the outer atmosphere capturing and controlling the motion of the plasma along the field lines. It is evident that if the Sun were not to possess any magnetism, its external layers would not have presented such a spectacularly dazzling and explosive picture. Figure 1.5 shows the evolution of solar magnetic fields with the solar cycle.

## 1.2 Observations of the evolution of inhomogeneities in the Sun

The evolution of aforesaid activities of the Sun over the solar cycle provides us opportunity to understand the basic astrophysical processes taking place in

the Sun from large to very small spatial scales. The Sun can be observed from both, ground and space based telescopes. Space based observations are free from atmospheric effects; they are however expensive and short lived. Ground based facilities can stably operate for longer time and are convenient for future upgradations, apart from being of less expensive relative to space based observational facilities. However, it is very necessary to develop proper observing techniques like adaptive optics to support the ground based observations in order to compensate the atmospheric effects. Thus, with the help of such observing facilities we can continuously monitor the dynamic activities of the Sun over several solar cycles with progressively improved observational techniques. This would refine our understanding of the physics involved in the various interesting solar phenomena and also help in precise Space Weather predictions.

### **1.3 Earth's atmospheric turbulence and astronomical seeing**

The Earth's atmosphere is a highly turbulent medium. Heating of the Earth's surface by the solar radiation causes turbulent air motions in the atmosphere. According to the Kolmogorov's theory of fluid turbulence (Kolmogorov, 1941), when the kinetic energy of the air motions at a given length-scale is much larger than the energy dissipated as heat by viscosity of the air at the same scale- a condition indicative of fully developed turbulence -the kinetic energy of large scale motions would be transferred into smaller and smaller scale motions; motions at small scales would be statistically isotropic; at the smallest scales, viscous dissipation would dominate the break-up process.

During day time, large warm packets of air closer to the ground move up due to buoyancy and initiate convection, causing turbulence near the ground (typically, up to one km height from the surface, depending on local orography and strength of the wind). They dissipate their kinetic energy continuously and randomly into smaller and smaller packets of air, each having a unique



temperature. These packets are often called *turbulent eddies*. Convection changes with insolation and disappears during night time. However, horizontal circulation of air starts. An important property of the turbulent eddies is that they exist in a variety of length-scales and their distribution is random. There exists an upper limit,  $L_0$ , decided by the process that generates the turbulence and a lower limit,  $l_0$ , decided by the size at which viscous dissipation overtakes the break-up process. Within these limits (often called the ‘inertial range’), the energy of the eddy is proportional to the  $5/3$  power of its linear size (Kolmogorov, 1941).

Turbulent air motions cause fluctuations in the density, pressure, temperature and humidity of the air from one point to another. While the local temperature fluctuations of the air could be of the order of a few hundredths of a degree throughout the atmosphere, fluctuations of a few tenths of a degree or more are typical in the lowest layer of the atmosphere. As the refractive index of air is highly sensitive to the temperature fluctuations, it varies randomly from one point to another. Fluctuations in the refractive index induce random optical path lengths to the rays that are normal to the wave-front arriving at the atmosphere from a distant star. Consequently, when the wave-front reaches the entrance pupil of a ground based telescope, it becomes already corrupted in the sense that the surface of constant phase is no longer planar; it has an overall tilt and small scale corrugations on top of it. The *rms* value of the phase perturbations increases with the size of the wave-front.

The perturbations in the wave-front produce effects similar to optical aberrations in the telescope and thus degrade the image quality. When a very small aperture is used, a small portion of the wave-front is intercepted and the phase of the wave-front is uniform over the aperture. If the amplitudes of the small scale corrugations of the wave-front are much smaller than the wavelength of light, the instantaneous image of a star is sharp and resembles the classical diffraction pattern. But as the wind moves the eddies past the aperture, the tilt of the intercepted wave-front changes. This change in the tilt causes random motion of the star’s image at the focal plane. As the aperture

size increases, there is a decrease in the sharpness and the amplitude of the motion. When a large aperture is used, the amplitude of the random variation of phase across the interpreted wave-front is larger. This leads to the blurring of the image. The image motion and blurring together are referred to as *atmospheric seeing* or simply *seeing* (Young, 1971; Labeyrie, 1976).

## 1.4 Adaptive optics for solar observations

In 1953, H.W. Babcock, a solar astronomer, introduced the concept of Adaptive optics (AO), viz., improving the resolution of ground based imaging systems by correcting the perturbed wave-front at the pupil plane. He also introduced the concept of deformable mirrors for correcting the wave-fronts. However, the progress in this field was rather slow due to the lack of the technological development and the multi-disciplinary expertise needed for the physical realization of an AO system. In the last 25 years, intricate nature of such a system has been understood both theoretically and experimentally to such an extent that today it has become an integral part of any large ground based telescope operating at optical and infra-red wavelengths. The advances in this direction have been broadly reviewed by Beckers (1993), Roggema, Welsh, and Fugote (1997). Also, a number of papers on the advances and application of AO system are available in Rimmele, Balasubramaniam, and Radick (1999). A low-cost AO system developed by National Solar Observatory, USA, is operational at McMath-Pierce Telescope on Kitt Peak and has been proved to be very useful for their solar observing programs (Keller, Plymate, and Ammons, 2003). Similarly, a low-order AO system operational at the Swedish 1-meter Solar Telescope at the Roque de los Muchachos on the Canary island of La Palma has yielded significant results (Scharmer *et al.*, 2003).

## 1.5 Motivation of the thesis

The prime idea of this research work is to identify and understand the morphology, dynamics and influence of the localized inhomogeneities in the solar atmosphere at different length-scales and scale heights. The large-scale inhomogeneities appear in the form of magnetic features, like, sunspots, filaments, supergranulations, faculae and plages etc., whereas the small-scale magnetic features include the pores, fibrils, spicules, granulations, network and intranetwork regions. These inhomogeneities evolve with the solar cycle and give rise to interesting events (Bhatnagar, 2006). Some of these events are very rare, such as detection of photospheric “Doppler ribbons” (c.f., Chapter V of this thesis) and “solar quakes” (Kosovichev and Zharkova, 1998) during intense solar flares. Figure 1.6 depicts seismic waves spreading out from a flaring region towards the photosphere as ripples on a water pond during a 1B/X2.6 class solar flare on 9 July 1996, observed by SOHO/MDI instrument. The study of such rare events (Kumar *et al.*, 2006) can enhance our knowledge about the basic astrophysical processes taking place in the Sun on different length-scales.

The aforesaid investigations could be done by resolving the fine structures of these inhomogeneities in multi-wavelengths at different heights of the solar atmosphere from photosphere to corona through the chromosphere and transition region. These observations could be accomplished by both, space based and ground based Observatories. Space based observations are free from atmospheric effects; they are however short lived and expensive. On the other hand, ground based observations are stable, however affected by Earth’s atmospheric turbulence. The atmospheric turbulence or “seeing” could be well estimated using established techniques. In this thesis, solar  $H\alpha$  images have been extensively used to quantify “seeing” at the lake site of Udaipur Solar Observatory (USO). Also, the efficacy of using small imaging telescopes even for initial site surveys for large ground based observational facilities has been established (Kumar, Venkatakrishnan, Raja Bayanna, and Venugopalan, 2007). The estimates of “seeing” obtained in this analysis helped in determining the

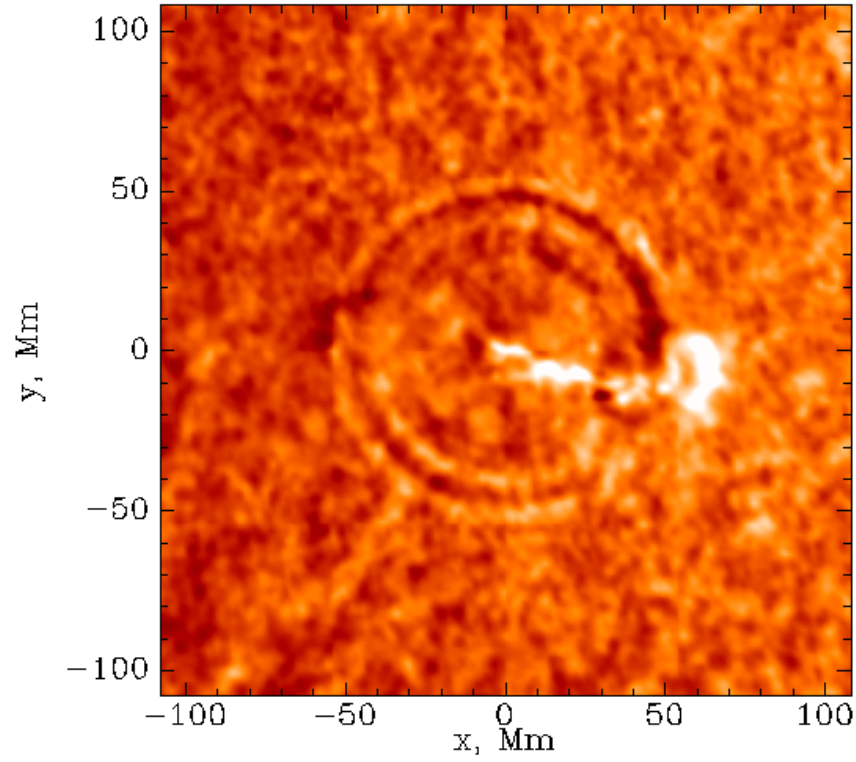


Figure 1.6: Velocity image obtained by SOHO/MDI showing the expanding solar quake associated with a large X-class flare on 9 July 1996 (Kosovichev and Zharkova, 1998).

aperture of a Multi-Application Solar Telescope (MAST) proposed for USO (Venkatakrishnan *et al.*, 2004). It also helped in the design and development of an Image Stabilization (ISS) system at USO (Sridharan *et al.*, 2005; Kumar *et al.*, 2005; Raja Bayanna *et al.*, 2006, 2007), which will be basically used for improving the resolution of ground based imaging systems by correcting the perturbed wave-front passing through the Earth's turbulent atmosphere.

# Chapter 2

## Estimation of atmospheric “seeing” using solar $H\alpha$ images

### 2.1 Introduction

The performance of ground based telescopes is limited by the perturbations introduced by the atmospheric turbulence. Generally, atmospheric turbulence is characterized by a spatial scale ‘ $r_0$ ’ known as Fried’s parameter (Fried, 1965, 1966, and 1967). It is interpreted as the size over which the *rms* variance of the phase fluctuations is one  $\text{rad}^2$ , that corresponds to a Strehl ratio of 0.33 (Rodier, 1981). Strehl ratio is defined as the ratio of the observed peak intensity at the detection plane of a telescope or other imaging system from a point source compared to the theoretical maximum peak intensity of a perfect imaging system working at the diffraction limit. In a long exposure image, the transfer function of an image is the product of telescope transfer function and atmospheric transfer function. Atmospheric transfer function is represented as  $\exp(-3.44(\lambda f/r_0)^{5/3})$ , where  $f$  is the spatial frequency. By knowing the value of  $r_0$ , we can theoretically obtain the transfer function of the atmosphere. Deconvolution of the long exposure image using this theoretical transfer function can improve the images to the extent permitted by the noise. Speckle interferometry is another important image restoration technique used in ground based imaging systems for high resolution observations. It uses theoretical models for

estimation of the speckle transfer functions. These models need the knowledge of seeing parameter of the particular site. Further, the knowledge of Fried's parameter for a given site helps not only in reconstruction of high resolution images, it also helps in designing and building an Adaptive optics (AO) system. The various ways for estimation of  $r_0$  from a series of short exposure ( $\sim 1-10$  ms) images are: measurement of angle of arrival fluctuations, power spectrum equalization method, estimation of differential image motion, and spectral ratio technique etc. The advantages and disadvantages of the aforesaid methods have been widely discussed by Sridharan, Venkatakrishnan, and Verma (2002). Goode *et al.* (2000) has presented a comparison between the spectral ratio technique (von der L  he, 1984) and solar scintillometry (Seykora, 1993; Beckers *et al.* 1997; Beckers, 2001). Bell, Hill, and Harvey (1999) used the modulation transfer functions (MTFs) of low-resolution continuum solar images taken for the Global Oscillation Network Group (GONG) to obtain  $r_0$ .

In this work, we employ the spectral ratio technique to estimate  $r_0$ . Spectral ratio method, originally proposed by von der L  he (1984), is one of the proven methods to estimate the Fried's parameter. For using this method, we need a time series of images of arbitrarily shaped structure, and the structure should have features smaller than seeing limit. Also, the images should be of short exposure with large number of frames recorded in a short duration ( $\sim 1$  min for solar observations (von der L  he, 1993)) to achieve statistically significant results. Further, it is recommended that the field-of-view should be restricted to the size of isoplanatic patch. Sridharan, Venkatakrishnan, and Verma (2002) have used solar  $H\alpha$  images from different Indian Observatories to estimate  $r_0$  using various methods including the spectral ratio method. The images from Udaipur Solar Observatory (USO) used in the aforesaid study were taken with exposure times  $\sim 20$  ms with the CCD camera dedicated to the synoptic observations of the Sun. However, we have been able to acquire short exposure (3 ms) high resolution  $H\alpha$  images (spatial scale of  $\sim 0.55$  arc-sec per pixel) in burst mode, using a new CCD camera at the image plane of the 15 cm refractor spar telescope located at the lake site of USO. These images have been used for

estimation of  $r_0$  employing the spectral ratio technique. In order to understand the diurnal and seasonal evolution of  $r_0$ , this study has been carried out daily once an hour over the months of January–June of the years 2005 and 2006. The lake site observatory of USO is located on a small island in the middle of the Lake Fatehsagar ( $24^\circ.5$  N,  $74^\circ$  E) at Udaipur in India. USO also hosts one of the six GONG telescopes which is located on a hillock inside the main office campus of USO, a little away from the lake.

USO is in the process of installing a Multi-Application Solar Telescope (MAST) equipped with an AO system at the aforesaid lake site. The estimates of  $r_0$  obtained in our analysis helped in determining the optimum size of the MAST. It also helped in the design and development of a proto-type Adaptive optics system at USO (Sridharan *et al.*, 2005).

## 2.2 The observational data

The typical time scale of the evolution of the atmosphere is  $\sim (1-10)$  ms, and hence images taken with such exposure times will contain solar features viewed through “frozen” atmosphere. In our case, the time exposure of 3 ms has been chosen according to the capability of our CCD camera in acquiring the images with optimum dynamic range. The CCD camera being used in our observations has a front-illuminated image sensor (ICX285AL chip) with pixel size  $6.45 \times 6.45 \mu\text{m}$  and scan rate of 20 MHz. This camera is able to acquire 12 frames/sec with 12-bit resolution and exposures in the range  $5 \mu\text{s} - 65$  s. The lake site Observatory of USO has a 12 foot long spar telescope ( $D = 15$  cm ;  $f = 225$  cm), generously gifted by CSIRO, Australia. At present, it is housed inside a dome, at a height of about 10 m above the ground. Our spar telescope is dedicated to the synoptic observations of the Sun in  $\text{H}\alpha$  line-center ( $\lambda = 6563 \text{ \AA}$  ; pass-band =  $0.5 \text{ \AA}$ ) during 04:30–11:30 UT. Generally, short exposure high resolution solar images taken in G-band are used for quantifying seeing of a given site (Rutten *et al.*, 2004). The G-band images provide good contrast in the observed granular pattern (Rao *et al.*, 2001) and hence those

are regarded as reasonable source for estimation of  $r_0$  of a site. However, these images have very poor contrast in quiet solar regions at sites of moderate to poor seeing while observing with small aperture telescopes. We need images of better contrast for such sites. G-band images do show the supergranular network even in poor seeing, but not the finer granulation structure. It is only  $H\alpha$  images which show reasonable contrast with a 15 cm telescope over a wide band of spatial frequencies. Figure 2.1 is the mean Wiener spectrum obtained from 100 short exposure  $H\alpha$  images, which demonstrates this wide bandwidth. We, therefore, decided to use  $H\alpha$  images for  $r_0$  measurements. In order to verify that the estimation of  $r_0$  is independent of the object's properties, we have compared the results in  $H\alpha$  line-center with those in red and blue wings (c.f., Figures 2.2 (a), (b), and (c)). It is found that the value of  $r_0$  is almost the same in all the three cases. This encouraged us to use the images taken in  $H\alpha$  line-center for quantifying the seeing of our lake site. For every run of observations intended for estimation of  $r_0$ , we have taken 100 short exposure (3 ms) images accompanied by the dark and flat images in order to perform a good correction to the images. The observations have been carried out everyday on hourly basis during 04:00–10:30 UT over the months of January–June of the years 2005 and 2006. It is noteworthy to mention that the lake was almost dry during the observing period in 2005. The solar observations got interrupted after the onset of monsoon in the last week of June, 2005, while the monsoon rains extended abnormally till October, 2005. The lake continued to fill and even overflowed after the rains, hampering the observations till we recovered in the last week of December, 2006. Our regular observations and estimation of  $r_0$  started again in January, 2006, and continued till the onset of monsoon in the last week of June, 2006 at Udaipur.

## 2.3 Analysis and Results

As has been mentioned in the previous Section, we have acquired 100 short exposure high resolution solar images in burst mode in  $H\alpha$  line-center for each



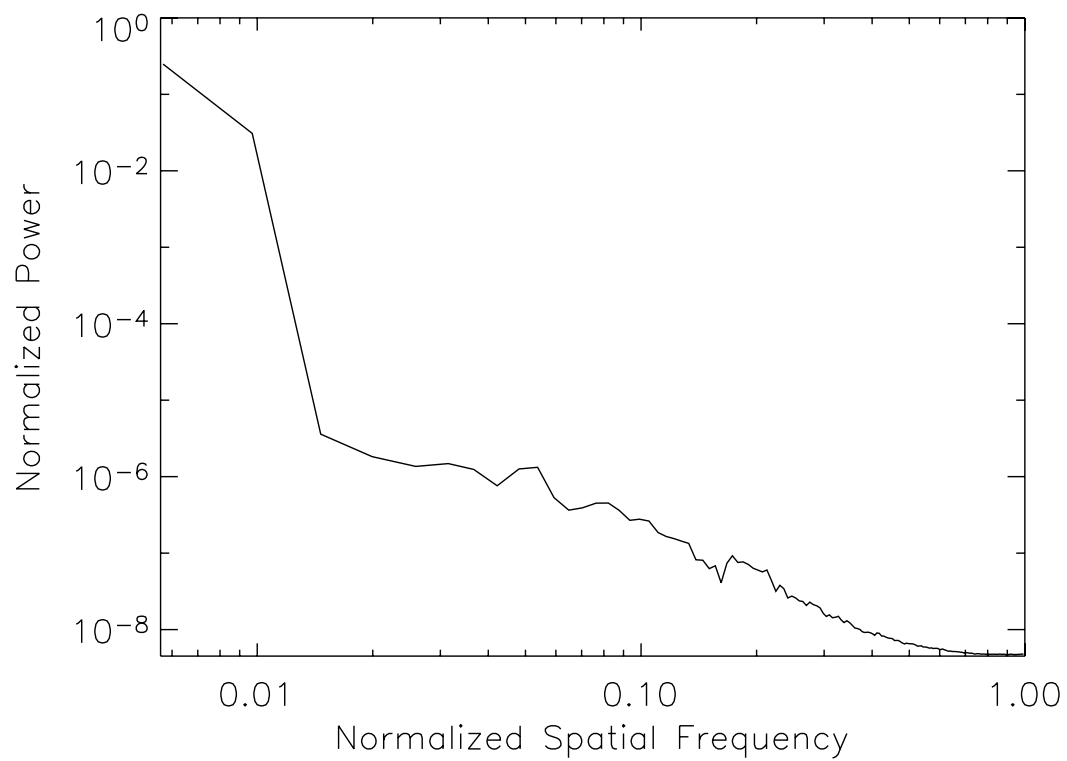


Figure 2.1: The mean Wiener spectrum obtained from 100 short exposure (3 ms)  $H\alpha$  (6563 Å) images. The power spectrum illustrates that these images have reasonable contrast over a wide band of spatial frequencies.

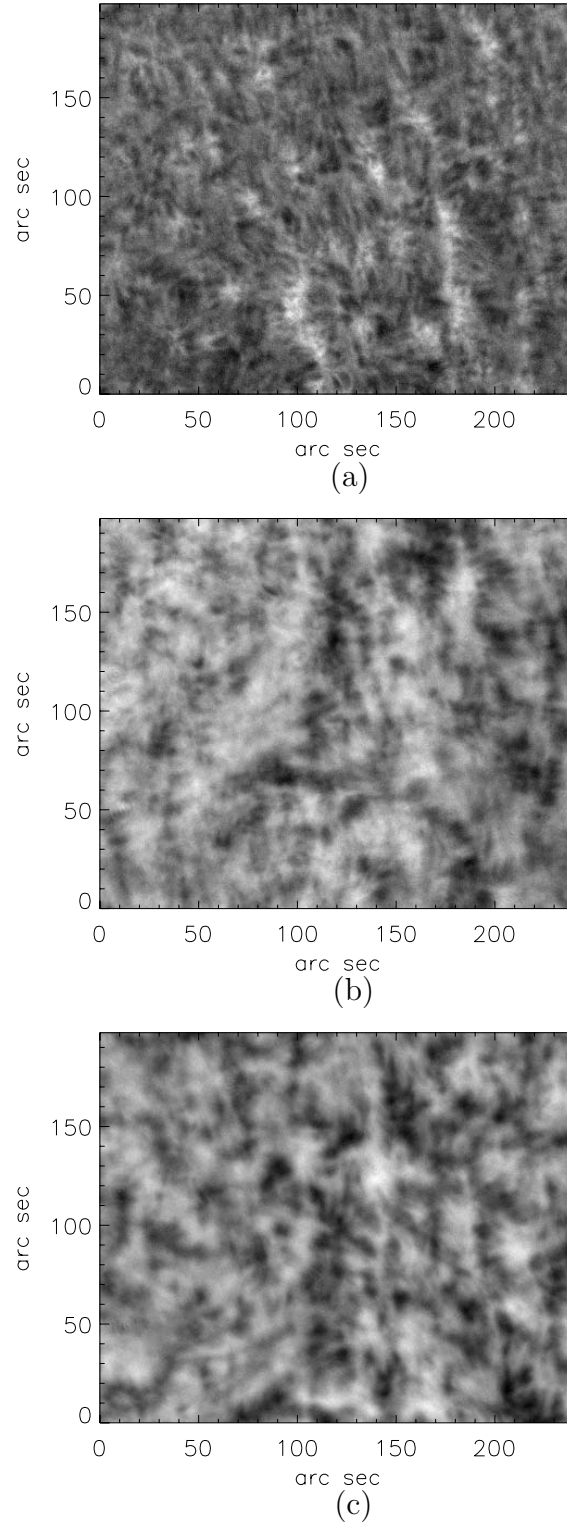


Figure 2.2: Typical short exposure images of the Sun taken in: (a) line-center ( $6563 \text{ \AA}$ ), (b) blue wing ( $6563-0.5 \text{ \AA}$ ), and (c) red wing ( $6563+0.5 \text{ \AA}$ ) of  $H\alpha$  taken from the 15 cm refractor spar telescope at the lake site of USO. The values of  $r_0$  estimated from these images are: (a)  $5.196 \pm 0.37 \text{ cm}$ , (b)  $5.256 \pm 0.40 \text{ cm}$ , and (c)  $5.216 \pm 0.32 \text{ cm}$ .

observing run of about 5 minute duration intended for estimation of  $r_0$ . These observing runs have been taken once an hour daily. Each of the 100 images mentioned above is first flat fielded and dark corrected and then co-aligned with respect to the first image of the sequence. This registration was necessary to remove telescope drift and vibrations. However, since the image FOV ( $\sim 382 \times 281$  arc-sec) is much larger than the isoplanatic patch, the registration will not destroy the tilt component of the seeing. Figure 2.2 (a) shows the raster of one such image illustrating the fine structures present in the solar atmosphere. These co-aligned images are sub-divided into rasters of the size  $32 \times 32$  pixels (total FOV  $\sim 18 \times 18$  arc-sec). Thus, we have 280 rasters of  $32 \times 32$  pixels from each image of the size  $640 \times 448$  pixels after rejecting the wrapped portions of the registered images ( $696 \times 512$  pixels). In our analysis, we estimate  $r_0$  for each raster from the time sequence of 100 images and then produce an average value of  $r_0$  from the 280 values. The *rms* variation of the 280  $r_0$  values also provides an upper limit for the measurement error.

The summary of the spectral ratio technique is as follows. A mean image is constructed from the individual short exposure images, for which the atmosphere is assumed to be “frozen”. The mean image thus obtained is subjected to Fast Fourier Transform (FFT). Further, we perform FFT of the individual 100 images. Now, the ratio of the squared modulus of the FFT of mean image and the mean of the squared modulus of FFT of the individual images can be represented by  $S$  as follows:

$$S = \frac{|\langle FT[Image] \rangle|^2}{\langle |FT[Image]|^2 \rangle} \quad (2.3.1)$$

$S$  depends on the seeing conditions that prevailed during the period of observation. This ratio  $S$  allows us to extract the normalized atmospheric cut-off frequency  $f_c$  (c.f., Equations (3) and (4), von der L  he, 1984) from the burst of high resolution images. The Fried’s parameter  $r_0$  is given by  $f_c D$ , where  $D$  is the aperture of the telescope and the parameter  $f_c$  is illustrated in Figure 2.3.

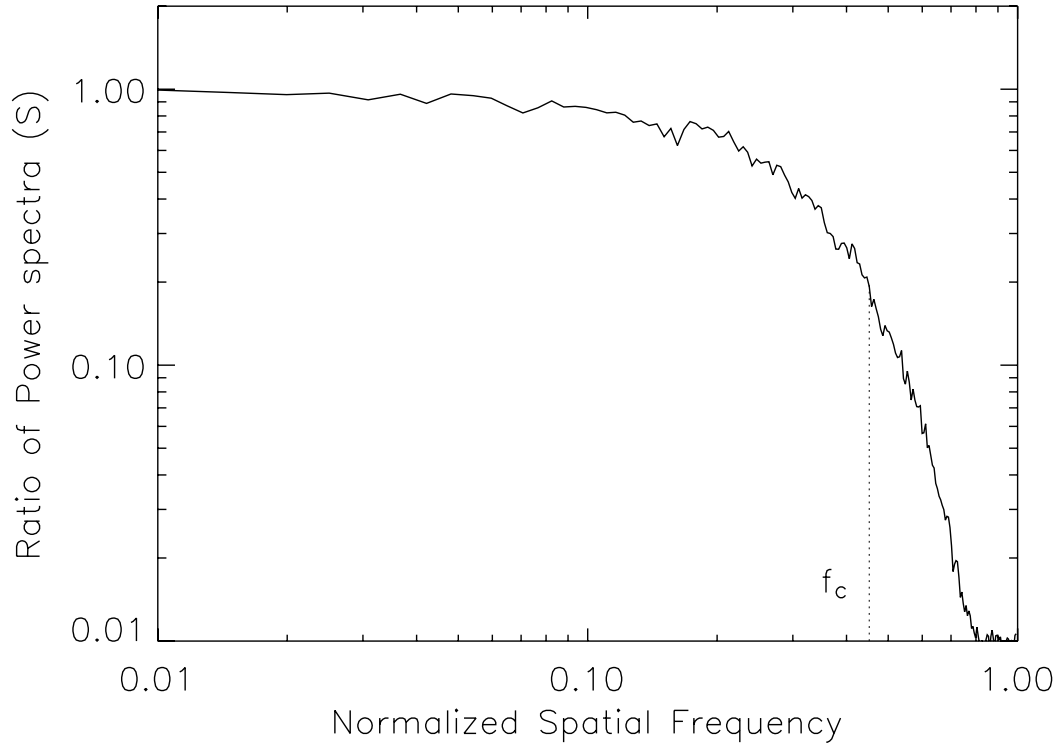
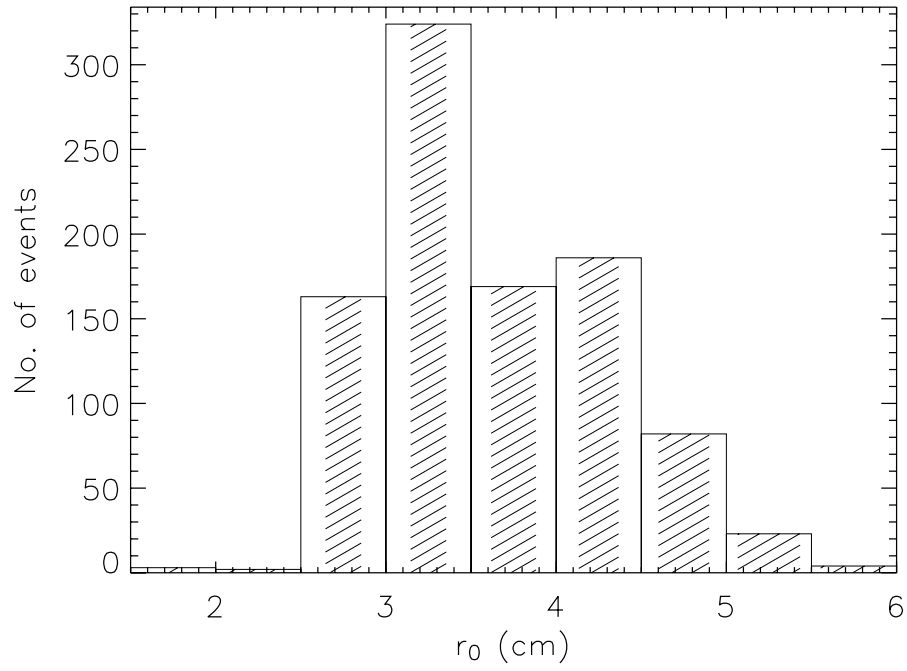


Figure 2.3: Plot of  $S$  (c.f., Equation (1)) v/s normalized spatial frequency. The normalized atmospheric cut-off frequency ( $f_c$ ) is indicated in the plot.

Figure 2.4 shows the histogram distribution of  $r_0$  obtained during the period January–June for the years 2005 and 2006. The lake was almost dry during the observing period in 2005 while it overflowed during our observations in the year 2006. For the condition of the lake without water, the value of  $r_0$  ranges between 1.5 cm and 6.0 cm with the mean of the distribution in the bin 3.0–3.5 cm at different epochs of the USO observing time over the months January–June, 2005. However, for the condition of the lake overflowing with water, there is obvious improvement in the seeing and the value of  $r_0$  ranges between 2.0 cm and 8.0 cm with the mean of the distribution in the bin 4.0–4.5 cm. In Figure 2.5, we show the mean value of  $r_0$  for each observing day during the aforesaid periods. The mean values of the  $r_0$  also show an improvement by 1.0 cm for the lake with water. The plots shown in Figures 2.4 and 2.5 provide a good comparison of the seeing at the site as regards to the condition of the lake with water and without water.

$r_0$  between 04:30–10:30 UT during Jan–June 2005



$r_0$  between 04:30–10:30 UT during Jan–June 2006

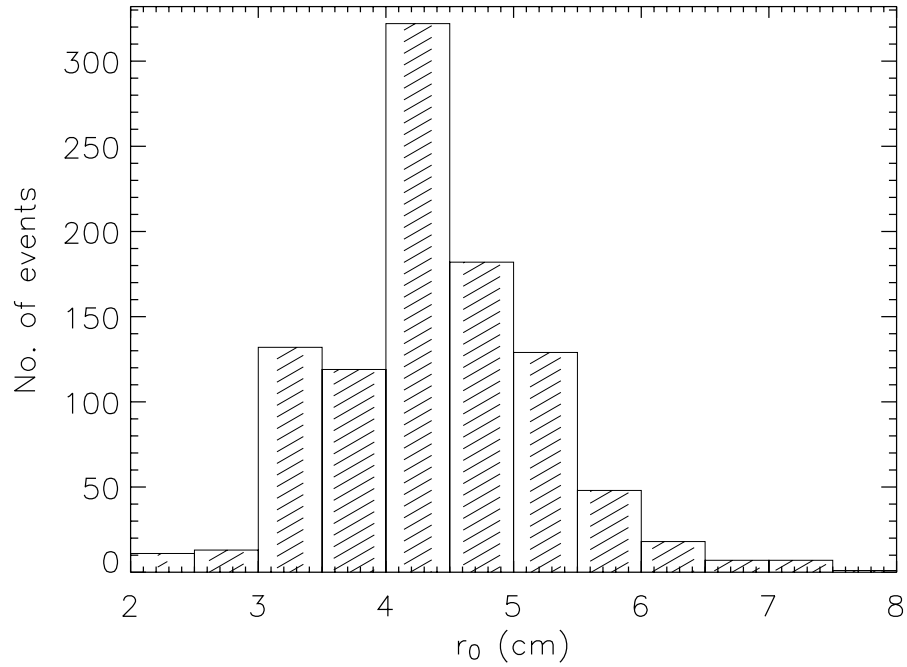


Figure 2.4: The *top panel* shows the histogram distribution of  $r_0$  for the period January–June, 2005 while the *bottom panel* shows that for the year 2006. The range of  $r_0$  varies between 1.5 cm and 6.0 cm when the lake was dry, while it is between 2.0 cm and 8.0 cm for the filled lake condition. The shaded area in the histograms show  $2\sigma$  values.

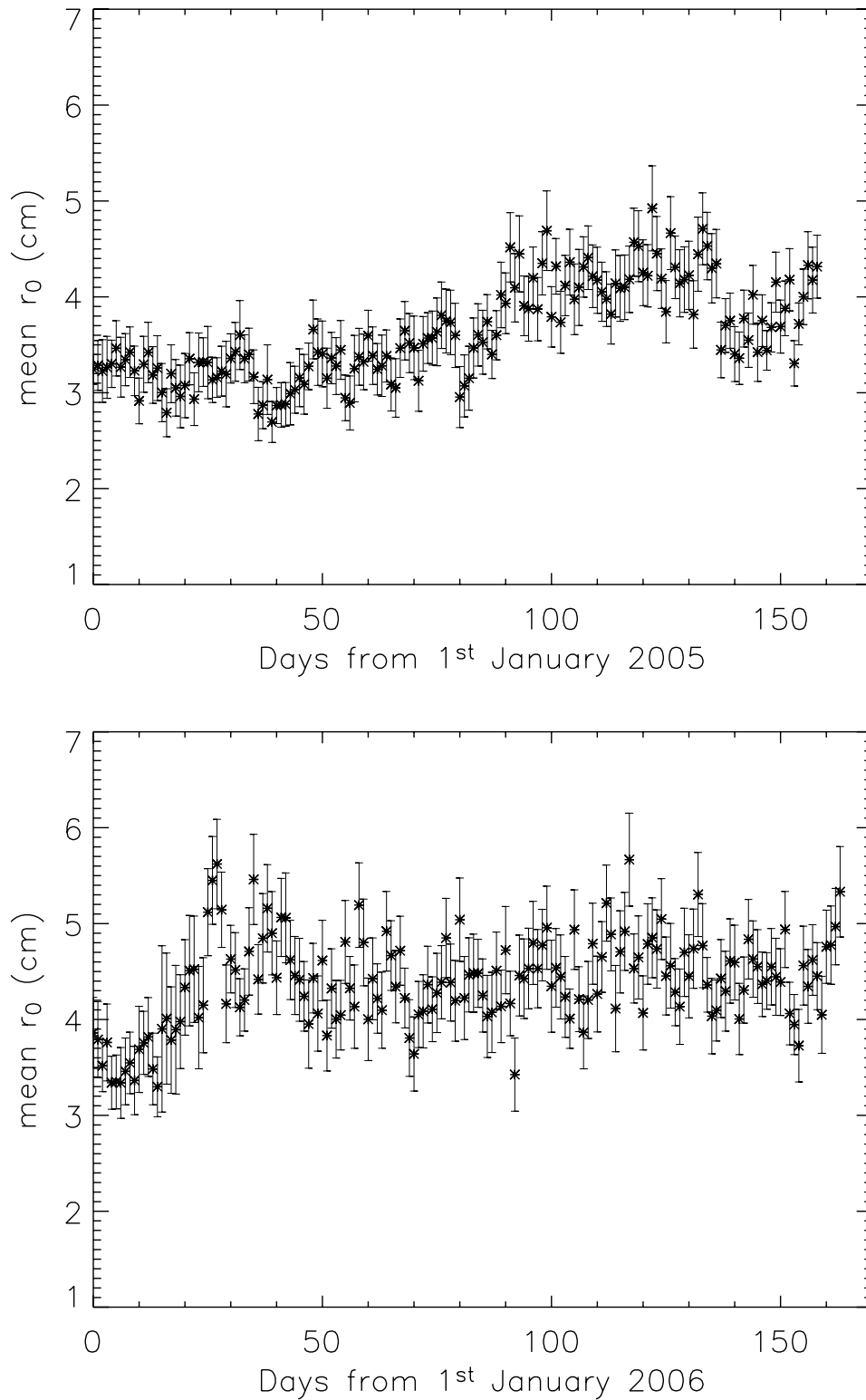


Figure 2.5: The *top panel* shows the mean value of  $r_0$  for each day during the period January–June, 2005 while the *bottom panel* shows that for the year 2006. A change in mean  $r_0$  by about 1.0 cm is observed for the lake with water as compared to the dry condition. The error bars indicate  $\pm 1\sigma$  values.

## 2.4 Summary and Discussions

Using spectral ratio technique, we have estimated  $r_0$  extensively using short exposure (3 ms) high resolution (spatial scale of  $\sim 0.55$  arc-sec per pixel)  $H\alpha$  (6563 Å) images taken in burst mode from a 15 cm refractor spar telescope located at the lake site of USO. This study has been carried out daily once an hour over the months January–June of the years 2005 and 2006 to understand the diurnal and seasonal evolution of  $r_0$ .

It is essential to quantify the seeing conditions prevailing at a site for deciding the aperture of a telescope which helps in achieving optimum performance with an AO system. USO has been involved in synoptic observations of the Sun in  $H\alpha$  line for many years apart from building new instruments viz., digital imaging multi-slit spectrograph (Srivastava and Mathew, 1999), solar video magnetograph (Mathew *et al.*, 1998), and solar vector magnetograph (Gosain, Venkatakrishnan, and Venugopalan, 2006) etc. at different epochs. However, recently a Multi-Application Solar Telescope (MAST) has been proposed to be installed at the lake site of USO (Venkatakrishnan *et al.*, 2004; <http://www.prl.res.in/~uso/mast.html>). Hence, in order to decide the size of MAST equipped with an AO system, we started these observations in January 2005. The observations continued till the arrival of monsoon rains in the month of June 2005. The lake was in dry state during the aforesaid period due to drought like conditions prevailing since 2002. Fortunately, there were very good rains after this period and the lake overflowed after the monsoon. It provided us a unique opportunity to compare our results obtained in dry condition with that of the lake filled with water. Therefore, we have taken similar set of observations during January–June, 2006. This work reports the first systematic study of seeing using  $H\alpha$  images employing the spectral ratio technique.

The lake with water shows improvement in  $r_0$  by about 1.0 cm with respect to previous dry condition and mean varies between 4.0–4.5 cm as evident from the data obtained between January–June, 2006. The systematic comparison of

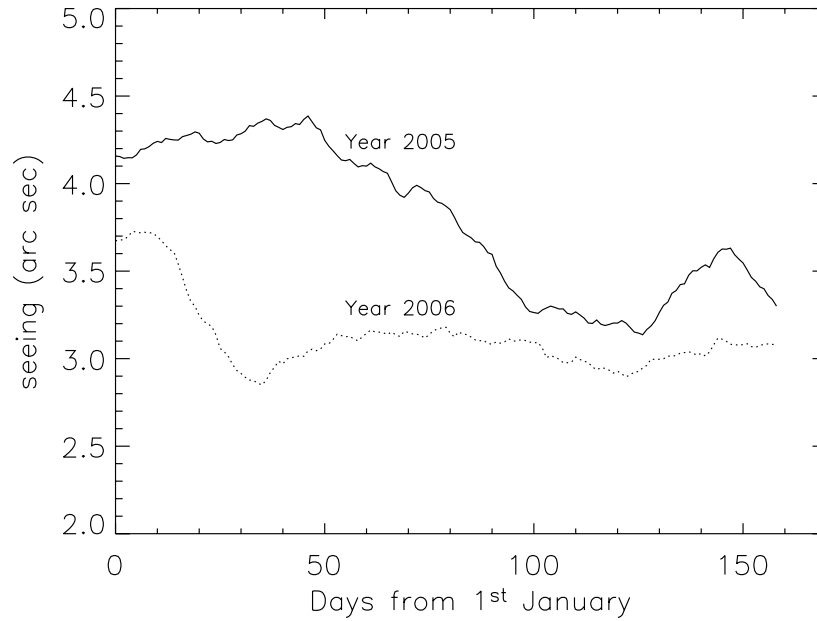


Figure 2.6: The plots show smoothed version of the mean seeing ( $\theta \approx \lambda / \text{mean}(r_0)$ ) for each day during the months of January–June for the years 2005 (*solid curve*) and 2006 (*dashed curve*).

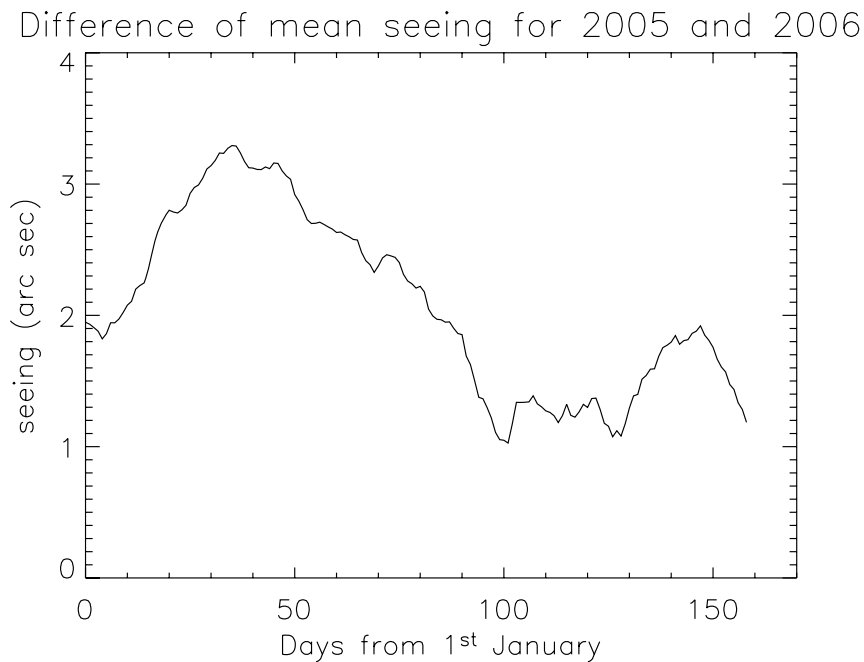


Figure 2.7: The plot shows the quantity  $\sqrt{\theta_{dry}^2 - \theta_{filled}^2}$  for each day during the months of January–June of the years 2005 and 2006.  $\theta_{dry}$  is the seeing for the condition of the lake without water while  $\theta_{filled}$  is that for the lake with water as have been illustrated in Figure 2.6.



seeing at different kinds of sites (Beckers and Mason, 1998) has been very useful in establishing the utility of water bodies for extending good and consistent seeing conditions over the day. In this paper, with our long term investigations of seeing and the episodic conditions of the lake, we have established that the seeing at a site surrounded by a water body is indeed better than that at the same site without the water body. By measuring  $r_0$  over a long period of time, we can also study the seasonal variations in the upper atmospheric conditions.

We now plot a smoothed version of the mean seeing for each day ( $\theta \approx \lambda/\text{mean}(r_0)$ ) for both the years in Figure 2.6. Figure 2.7 shows  $\sqrt{\theta_{dry}^2 - \theta_{filled}^2}$  as a function of time. Inspection of Figure 2.6 reveals some interesting details. The seeing in early January is seen to be poor in both the years. The sky conditions were poor in early January during both the years. Thus, the deterioration of the upper atmospheric weather seems to wield a greater influence on the seeing than the presence of a water body. A similar deterioration in seeing produced by dust storms can also be seen during the days from 130 to 150 of the year 2005. Figures 2.6 and 2.7 can be understood in terms of a 3-component model for the seeing. Let us assume that the seeing consists of contributions from: (a) upper atmospheric (extended or disturbed boundary layer typical of day-time conditions), (b) ground heating, and (c) dome seeing. The upper atmospheric contribution is largest during unstable meteorological conditions. For a sub-tropical island site like Udaipur, visibly bad sky conditions prevail in monsoon and continue up to the end of December but improve beyond January till onset of monsoon in June. The present USO dome encloses a large volume of air with a very narrow slit. Hence, the air inside is much warmer than the outside air in winter. The air outside becomes quite hot in summer and matches the temperature of air inside the enclosure in summer. Thus dome seeing is important in winter and less important in summer. We should therefore expect the seeing to monotonically improve from winter to summer. The  $\theta_{dry}$  shows such an improvement commencing from day 40, ignoring the deterioration in seeing between the days from 130 to 150 caused by dust storms. On the other hand, the  $\theta_{filled}$  shows an earlier onset of good seeing, but no further improvement

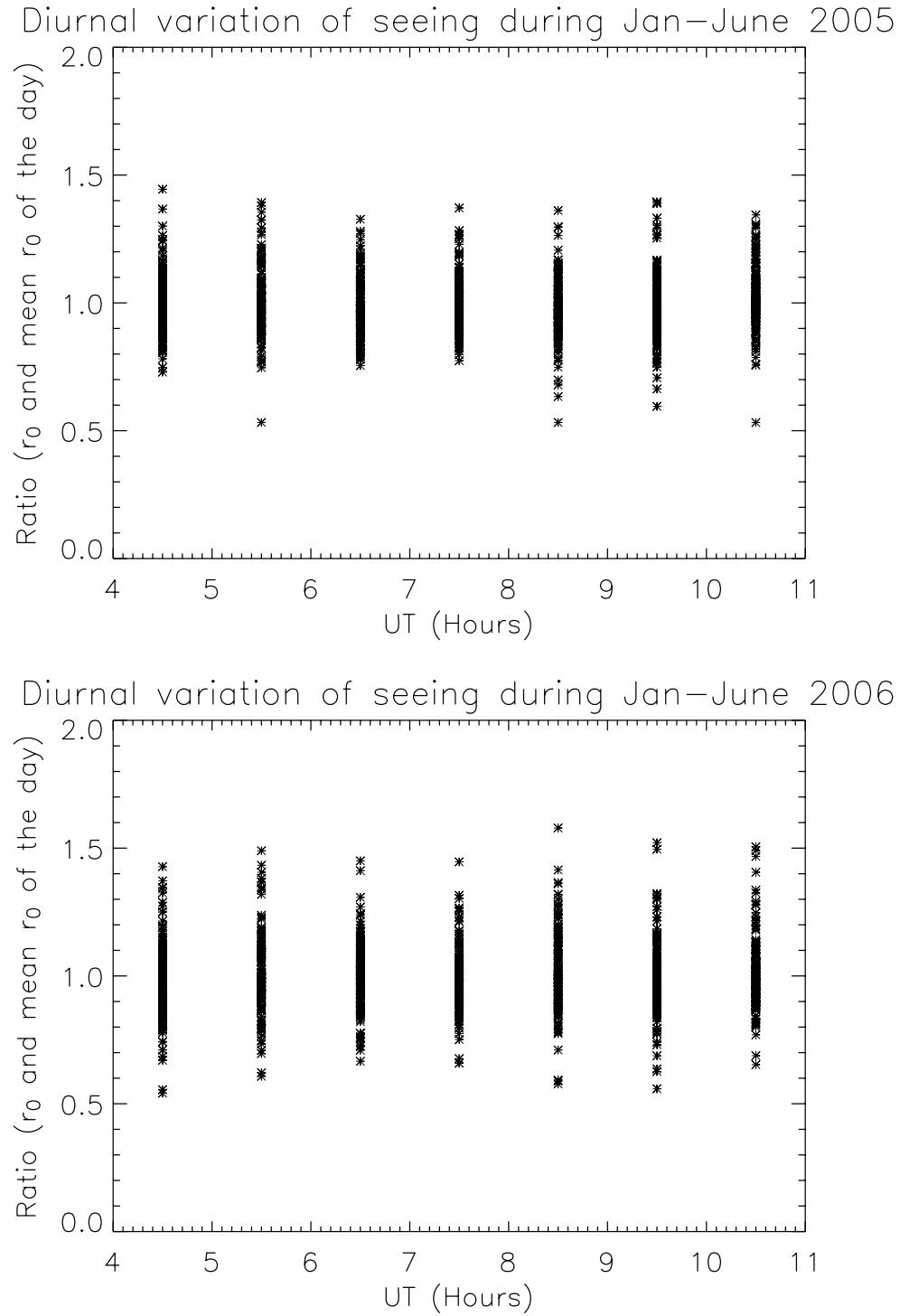


Figure 2.8: The plots show the diurnal variation of seeing between 04:30–10:30 UT weighted by mean value of  $r_0$  for each day during the months of January–June. The *top panel* is showing the aforesaid quantity for the year 2005 while the *bottom panel* shows that for 2006.

in summer. This lack of improvement could be attributed to the late onset of ground turbulence in filled-lake situation. Figure 2.7 in fact shows that the difference of ground turbulence (other components cancel out) between dry and filled situations initially increases and then decreases, however remaining always positive. Thus, we can safely conclude that the effect of the lake is: (1) to improve the seeing, and (2) to extend the number of days of good seeing over a year. Figure 2.8 shows the scatter plot of  $r_0$  normalized by mean  $r_0$  of each day. The normalization is necessary to reduce the effect of day to day variation of mean  $r_0$ . Both panels show no systematic diurnal variation. On the other hand, Beckers and Mason (1998), Beckers (2001), and Beckers, Liu, and Jin (2003) find an extended period of good seeing during the day at lake sites in comparison with mountain sites. It therefore seems that a flat terrain, as available at our site, produces less systematic diurnal behaviour, compared to a mountain site, irrespective of the presence or absence of water in the lake.

There is a more practical lesson that we learn from our study. Hitherto, most site surveys (e.g., Hill *et al.* (2006)) used scintillometry for monitoring the seeing since the scintillometers are eminently portable. However, our study establishes the efficacy of using small imaging telescopes even for the initial surveys. This is because modern  $H\alpha$  filters e.g., Coronado solar filters (<http://www.coronadofilters.com>) are relatively inexpensive and can be easily attached to the entrance aperture of compact telescopes designed for solar observations, which are available with such manufacturers. Further, CCD prices are also declining. Hence, small telescopes, equipped with  $< 1$  Å entrance filters centered at  $H\alpha$  and fast CCD cameras could be readily deployed for measuring  $r_0$  in an unambiguous manner. For exceptionally good sites where  $r_0 > D$ , the telescope aperture, we can register large FOVs and then use angle of arrival fluctuations within isoplanatic patches to estimate  $r_0$ . Another lesson learnt from our study is that our dome contributes nearly 2 arc-sec of seeing. This estimate arises from the square root of the difference of the squares of best and worst seeing for both the years. Thus, we can expect the mean seeing to be about 2 arc-sec at the lake site of USO by observing without the dome.

This has been planned for MAST. The local government has also planned to maintain the water level in the lake through ambitious water supply projects for Udaipur.

# **Chapter 3**

## **Development of an Image**

## **Stabilization System for solar**

## **observations at Udaipur Solar**

## **Observatory**

### **3.1 Introduction**

Atmospheric turbulence causes rapid random motion of the images at the focus of ground based telescopes. This leads to a degraded image in a typical long exposure image lasting a few seconds. Techniques like speckle imaging perform post-processing of noisy short exposure images and have proven capability of achieving diffraction limited imaging. Adaptive optics attempts to correct for the degradation caused by the atmosphere in real time using opto-mechanical elements. As a result, in the case of point sources, it is possible to focus the light over a small area in the focal plane of the telescope for a long duration and thus ability to sense faint stars over the sky background is enhanced. In addition to the high spatial resolution, the possibility to stabilize images at the entrance slit of spectrographs renders high signal to noise ratio and spectral resolution. Even a rudimentary adaptive optics system correcting for

the image motion alone is capable of achieving diffraction limit under good seeing conditions.

In an image stabilization system (also known as tip-tilt or correlation tracking system), a small portion (typically  $10 \times 10$  arc-sec<sup>2</sup>) of a short exposure (typically  $< 10$  ms) image is cross-correlated with a previously recorded reference image. Subsequent images are correlated with the same reference image. This reference image needs to be updated within the time scale of evolution of the solar feature used as a reference. However atmospheric conditions change more rapidly than the time taken for the feature to evolve hence we change the reference image every 10 s or so to make best use of the atmospheric conditions. The cross-correlation extracts the shift of the instantaneous image with respect to the reference image in two orthogonal directions. These shifts are used to calculate and feed appropriate voltages to the piezo-actuators driven tip-tilt mirror so that its surface closely approximates to the instantaneous global tilt of the wave-front. As the global tilt is removed from the wave-front, after being reflected off the mirror, the random image motion is arrested. This results in a stable output in the science camera and thus allows for long exposures.

Several solar adaptive optics systems are either developed or being developed at various observatories around the world (Rimmele, 2000; Scharmer *et al.*, 2003; von der L  he *et al.*, 2003; Keller, Plymate, and Ammons, 2003). Unlike stellar adaptive optics systems, most of the solar adaptive optics systems operate in the visible region of the electromagnetic spectrum. The scintillation is normally ignored, while the global tilts of the distorted wave-front are corrected with the help of tip-tilt mirror system and the local tilts are corrected using deformable mirrors which are available in the form of either thin membrane mirrors or solid bi-morph mirrors. A special aspect of solar adaptive optics systems is that the region of scientific investigation itself -usually small scale features (pores, granulations, and small sunspots etc.) riding on an extended background (quiet photosphere/ continuum), is used as the reference in a much wider spectral bandwidth centered away from the spectral region of interest. In spite of the hurdles caused by the day time seeing conditions which are arguably worse

than their night time counterparts, images recorded with robust solar adaptive optics systems coupled with post processing techniques reveal finest details ever seen on the solar surface at visible wavelengths (Scharmer *et al.*, 2002).

Udaipur solar observatory (USO) is located on an island in the middle of Lake Fathesagar ( $24^{\circ}.5$  N,  $74^{\circ}$  E) in Udaipur, Rajasthan, India. The observatory has a 12 foot long spar telescope with a 2250 mm focal length, f/15 refractor, generously gifted by CSIRO, Australia. At present, it is housed inside a dome, at a height of about 10 m above the ground. It is regularly used for observing solar activities (flares, prominences, and filaments) in  $H\alpha$  line since 1975. As described in the Chapter I, since January 2005 this telescope is also being used for the measurement of the atmospheric “seeing” parameter ( $r_0$ ) with an upgraded camera for short exposures (3 ms) and a focussing/ defocussing mechanism that enables recording of flat-field images for each data set (Kumar *et al.*, 2007). Spectral ratio method (von der L  he, 1984) is employed for estimation of  $r_0$ . In addition to the Spar telescope, there is a 15 cm Coud   refractor which served as a platform for building of a multi-slit digital imaging spectrograph for measuring the line-of-sight velocities of mass motions associated with solar flares, eruptive prominences and surges in  $H\alpha$  (Srivastava and Mathew, 1999) and a Fabry-Perot based solar video magnetograph capable of providing near simultaneous measurements of photospheric longitudinal magnetic fields, chromospheric images in  $H\alpha$  and photospheric images in Ca I (Mathew *et al.*, 1998), and also there is a 15 cm Razdow telescope which is used for monitoring of flares and filaments through full disk  $H\alpha$  imaging. Recently, a Solar Vector Magnetograph (Gosain *et al.*, 2006) has become operational at USO.

USO is currently involved in building a Multi-Application Solar Telescope (MAST) for solar observations. As is the case with any of the modern solar telescopes, the MAST would be equipped with an adaptive optics system that operates in the Visible and Near IR (<http://www.prl.res.in/~uso/mast.pdf>). As a preparatory exercise, a prototype project for developing and demonstrating

the feasibility of a solar adaptive optics system<sup>1</sup> at USO was started in January 2003. As a preparatory exercise, a prototype project for developing and demonstrating the feasibility of a solar adaptive optics system at USO is under progress.

As far as the laboratory demonstration of the adaptive optics system is concerned, in the first phase, an Image Stabilization System (ISS) i.e., a tip-tilt system that corrects for the lowest order wave-front aberration has been demonstrated. In this Chapter, the details of this proto-type tip-tilt adaptive optics system are described, which has been successfully demonstrated (Sridharan *et al.*, 2005; Kumar *et al.*, 2005). In the second phase, the development of an adaptive optics system that includes wave-front sensing and correction using a membrane mirror is in progress (Raja Bayanna *et al.*, 2005, 2007).

## 3.2 Optical setup

A clean laboratory space was developed in September 2003 in the main campus of USO for performing experiments needed for the practical realization of an adaptive optics system. The required adaptive optics system components (wave-front sensors, correctors and control computer) and auxiliary equipments (optics table and opto-mechanical components, lenses and mirrors) were purchased over the next nine months. The 15 cm Coudé telescope was relocated from the island to the USO main campus in May 2004. Figure 3.1 shows the telescope tracking the Sun during a typical observing run. A 50 mm diameter mirror mounted on an additional bench attached to the telescope reflects the diverging beam from the focus towards the laboratory. A doublet lens of focal length 1000 mm, mounted on a separate bench close to the telescope, collimates the beam. Another doublet of focal length 2000 mm focuses the collimated beam inside the laboratory. Thus, the 20.9 mm diameter primary image of the Sun is re-imaged inside the laboratory with a magnification of

---

<sup>1</sup>which would be modified suitably to: (1) meet with the MAST AO system requirements, and (2) keep in pace with the advancement of the technology in wave-front sensing and correcting and the human expertise gained during the development.





Figure 3.1: 15 cm Zeiss Coudé Telescope being used as the light feed for prototype adaptive optics at USO. In addition to the telescope, a 50 mm diameter mirror and two 150 mm diameter doublets used for relaying the primary image to inside the laboratory are also shown. The telescope, supporting optical benches, shelter and side wall of the building are all painted with matt finish white paint rich in  $\text{TiO}_2$  so as to maintain the surfaces close to the ambient air temperature.

three. The telescope, the supporting optical benches used for mounting mirror and lenses, the protecting shelter and the side wall of the laboratory are painted with matt finish white paint ( $\text{TiO}_2$  abundant) that keeps the surfaces close to the ambient air temperature throughout the day.

Figure 3.2 shows the schematic of optical setup inside the adaptive optics laboratory. A portion of the image is collimated by a doublet of focal length 200 mm. The collimated beam is first reflected by the tip-tilt mirror and then by a plane mirror and is finally focussed by another lens of focal length 300 mm. A beam splitter splits the converging beam equally into two parts; one beam is directed to a ‘science camera’ after passing through a filter of 1 nm bandwidth centered at 430.5 nm and the other beam is directed to the ‘wave-front sensing camera’ after passing through a filter of 20 nm bandwidth

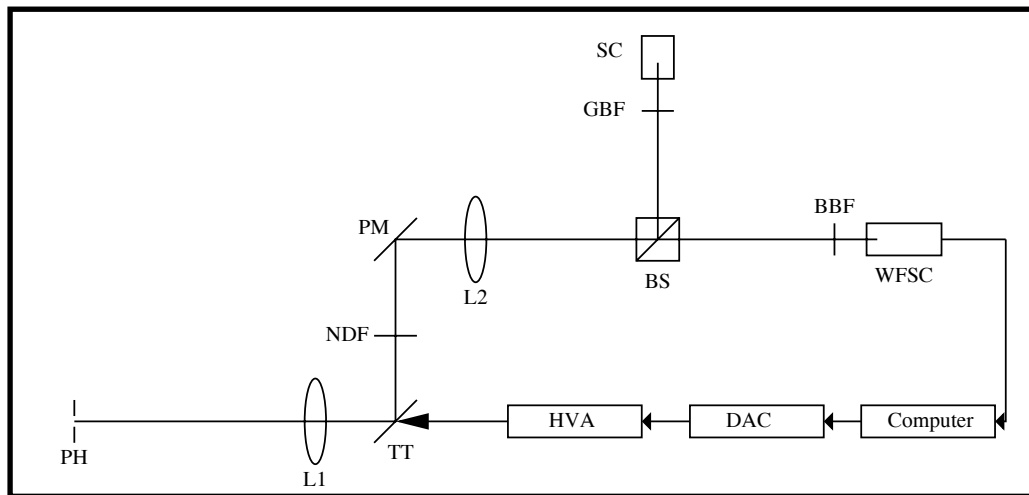


Figure 3.2: Schematic of the optical layout inside the adaptive optics laboratory. The image of the full-Sun is available at the plane of the pinhole (PH). Only a portion (about an arc-min in the current setup) of this image, mostly containing a sunspot is used for the adaptive optics correction. L1 - collimating doublet, TT - tip-tilt mirror mounted on a piezo electric stage, NDF- neutral density filter, PM - plane mirror, BS - beam splitter, L2 - imaging doublet, GBF - G-band filter (430.5 nm, 1 nm pass band), BBF - broad band filter (520 nm central wavelength, 20 nm pass-band), SC - science camera, WFSC - wave-front sensing camera, HVA - high voltage amplifier, DAC - digital to analog converter. The control computer is a 2.4 GHz Pentium 4 processor with 512 KB L2 Cache.

centered at 501.3 nm. Suitable neutral density filters are inserted in the path of collimated beam. The final image has a scale of 0.31 arc-sec per pixel at the ‘wave-front sensing camera’.

### 3.3 Overall description of the system

In this section, we describe the development of both the hardware and software. Almost all the components were bought off the shelf from various manufacturers around the globe. Here we provide the details of these components in order to provide complete specifications of the system. However, such a description should neither be considered as the recommendation of these components by the authors nor be regarded as the best equipments available for this purpose. Also, some of the products described here are presently available with better specifications.

### 3.3.1 Hardware

Apart from optical elements, the main components of the system are: (1) A 2-channel digital to analog converter board, (2) the piezo-electric stage and its controller, and (3) data acquisition system which consists of a fast camera and a frame-grabber card.

#### 3.3.1.1 Digital to analog converter

We use a 16 bit PCI data acquisition board from *Iotech*. It has several channels of 200 kHz analog to digital converters and two channels of 100 kHz digital to analog converters. It operates in the voltage range of -10 to +10 V. The software for using the board on Linux platform is freely available. Portions of the software necessary for initializing the device and sending the analog outputs have been integrated with the ‘universal tracker software’ being used for operating the adaptive optics system.

#### 3.3.1.2 Piezoelectric stage, its controller and mirror assembly

We use a two axes, three actuators fast piezo electric tilting stage (PZT) along with its control electronics provided by *piezosystem jena GmbH*. It is capable of producing 8 milli-radian tilt on both the axes and has a resonant frequency of 1.2 kHz. It operates in the voltage range of -10 to +150 V. It is insensitive to temperature variations and can operate in the range of -20 to +80 °C. The Daqboard converts the digital voltage of the two channels to analog and feeds them at the two modulating input channels of the piezo-electric stage controller. The controller amplifies the voltages by a factor of 15.8, adds the corresponding base voltages (which is set as -10 V in its left most position) and outputs the resulting voltages to the two orthogonal axes of the piezo-electric stage. The base voltages can also be adjusted for a given modulation input voltage. Thus, the piezo electric stage can be controlled both manually and through computer interface.

### 3.3.1.3 Data acquisition system

The data acquisition system consists of a fast camera (wave-front sensing camera) from *DALSA* and PC-DIG<sup>TM</sup> frame grabber board from *CORECO IMAGING*. The camera has frame-transfer architecture, uses IA-D6 sensor, and has 260×260 square pixels of 10 micron size. Each line of the digital data is split into 4 channels and each part is simultaneously read out at a speed of 25 MHz. In the free-running mode, the camera delivers images at a frame rate of 955 fps. The power supply for the camera was made in-house at USO. In the frame grabber, the images are acquired in a linearly addressed, single-ported 64 bit SGRAM buffer of 4 MB capacity, with a bandwidth of more than 250 MB/s and a 64 bit data bus. Data are transferred in ‘packets’ of 8 bytes (or 8 pixels at a time). The device-driver for the frame-grabber card on Linux platform, called *ITIFG<sup>TM</sup>*, was provided freely by *GOM (Gesellschaft Für Optische Messtechnik) mbH*. When operated in memory-mapping mode, the driver is capable of capturing and displaying images at the rate of 955 frames per second, thus enabling capturing of consecutive images.

## 3.3.2 Software

The adaptive optics system software consists of two *C*-programs that are executed together and share a common memory through inter process communication mechanism. The first one, called “the universal tracker” is largely based on the Linux device driver of the frame grabber card provided by *GOM mbH*. The second one, called “the control software”, is used to control the various parameters of the system. The details of these softwares are described below.

### 3.3.2.1 Universal tracker

The initial version of the “universal tracker software” developed for the low cost adaptive optics system at National Solar Observatory, Kitt Peak, USA (Keller, Plymate, and Ammons, 2003) based on earlier driver version (itifg-0.7.2) was

upgraded with the latest version (itfg-8.1.0.8). Particularly, the program that acquires and displays images while running in memory mapping mode was modified and used. The modifications include: (1) removal of unwanted options present in the test program provided by *ITIFG<sup>TM</sup>*, (2) inclusion of suitable device initialization and control options that are specific to our system, (3) implementation of three modes of operation of the tip-tilt system (see below), (4) initialization of shared-memory access for enabling communication with ‘control software’, (5) soft real-time scheduling for avoiding delays due to *time-sharing*, (6) initializing tracking areas on the detector and control parameters, (7) inclusion of dark and flat corrections and the capability to select the best frame from a set of frames based on *rms* contrast, and (8) inclusion of *PID* type controller for the adaptive optics system along with the capability for resetting the piezo-electric stage to the base voltage automatically for abnormal input voltages.

The ‘universal tracker’ can be operated in three modes, namely, spot tracking, N–S ( $x$ ) and E–W ( $y$ ) limb tracking and correlation tracking. In the spot tracker mode, the central portion of the camera is “divided” into four quadrants and isolated sunspot, if available, is centered at the center of the camera. The  $x$  and  $y$  components of the motion of the sunspot, as it moves due to atmospheric turbulence, is estimated using the relative changes in the brightness in the two halves of the detector within boundary of the quadrants in  $x$  and  $y$  directions, respectively. If the total intensity in the lower left, lower right, upper left and upper right quadrants are denoted by  $a, b, c$  and  $d$  respectively and if the sum of the intensities in all the four quadrants is denoted by  $P$ , then,  $x$  component of the image motion is  $(a - b + c - d)/P$  and the  $y$  component of the image motion is  $(c - a + d - b)/P$ . In the limb tracking mode, the camera is “divided” into three halves and a small portion of the limb of the Sun is carefully aligned either horizontally or vertically along the center of the camera. In the horizontal (or vertical) limb tracking, the  $y$  (or  $x$ ) component of the image motion is estimated as the difference between the total intensity

in the central region ( $c$ ) and the total intensity in the upper ( $a$ ) and lower ( $b$ ) halves (or right and left halves) normalized by the total intensity in upper and lower halves ( $a + b$ ). Mathematically,  $\delta y$  (or  $\delta x$ ) =  $(c - (a + b))/(a + b)$ . The sign of the displacement is found by initial trial for a given optical set-up. Though operating in the spot and limb tracking modes is faster, these modes have restricted usage in real applications. Hence, we operate mostly in the correlation tracker mode which is suitable for arbitrary structures.

In correlation tracker mode, the sum of absolute difference of the current image and the reference image (taken in the previous 10 or 30 seconds, depending on the seeing conditions) is estimated for various possible shifts ( $\pm 14$  pixels) and the shift for which this sum is a minimum is considered as the relative shift of the current image with respect to the reference image. The algorithm itself is implemented using the MMX technology instructions (<http://www.pcguide.com/ref/cpu/arch/int/MMX-a.html>; <http://www.tommeseani.com/MMX>), which allow us to estimate the shifts in less than 1 ms time. We are using PSADBW (Packed sum of absolute difference byte word) for implementing our algorithm. The advantage in using PSADBW is that it allows for finding sum of absolute differences of 8 pixels simultaneously in the registers available in Intel Pentium-IV processors. Thus, the shift estimation is done without storing the images on the disk and thereby helps in doing it very fast as described above. Finally, both, the code for estimation of shifts and image acquisition system which acquires images at the rate of 955 frames/sec, allow us to operate the tip-tilt system with higher bandwidth. One of the attractive features of this correlation tracking mode is its ability to track (estimate the relative shift between the reference and current image) over a large array size as big as  $256 \times 256$  pixels. This has been possible on account of two reasons. The first is that PSADBW allows for finding sum of absolute difference of 8 pixels simultaneously, thus increasing the speed of calculations. The second reason is to do with the way of implementation of the search grid for correlation track-

ing: To start with, a pixel shift of (1,1) is assumed and the sum of absolute difference is obtained for all the shifts that are two pixels away from (1,1) in all the eight directions. This leads to a search grid size of 25 pixels (but actual search is for 9 points only). When the minimum is found at a certain pixel, the new search is started in another search grid of 25 pixels surrounding that pixel. When two consecutive searches result in the minimum for same pixel shift, that pixel shift is assumed to be the actual shift. This procedure leads to the simultaneous estimation of the pixel shift between the images in both  $x$  and  $y$  directions with  $\pm 2$  pixel accuracy. However, this accuracy is further improved by using a parabolic interpolation (Press *et al.*, 1993; Niblack, 1986) about three points in  $x$  and  $y$  directions centered at the estimated pixel shift. In open loop, it leads to an accuracy of 0.8 pixels, and it improves further in closed loop due to control algorithm.

### 3.3.2.2 Control software

The control software interacts with the user and also shares a common memory with the “universal tracker”. It allows the user to initialize operations like flat and dark corrections, changing the parameters of the controller, prompting the recording of shift measurements during open and closed loop operations, triggering the recording of reference frames, setting the time interval for automatic reference update, changing the sign of the components of shift vector (it is necessary only at initial stages), prompting the recording of series of shift measurements in the closed loop by jolting the mirror (which enables tuning of the system) and changing parameters of spot, limb and correlation tracker modes. All these operations are performed without stopping the “universal tracker” software. It should be noted that all the actual processes like recording dark and flat are done by “universal tracker” and the control software just controls various actions.

## 3.4 Aperture size, system calibration and tuning

### 3.4.1 Aperture size

Typically, in any adaptive optics system, the wave-front is corrected over the isoplanatic patch size (the angular size over which the wave-front perturbations are highly correlated). A portion of the solar image is magnified and only a field corresponding to an isoplanatic patch (typically 5 to 10 arc-sec) is used for adaptive optics correction. In our case, typically, with an effective magnification of 20, the image scale becomes 0.045 arc-sec per pixel (1 pixel = 10 micron). This leads to an image size of roughly  $10 \times 10$  arc-seconds for the entire  $256 \times 256$  pixels, which is equal to the isoplanatic patch size. However the loss of light level due to such a high magnification leads to a poor signal to noise ratio, since our aperture size is small. After a few trials, we found that an effective magnification of 3 leading to a pixel size of 0.31 arc-seconds works fine for the current setup. The larger iso-kinetic angle (the region over which the average slope of the wave-front remains constant) allows us to track as large as  $80 \times 80$  arc-seconds, though significant anisoplanatic effects could be present. However, this will not be an issue for the proposed 50 cm telescope. At present, we have overcome this problem to some extent by modifying the code such that the cross correlation is performed only for central sub-arrays of various sizes  $128 \times 128$ ,  $64 \times 64$ ,  $32 \times 32$  and  $16 \times 16$ . One of these options can be chosen during compilation of the program depending on the image scale at the 'wave-front sensing camera'.

### 3.4.2 System calibration and tuning

Unlike the Kitt Peak system, which uses a single tuning parameter for both the channels, we tune our control system with different tuning parameters in the two channels. This is because of the unusual behaviour of our piezo-electric system. Here, we describe the calibration of our piezo-electric stage and the



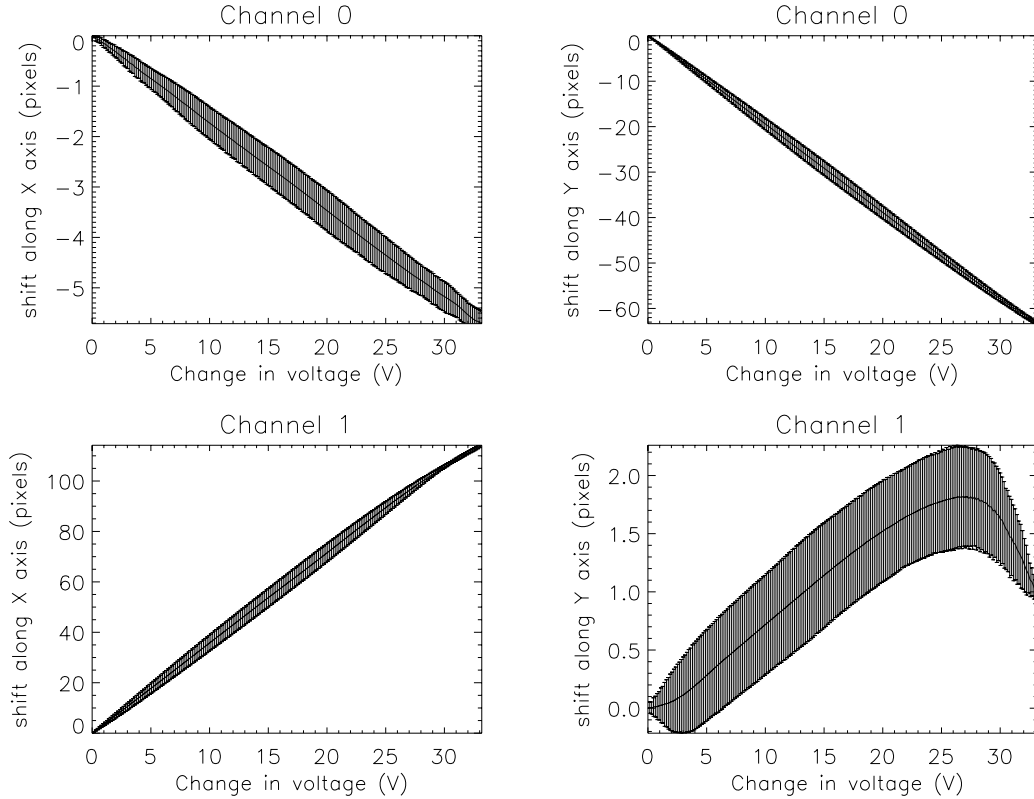


Figure 3.3: Top panels indicate the components of image motion along  $x$  and  $y$  directions as a function of change in voltage applied to *channel 0* when pinhole was illuminated by a laser light. Though the motion is linear along  $Y$  axis, there is a 6 pixel shift along  $X$  axis as the spot moves nearly 60 pixels along  $Y$  axis. The bottom panel indicates similar plots for *channel 1*. In this case, there is 2.5 pixel shift along  $Y$  axis as the spot moves nearly 110 pixels along  $X$  axis. These plots indicate that the response is not identical along the two axes. The error bars indicate  $\pm 1\sigma$  value.

channel-wise tuning of our control system.

The piezo-electric stage was initially tested for linearity and orthogonality using the following procedure. A 0.5 mm spot size laser beam was reflected off the plane mirror glued to the piezo-electric stage and the locus of the reflected beam was traced on a graph sheet by adjusting the base voltage of the controller manually in one of the channels, keeping the voltage of the other channel fixed. It was found that the motion was linear only within a certain voltage range centered around a particular base voltage. The experiment was repeated for the other channel and a similar result was obtained. It was also found that the motion is not orthogonal for the entire range of voltages. By iteration, the base voltages for the two channels were optimized such that the motion is linear and orthogonal within the detector size (2.6 mm). Though such an

optimization (7.2 V for *channel 1* and 86.0 V for *channel 0*, with a base voltage of -10 V) prevented the choice of the middle voltage (80 V for -10 to +150 V) as base voltage, the response (in terms of shift in pixels per unit voltage) was such that there was enough voltage range for  $\pm 30$  pixels shift in each axis for the optical setup shown in Figure 3.2. The top panels of Figure 3.3 show the components of motion of a tiny laser spot at the wave-front sensing camera in units of pixels for various input voltages, centered around the base voltage 86 V for *channel 0* along  $x$  and  $y$  directions along with  $1\sigma$  error bars. Ideally, one would expect to have the  $x$  component to be zero. However, we find a shift of  $\sim 6$  pixels along  $x$  direction as the spot sweeps along the  $y$  axis by 60 pixels. The bottom panel shows similar plots for *channel 1*. Here again, we find a shift of about 2.5 pixels along  $Y$  axis as the spot sweeps along the  $X$  axis by  $\sim 110$  pixels. We also find that the motion along  $y$  and  $x$  directions are completely linear for range of  $\pm 30$  pixels. We observed that the response is not identical in the two channels and there is hysteresis in the piezo electric stage. Such a calibration procedure provides the gain of the system. In our system, the gain was estimated as 107.8 DAC/pixel in *channel 0* and 58.9 DAC/pixel in *channel 1*. However, these values depend upon the optical setup and are not unique.

In a closed loop operation of a tip-tilt system, the correction voltages obtained using this gain correct only for the residual tilt of the wave-front. The actual voltages that corrects for the overall tilt of the wave-front are applied using a time sequence of correction voltages according to a control law that is optimized for accuracy and stability. In a typically used PID controller, the voltage applied to each axis of the piezo-electric stage is: (1) proportional to the estimated shift ( $P$  type controller), (2) varied in time proportional to the accumulated sum of the estimated shift ( $I$  type controller), (3) proportional to the rate of change of estimated shifts ( $D$  type controller). Mathematically, this can be written as

$$V_i = V_{i-1} + Px_i + I \left[ \sum_i x_i \right] + D \left[ x_i - x_{i-1} \right] \quad (3.4.1)$$

where,  $x_i$  is the estimated shift,  $P$ ,  $I$ , and  $D$  are constants that can, in principle, be determined from the open-loop operations. To start with,  $V_i$  is base voltage and the index  $i$  represents  $i$ th value in time. It should be noted that it is not absolutely essential to include all these constants. The process of choosing optimum values for the constants  $P, I$  and  $D$  is called tuning of the control system.

To start with, we employed the standard methods suggested in text books (Murril, 1981; Corripio, 2000) for estimating the tuning parameters. The methods using the open loop response of the system yielded  $P$  values which were consistent with the values evaluated from the gain obtained during calibration. The  $D$  and  $I$  parameters were also obtained from the dynamical properties of the system. While applying the closed loop techniques as recommended in the text books; we encountered a resonance near 70-80 Hz that prevented us from making meaningful estimates of the tuning parameters. We do not know the details of the computer hardware and software timings to eliminate the various phase terms arising out of timing delays. Thus, we used the parameters from open loop techniques as indicative values. Even here, Corripio (c.f. Pg. 29) cautions that the actual values could somewhat be different from the text book values.

We then searched in the parameter space around the “text-book” values and arrived at suitable combinations of  $P$ ,  $I$  and  $D$ . We examined the performance of the system for various parameter values in terms of the bandwidth. Here we define the bandwidth as the frequency at which the ratio of power spectra of “closed” to “open” loop data exceeds unity. We found that the operational bandwidth for the  $P$  alone controller was between 10 to 20 Hz while even modest values of the  $I$  parameter upset the tuning at low frequencies. On the other hand,  $P$ - $D$  controllers showed consistently larger bandwidth as evident from Table 3.1.

Table 3.1: Observed Bandwidth of 70–100 Hz for various runs in the two channels during closed loop tracking of sunspots. The  $P$  and  $D$  values correspond to *Channel 0*. The values applied in *Channel 1* are  $0.45P_0$  and  $0.45D_0$  respectively. The observed *rms* image motion in the closed loop is  $0.1''$  with the improvement varying from 10 to 20 depending on external conditions.

Obs.	Tuning Parameters		Bandwidth		Obs.	Tuning Parameters		Bandwidth	
	$P_0$	$D_0$	$Ch - 0$	$Ch - 1$		$P_0$	$D_0$	$Ch - 0$	$Ch - 1$
runs					runs				
1	020	040	100	100	15	020	073	80	99
2	020	040	105	80	16	020	074	100	109
3	020	045	100	100	17	020	075	100	75
4	020	055	100	100	18	020	075	97	102
5	020	065	100	100	19	020	078	118	100
6	020	070	100	103	20	020	078	100	100
7	020	070	100	100	21	020	079	126	100
8	020	070	99	75	22	020	079	100	100
9	020	070	80	77	23	020	080	100	92
10	020	071	75	86	24	020	080	96	71
11	020	071	73	81	25	020	080	82	78
12	020	071	119	70	26	020	085	100	98
13	020	072	100	100	27	020	085	80	79
14	020	072	100	82	28	020	085	120	100

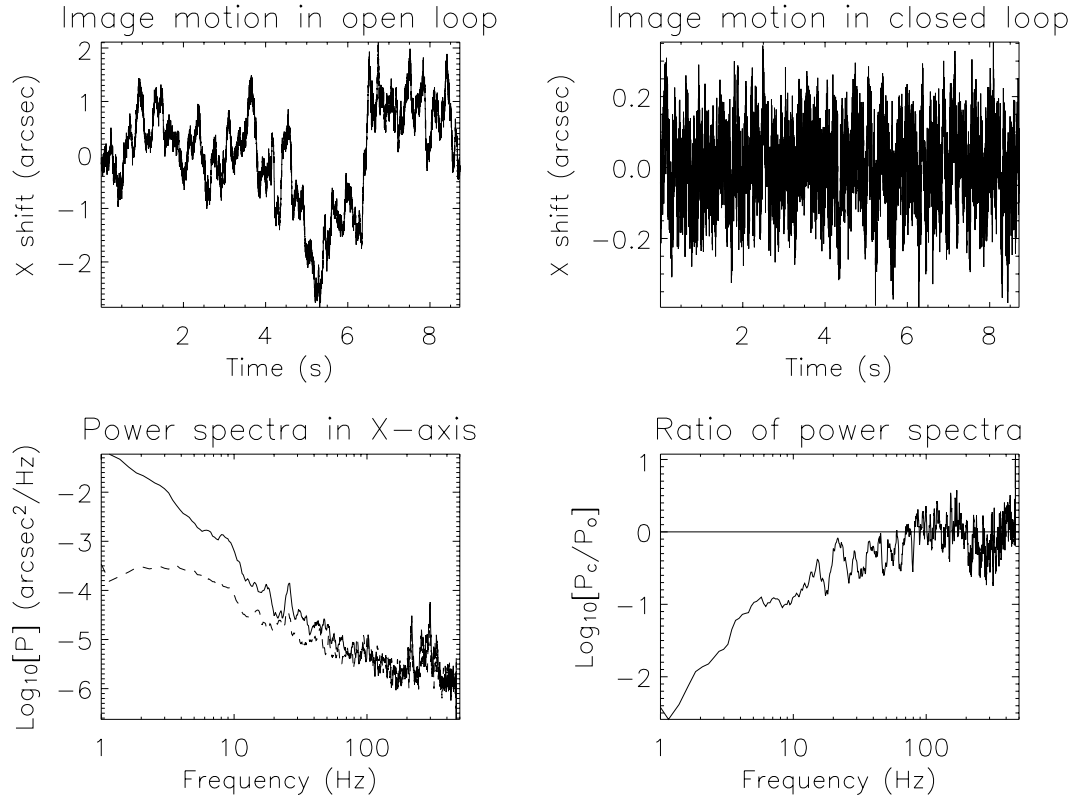


Figure 3.4: Left top: Image motion along  $X$  axis in open loop. Right top: Image motion along  $X$  axis in closed loop. Left bottom: Power spectra of image motion along  $X$  axis in open and closed loop. Right bottom: Ratio of closed loop and open loop power spectra.

### 3.5 Results and Discussions

The top panels of Figure 3.4 indicate the  $x$  component of image motion over a period of 8 seconds with the control-loop turned *off* and *on* respectively. It is clear that in the open loop tracking, in addition to the atmospheric image motion, there is considerable slow variation, which could be attributed to imperfect tracking of the telescope.

Following Equation (6) of Ballesteros *et al.* (1996) we can write the expected error  $e(t)$  after closing the loop as

$$e(t) \approx \frac{dp(t)}{dt} \cdot \tau \quad (3.5.1)$$

where  $p(t)$  is the “open loop” variation and  $\tau$  is the total delay time including

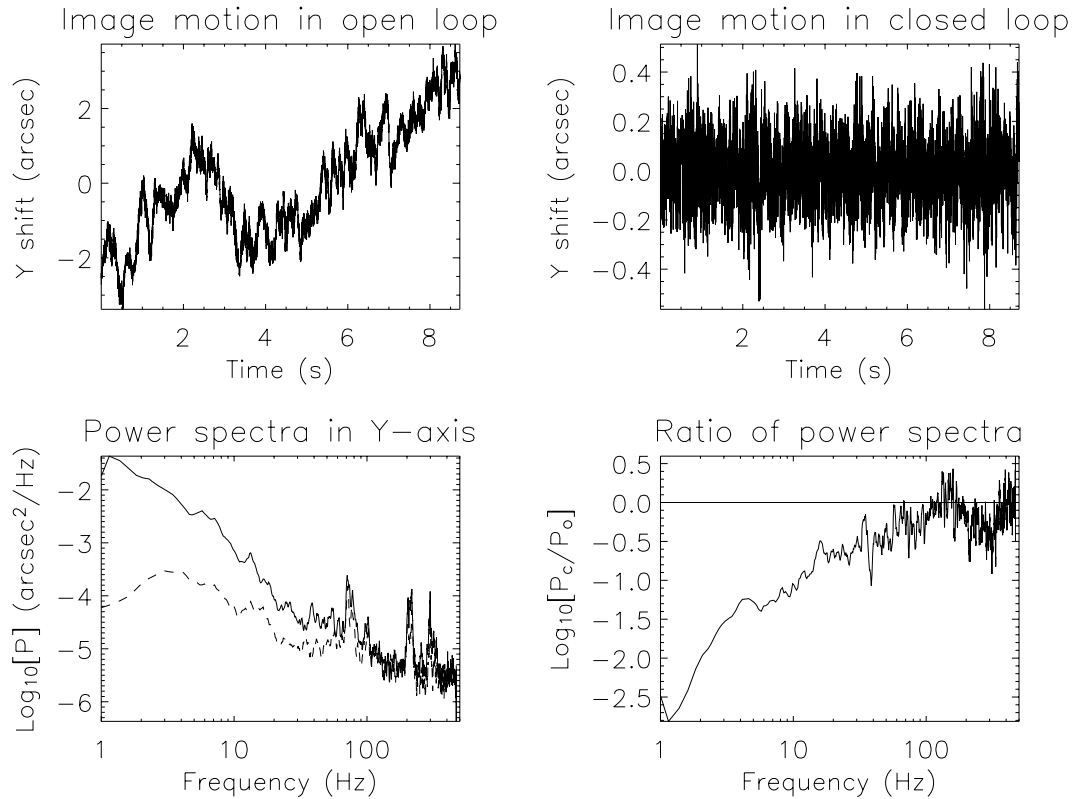


Figure 3.5: Left top: Image motion along  $Y$  axis in open loop. Right top: Image motion along  $Y$  axis in closed loop. Left bottom: Power spectra of image motion along  $Y$  axis in open and closed loop. Right bottom: Ratio of closed loop and open loop power spectra.

the sampling time. Fourier Transforming (3.5.1) we get

$$\tilde{e}(\omega) \approx i\omega\tau\tilde{p}(\omega) \quad (3.5.2)$$

The absolute square of (3.5.2) yields

$$\begin{aligned} P_e &\approx \omega^2\tau^2 P_o \\ \text{or, } \frac{P_e}{P_o} &\approx \omega^2\tau^2 \end{aligned} \quad (3.5.3)$$

where  $P_e$  and  $P_o$  are the power spectra of “closed” and “open loop” variations respectively. The slope of the plot of ratio of “closed” to “open” loop power in Figure 3.4 follows Equation (3.5.3) at low frequencies when the total delay time  $\approx$  few ms. The behaviour of the ratio at higher frequencies needs better modelling as suggested by Ballesteros *et al.*, 1996. Table 3.1 shows the bandwidth achieved for various values of  $P$ ,  $I$  and  $D$ . Although the “open” and “closed”

loop data are not co-temporal, they were obtained in quick succession. Moreover, several runs were performed for each set of parameters and results were reproduced in the different runs. A clear result is the improvement of bandwidth seen in a  $P$ - $D$  controller in comparison with a  $P$  alone or  $P$ - $I$  controller. A  $P$  alone controller will iron out the low frequency behavior leaving the residual high frequency variations. The difference of the error terms then produces a signal that is exactly  $180^\circ$  out of phase of the residual high frequency variation. The  $D$  parameter will decide the extent of the cancellation of the high frequency power, when a difference of errors multiplied by  $D$  is included in the feedback of the controller. We were able to achieve the required bandwidth by using suitable values of  $D$ . However we see several ‘spikes’ in our “closed” loop power spectra which could not be completely suppressed. Such spikes are also seen in the results for various Image Stabilization systems (c.f., panels 2 and 3 of Figure 9, Scharmer *et al.*, 2000; Figure 13, Ballesteros *et al.*, 1996). These spikes are due to various resonances in the system. We conjecture that these resonances are due to the interaction of various time delays. It would be interesting to address these resonances by developing tuning methods more suitable for high frequency operations than what are described in text books on process control.

### 3.5.1 G-band observations using the Image Stabilization System

Using our Image Stabilization System, we have taken the observations of solar active region NOAA 10923 on 15 November, 2006 with the help of a G-band filter ( $\lambda = 430.5$  nm ;  $\delta\lambda = 1.0$  nm). Here, we present a comparison of the mean images constructed from a burst of 100 frames obtained by our ‘science camera’ with 3 ms exposure in the G-band (Figure 3.6) with the control-loop turned *off* and *on*, respectively. The improvement in image quality seen in the closed loop operation is obvious. The best frame from these is also shown in to demonstrate the quality of the imaging system during times of minimum

atmospheric degradation. For the present, we have realized a system that has a bandwidth sufficient to handle atmospheric fluctuations in the visible region.

### 3.5.2 Estimation of atmospheric “seeing” using G-band images

The aforesaid short exposure (3 ms) G-band images have been used to estimate atmospheric “seeing” in both the situations, control-loop turned *off* and *on*, respectively. Spectral ratio method (von der Lühe, 1984) has been used to estimate  $r_0$  in open and closed loop operations using the burst of 100 short exposure G-band images. For both the cases, open loop and closed loop operations, the sequence of 100 images are registered before performing the analysis.

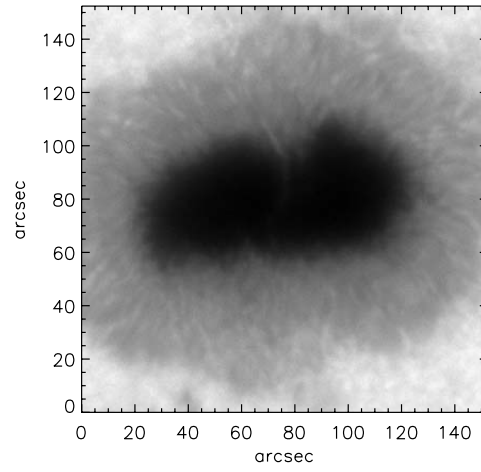
As has been described in Chapter II, the ratio of the squared modulus of the FFT of mean image and the mean of the squared modulus of FFT of the individual images can be represented by  $S$  as follows:

$$S = \frac{|\langle FT[Image] \rangle|^2}{\langle |FT[Image]|^2 \rangle} \quad (3.5.4)$$

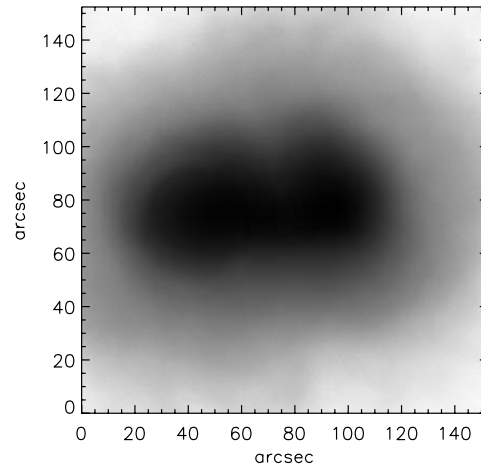
$S$  depends on the seeing conditions that prevailed during the period of observation. This ratio  $S$  allows us to extract the normalized atmospheric cut-off frequency  $f_c$  (c.f., Equations (3) and (4), von der Lühe, 1984) from the burst of high resolution images. The Fried’s parameter  $r_0$  is given by  $f_c D$ , where  $D$  is the aperture of the telescope. The parameter  $f_c$  for the aforesaid open loop and closed loop observations is illustrated in Figure 3.7. The value of  $r_0$  obtained from open loop observations is  $\sim 2.65 \pm 0.08$  cm and that for closed loop observations is  $\sim 4.20 \pm 0.12$  cm. This illustrates the successful operation of our tip-tilt system.

In summary, we have realized an Image Stabilization System using a tip-tilt mirror with a digital *PID* controller. The system has a closed loop correction bandwidth in the range of 70 to 100 Hz. The root mean square image motion in the closed loop is about 0.1 arc-sec and is better than that in the open

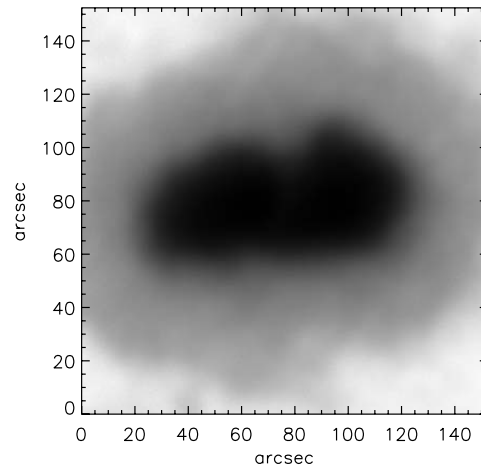




(a)



(b)



(c)

Figure 3.6: The images show: (a) typical short exposure (3 ms) observation of a sunspot (active region NOAA 10923) taken on 15 November 2006, in G-band (430.4 nm) with a 1.0 nm bandpass filter using the Coudé telescope and lab setup for Image Stabilization System at USO; (b) average image obtained from the aforesaid 100 images taken in the open loop; (c) depicts the average image in the closed loop. The improvement in image motion in closed loop leading to better average image from the burst of images is clearly seen.

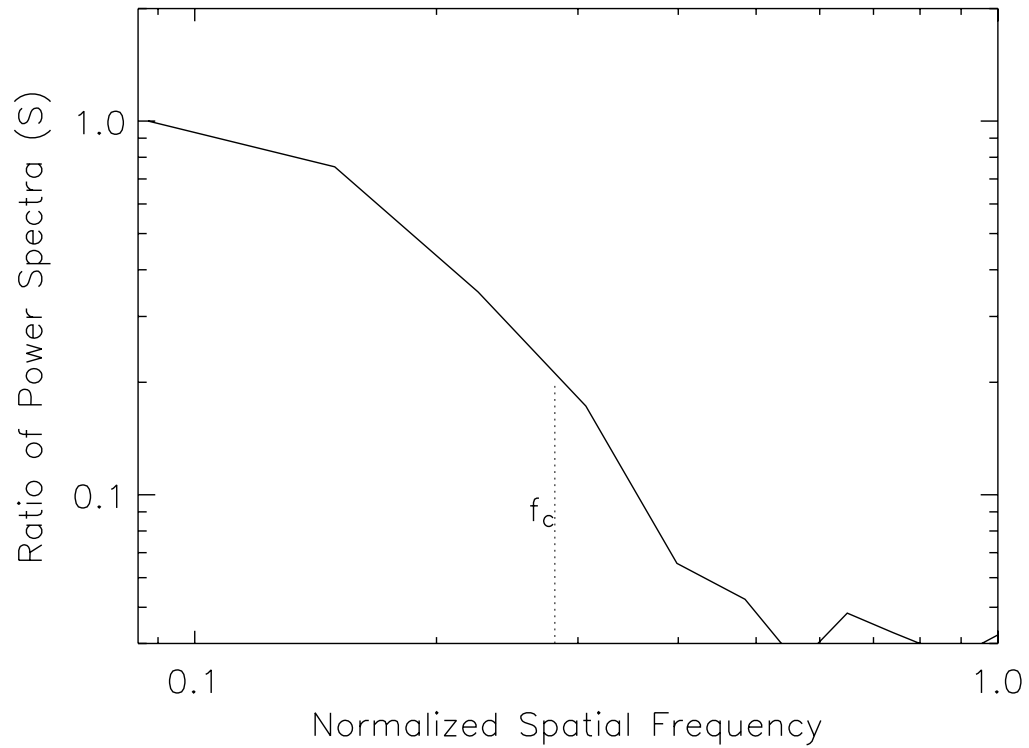
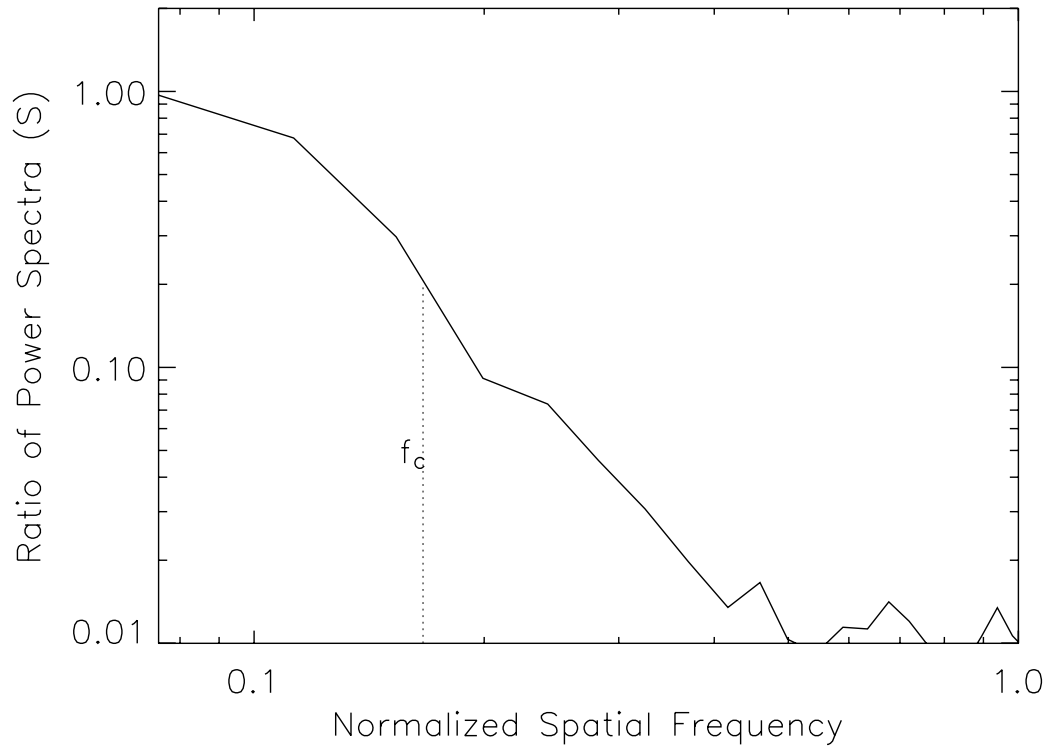


Figure 3.7: Top panel: Plot of  $S$  (c.f., Equation (3.5.4)) v/s normalized spatial frequency in open loop observations. Bottom panel: Same as above, but for closed loop observations. The normalized atmospheric cut-off frequency ( $f_c$ ) is indicated in the plots.

loop operation by a factor of 10 to 20. We followed basically the approach of Keller, Plymate, and Ammons (2003) with appropriate modifications in software and hardware. A careful survey of tuning methods provided a useful insight into how these methods could be implemented in practice. We have also demonstrated how resonances in the system can be damped by proper tuning.

### 3.6 Limitations and Future plans

The present system has several limitations and we plan to improve upon it in future. One of the serious limitations is the inability to operate within a field of view as small as 5-10 arc-sec (arguably size of a typical isoplanatic patch, for day time seeing conditions). This is partly due to the poor tracking and partly due to using aperture as small as 15 cm. Typically, with an effective magnification of two, the image scale becomes 0.45 arc-sec per pixel (1 pixel = 10 micron). This leads to an image size of roughly  $2 \times 2$  arc-min for the entire  $256 \times 256$  pixels, which is much larger than the isoplanatic patch size. At present, we can operate in sub-array mode of as small as  $16 \times 16$ . However, we find it extremely difficult to operate in this mode for long duration, particularly with the present imperfect tracking under windy conditions. A magnification of 20, though allows to accommodate about  $10 \times 10$  arc-sec within the  $256 \times 256$  pixels, the loss of light level due to such a high magnification leads to a poor signal to noise ratio. After a few trials, we found that an effective magnification of 3 leading to a pixel size of 0.31 arc-seconds is optimum for the current setup. The larger iso-kinetic angle (the region over which the average slope of the wave-front remains constant) allows us to track as large as  $80 \times 80$  arc-seconds, though significant anisoplanatic effects could be present. However, we hope that this will not be an issue for the proposed 50 cm telescope, as is case with any of the large solar telescopes. The second important limitation is the inability to track longer than a maximum of 30 seconds. While, this is partly dependent on the seeing conditions, we expect further improvements after in-

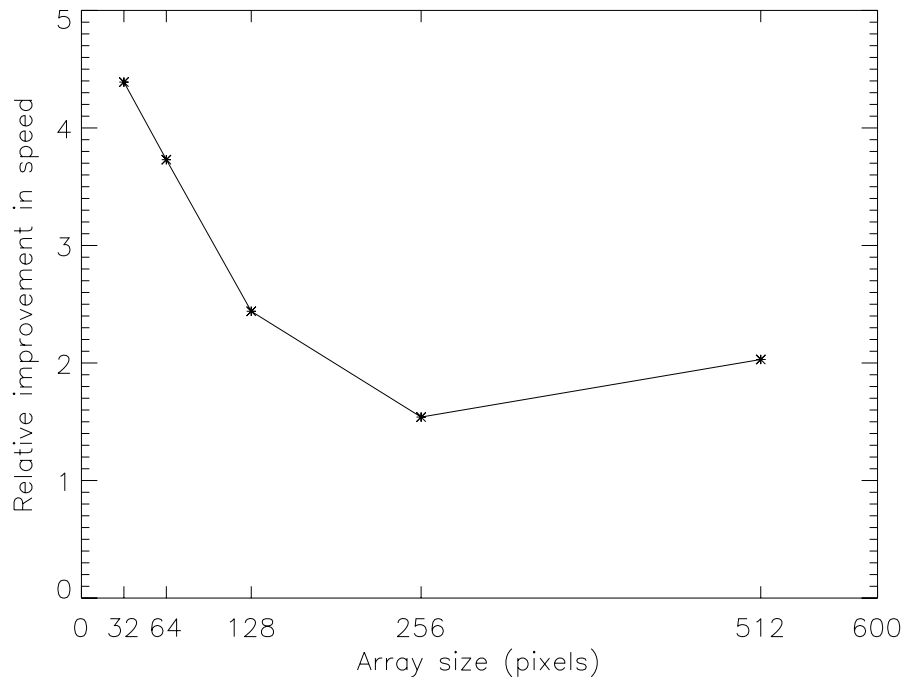


Figure 3.8: Relative improvement in speed of FFTW over FFT for various array sizes. The bench marking was done with an Intel Pentium 4 processor with 2.4 G Hz speed.

stalling appropriate guider for the telescope. The third limitation is that, due to the inability to see granulations, we had to depend on the availability of sunspots and pores on the solar surface to operate our system. The mediocre seeing prohibits running the system with any arbitrary surface of the Sun as reference.

At present, there is a possibility to operate the “universal tracker” in sub-array modes, whereby the correlation tracking is done over sub-arrays of  $32 \times 32$  or  $64 \times 64$  or  $128 \times 128$  or  $256 \times 256$  pixels. Depending on the image scale at the adaptive optics camera, one of these options can be chosen during compilation of the program. We plan to replace the current sum of absolute difference algorithm by the FFT based cross correlation algorithm which has already been developed and tested. If  $C$  and  $R$  represent current and reference image respectively, then the relative shifts  $(\delta x_0, \delta y_0)$  between them is estimated as that for which the cross correlation  $CC$  is maximum. Mathematically, the

cross correlation is estimated using Fourier transforms as

$$CC \left[ \begin{matrix} \delta x, \delta y \end{matrix} \right] = F \left[ \frac{F^{-1}(C) * conj[F^{-1}(R)]}{[P1 * P2]^{\frac{1}{2}}} \right], \quad (3.6.1)$$

where  $F^{-1}$  and  $F$  represent two dimensional Fourier and inverse Fourier transform operators respectively, P1 and P2 represent total power in  $C$  and  $R$  respectively, and *conj* implies complex conjugate. In practice, the slowly varying background is subtracted from each image before performing Fourier transform. The co-ordinates of the maximum are obtained with sub-pixel accuracy using a parabolic interpolation (Niblack, 1986) of three pixels along  $x$  and  $y$  directions centered around the estimated maximum of the cross-correlation function. We have implemented and tested the FFT based cross correlation algorithm using Fastest Fourier Transform in the West (FFTW) routines which indirectly use MMX/SSE2 instructions. Figure 3.8 shows a plot of improvement in speed v/s the array size and it is clear that for array sizes less than  $128 \times 128$  pixels, the speed is increased at least by a factor of two. This feature will be added as an additional compile time option in the adaptive optics software. While the time taken for estimating the relative shift using FFTW based algorithm is equal for all the shifts up to half the size of the array, the time taken for SAD (Sum of Absolute Differences) algorithm is highly dependent on the magnitude of the shift. We found that for an array size of  $32 \times 32$  pixels, both FFTW and SAD algorithms have equal speed. However, we plan to include FFTW based algorithm as a compile time option due to its higher accuracy and its immunity to low signal to noise ratio. In the case of wave-front sensing with smaller sub-aperture images, the effective time for  $N$  number of small arrays is expected to be smaller than a large array and thus we expect that FFTW based cross-correlation might be more efficient in wave-front sensing.

At present, the control software, is being operated through command-line instructions. A graphics user interface has been partly developed on the Linux platform for interactive use and will be implemented soon. We hope to complete these improvements eventually as we migrate towards a robust adaptive

optics system for the MAST.

# Chapter 4

## Analysis of enhanced velocity signals observed during solar flares

### 4.1 Introduction

Solar flares release large amount of energy within few minutes to hours. Apart from high energy radiation, it also produces a large amount of energetic particles which move at high speeds. Several researchers have put their effort to understand the mechanism involved in these explosive events occurring in the solar atmosphere. The major aspect of such investigations involved looking for change in magnetic flux (Lara, Gopalswamy, and DeForest, 2000), change in magnetic shear (Sakurai *et al.*, 1992; Ambastha, Hagyard, and West, 1993; Wang, Xu, and Zhang, 1994; Hagyard, Stark, and Venkatakrishnan, 1999; Li *et al.*, 2000), change in magnetic helicity (Moon *et al.*, 2002) and change in magnetic energy (Metcalf, Leka, and Mickey, 2005), before and after the flares. Apart from searching for the cause of the flare, people have also looked at the consequence of the flares in the solar atmosphere and one chief thrust area has been the study of the effect of a flare on solar oscillations, especially on the  $p$ -mode oscillation frequency and power in the associated active region. These global oscillations are present on the Sun all the time, with maximum power

in the 3 mHz frequency band for velocity oscillations. These global modes are excited by the turbulence in the convective layer. However, reduced velocity power in 3 mHz band is seen in sunspots as compared to the quiet part of the Sun, whereas enhancement in high frequency power in these active regions have been reported (Hindman and Brown, 1998; Venkatakrisnan, Kumar, and Tripathi, 2002) during non-flaring conditions. Sunspots are thus known to absorb the  $p$ -mode power (Braun, Duvall, and LaBonte, 1987), however this situation could well be altered during the flares.

Wolff (1972) suggested that large solar flares can stimulate the free modes of oscillation of the entire Sun. Haber *et al.* (1988) have reported that there is an average increase in the power of intermediate degree  $l$ , after the flare. At the same time, Braun and Duvall (1990) could not detect the excitation of acoustic waves from an X- class flare. Kosovichev and Zharkova (1998) have reported signature of seismic waves (solar quakes) during solar flare. Following this result, Donea, Braun and Lindsey (1999) found an acoustic source associated with a flare using seismic images. They found a considerable flare induced acoustic power in 3.5 mHz band. The flare also induced power in 6 mHz band. Further, they report that 6 mHz flare signature lags the 3.5 mHz by  $\sim 4$  min. Application of ring diagram analysis technique to several flare producing active regions showed that power of  $p$ -modes appear to be larger when compared to that in non-flaring regions of similar magnetic field strength (Ambastha, Basu, and Antia, 2003). Using helioseismic holography technique, Donea and Lindsey (2005) have reported emission of seismic waves from large solar flares which have occurred in active region NOAA 10486 on 2003 October 28 and 29. They found many compact acoustic sources associated with the foot-points of the coronal loops.

In this Chapter, the enhanced velocity signals in NOAA active regions 10486 and 9415 appearing during flares, and co-temporal with the GOES soft X-ray flux, are being studied. These active regions have produced major X-class flares and hence are ideal sites for studying the effect of flares on velocity oscillations. Also, we present each of the selected events in decreasing order of flare strength.



Table 4.1: Active region numbers, date and time of observations, location of the active regions and the X-ray class of the flares are listed below.

S. No.	Active region	Date	Time (UT)	Location	X-ray class
1.	NOAA 10486	2003 Oct 28	06:00–14:59	S17E13	X17.2
2.	NOAA 10486	2003 Oct 29	16:00–23:59	S16W08	X10
3.	NOAA 9415	2001 Apr 06	16:20–23:59	S21E31	X5.6

Fast Fourier Transform based power spectral images have been used to study the acoustic power in the active region in different frequency regimes during the flare event. The next few sections of the Chapter are devoted to the data and its analysis, while the later sections present summary of the results and related discussions.

## 4.2 The observational data

In order to examine the enhanced velocity signals in active regions during the flare, we have used the full disk Dopplergrams observed with a cadence of 60 sec, obtained from the Michelson Doppler Imager (MDI: Scherrer *et al.*, 1995) on-board the Solar and Heliospheric Observatory (SOHO: Domingo, Fleck and Poland, 1995). We chose the data of NOAA active regions 10486 and 9415 for the days 2003 October 28 and 29, and 2001 April 6, respectively, for our study. We have chosen these active regions because they produced large flares on the aforesaid days and hence would provide greater chance for detecting effects clearly discernible of these flares on the acoustic oscillations. We also used the white light images and line-of-sight magnetograms from MDI, 1600 Å images from TRACE, soft X-ray flux data from GOES (1–8 Å) and hard X-ray flux data (100–300 keV) from RHESSI, to complement the MDI Dopplergrams.

The active region NOAA 10486 was one of the largest groups of sunspots observed in the declining phase of solar cycle 23. It appeared on the east limb of the Sun on 2003 October 23 in the southern hemisphere. This complex

active region belonged to  $\beta\gamma\delta$  class and produced several X-class and M-class flares during its passage on the solar disk. The limb flare observed on 2003 November 4 was a X28 flare, which was one of the largest flare ever observed till now from GOES X-ray detector. The other flares were X17 and X10, which occurred on 2003 October 28 and 29, respectively, when the active region was located near the central meridian.

The active region NOAA 9415 was a more compact sunspot group and belonged to the class  $\beta\gamma$ . This also appeared in the southern hemisphere and produced several X-class and M-class flares during its passage on the disk. The one we choose is X5.6 flare, which occurred on 2001 April 6 at 19:21 UT.

The NOAA No. of the active regions, date and time of observations, location of the active regions on the solar disk and the X-ray class of the flares are summarized in Table 4.1. The active region was tracked using heliographic co-ordinates in the full disk Dopplergrams, which were interpolated to a  $1''$  pixel size. The missing data sets were interpolated. A two point backward difference filter was used to remove the low frequency fluctuations. These filtered Dopplergrams were then used for this study.

## 4.3 Analysis and Results

### 4.3.1 Space-time diagrams

In order to identify the temporal changes in the velocity field fluctuations at different spatial locations, we used the space-time analysis technique (Solanki and Rüedi, 2003; Ravindra, Venkatakrishnan, and Kumar, 2004). The space-time diagram for the time series of Dopplergrams has been obtained by selecting a pixel row along  $x$ -direction (as shown in Figure 4.1(a)) and stacking it in time. To identify the location of the slit on the active region, we have shown the magnetogram and the position of the slit in Figure 4.1(c). The magnetic field strength along the slit direction is shown for reference in Figure 4.1(d). Figure 4.1(a) shows the space-time diagram for the 2003 October 28 event. This space-time diagram shows that the oscillations in the regions of weaker

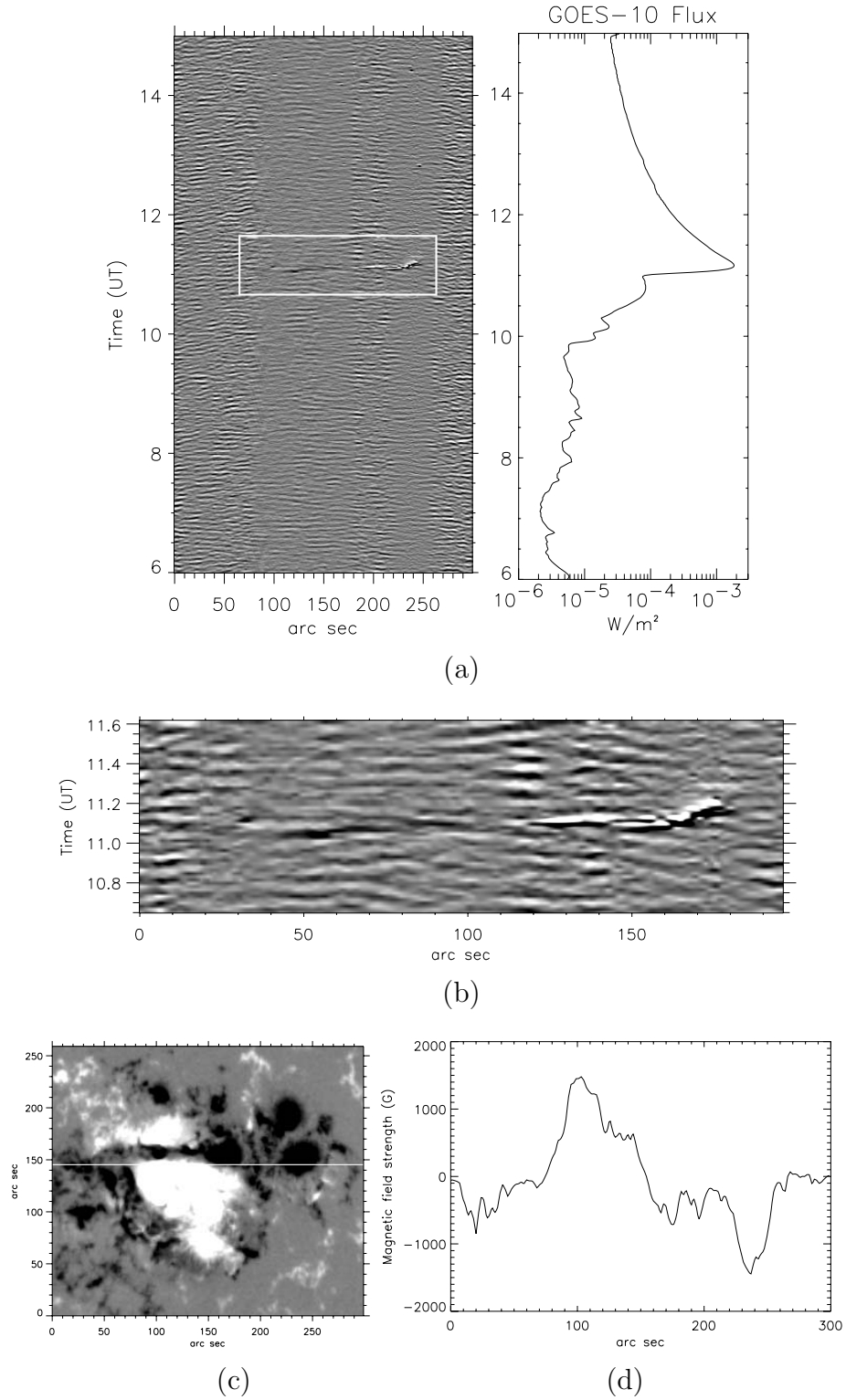


Figure 4.1: (a) Space-time map (left) showing the velocity fluctuations in and around the active region NOAA 10486 obtained on 2003 October 28. The transient changes in velocity signals observed during the flare are marked by the box. The GOES X-ray flux (right) shows the peak time of the soft X-ray emissions. (b) A magnified version of the space-time map inside the aforesaid box to illustrate the transient velocity signals. (c) The magnetogram of the AR 10486 showing the position of the virtual slit from which the space-time map has been made. (d) Magnetic field strength along the slit, showing the position of the strong and weak magnetic field regions.

magnetic fields of the Sun is similar to oscillations seen in the quiet Sun. However, oscillations with reduced strength and of a different kind can be seen in the stronger field regions. The location of the active region (between 80–260 arc sec) is seen as a patchy strip and can be confirmed from Figures 4.1(c) and (d). In the space-time diagram (Figure 4.1(a)), one can also notice that there is an apparent transient change in velocity signals (inside the box) in the active region during the flare (between 11:05–11:10 UT and between 100–250 arc sec). This can be clearly seen against the background oscillations as black and white patch from 120 to 180 arc sec, which is running horizontal to the  $x$ -axis in the magnified version of the space-time map (Figure 4.1(b)). The GOES X-ray flux has been plotted adjacent to the space-time diagram to relate transient changes in the velocity oscillations in the active region with the flare evolution. These GOES X-ray data are recorded in the soft X-rays in the 1–8 Å band with a temporal resolution of 1 min and are good indicators of the thermal energy released in flares. The transient changes in the velocity signals appear to precede the peak time of the GOES X-ray flux.

Figure 4.2(a) shows the space-time diagram for 2003 October 29. The position of the slit is marked on the magnetogram (Figure 4.2(c)). The boxed region in Figure 4.2(a) shows the transient change in the velocity oscillations and its magnified version is shown in Figure 4.2(b). Figure 4.3(a) is the space-time map for 2001 April 6 flare event. Here also, in the magnified space-time map (Figure 4.3(b)) one can notice enhancement in velocity signals in localized position of the sunspot, close to the peak time of the soft X-ray flux.

### 4.3.2 Power maps

We have computed the power maps of the active regions in selected frequency bands in order to examine the enhancement of velocity signals in different frequency regimes and locations. It is well known that the acoustic power spectrum of photospheric oscillations shows a maximum at around 5 minute (3.3 mHz). The band of dominant photospheric oscillations is in the regime of 2–4 mHz, with a decrease to negligible power at higher frequencies in the

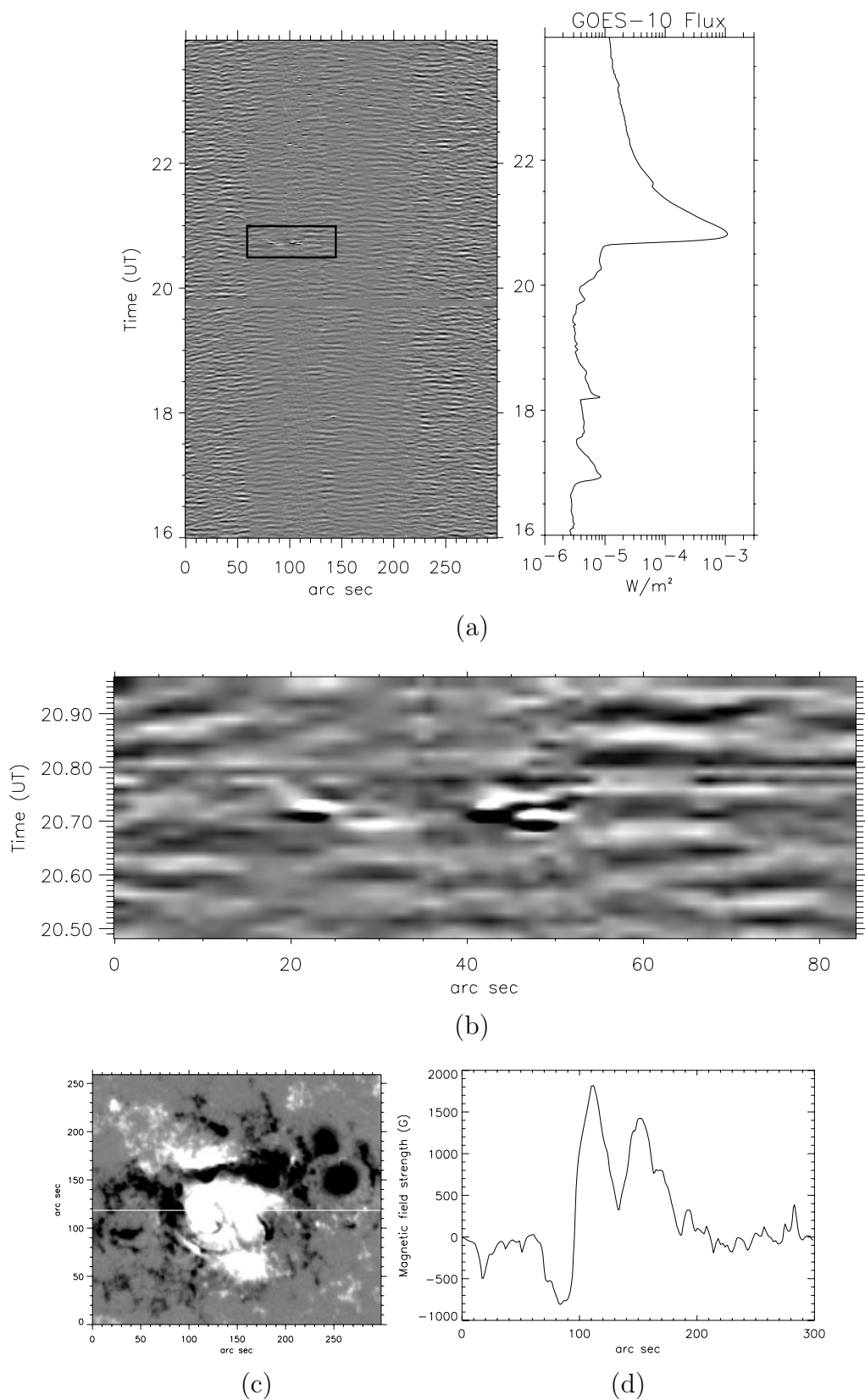


Figure 4.2: Same as Figure 4.1, but for the flare event of 2003 October 29.

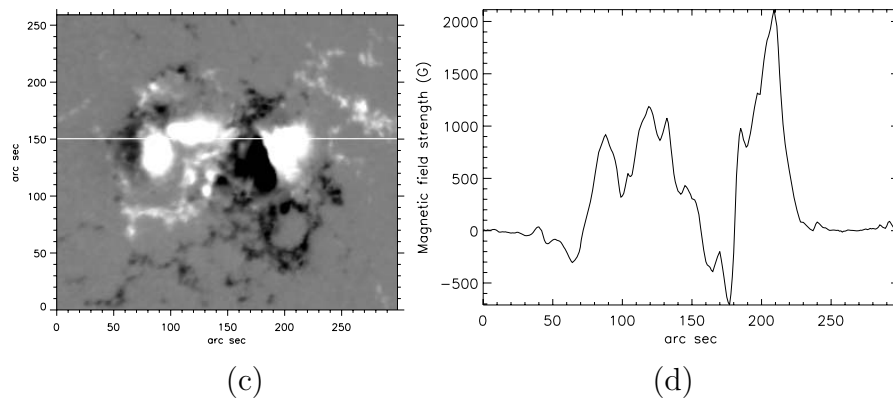
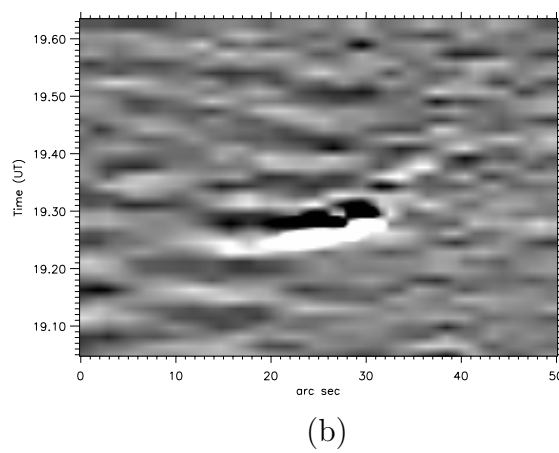
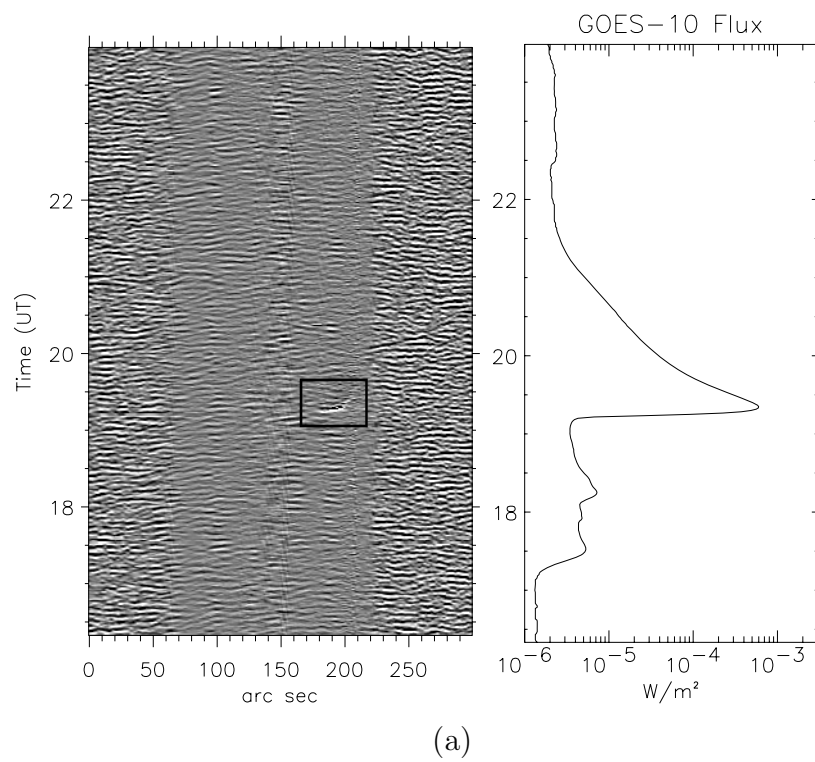


Figure 4.3: Same as Figure 4.1, but for the flare event of 2001 April 6.

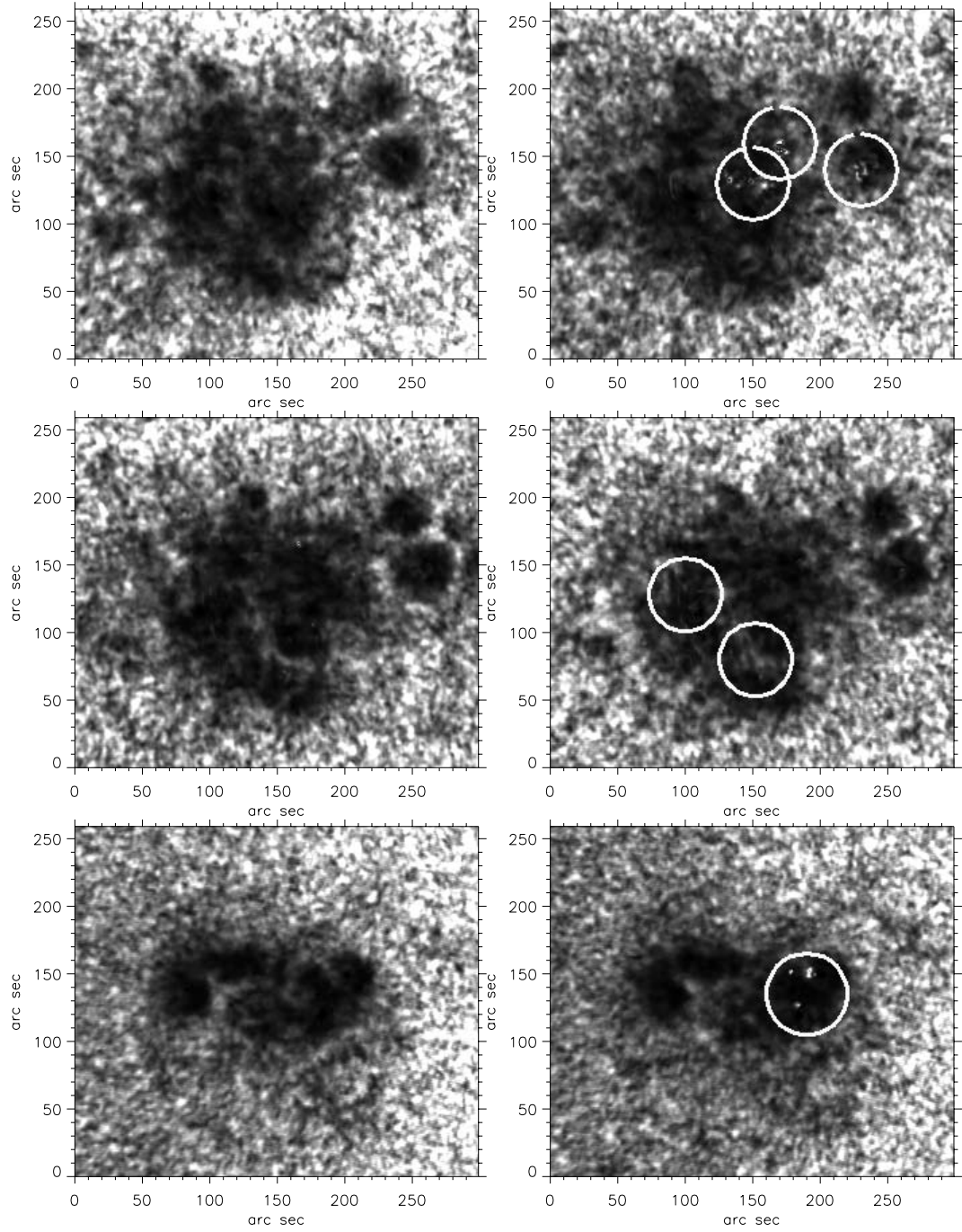


Figure 4.4: Power maps computed from the Dopplergrams for 2003 October 28 and 29, and 2001 April 6 events, from top to bottom, respectively. Left hand side images are power maps obtained by averaging the power in the frequency band 2–4 mHz for time duration of two hours before the flare, while the corresponding right hand side images are those obtained for two hours spanning the flare. The power maps on the left hand side have maximum (minimum) values of power  $83.61 \times 10^3$  (129.6),  $70.673 \times 10^3$  (419.65), and  $85.371 \times 10^3$  (284.273)  $\text{m}^2 \text{s}^{-2}$ , while for the right hand side images the values are  $81.05 \times 10^3$  (250.76),  $69.834 \times 10^3$  (386.14) and  $83.613 \times 10^3$  (405.88)  $\text{m}^2 \text{s}^{-2}$ , from top to bottom, respectively. The encircled regions show the location of enhanced power.

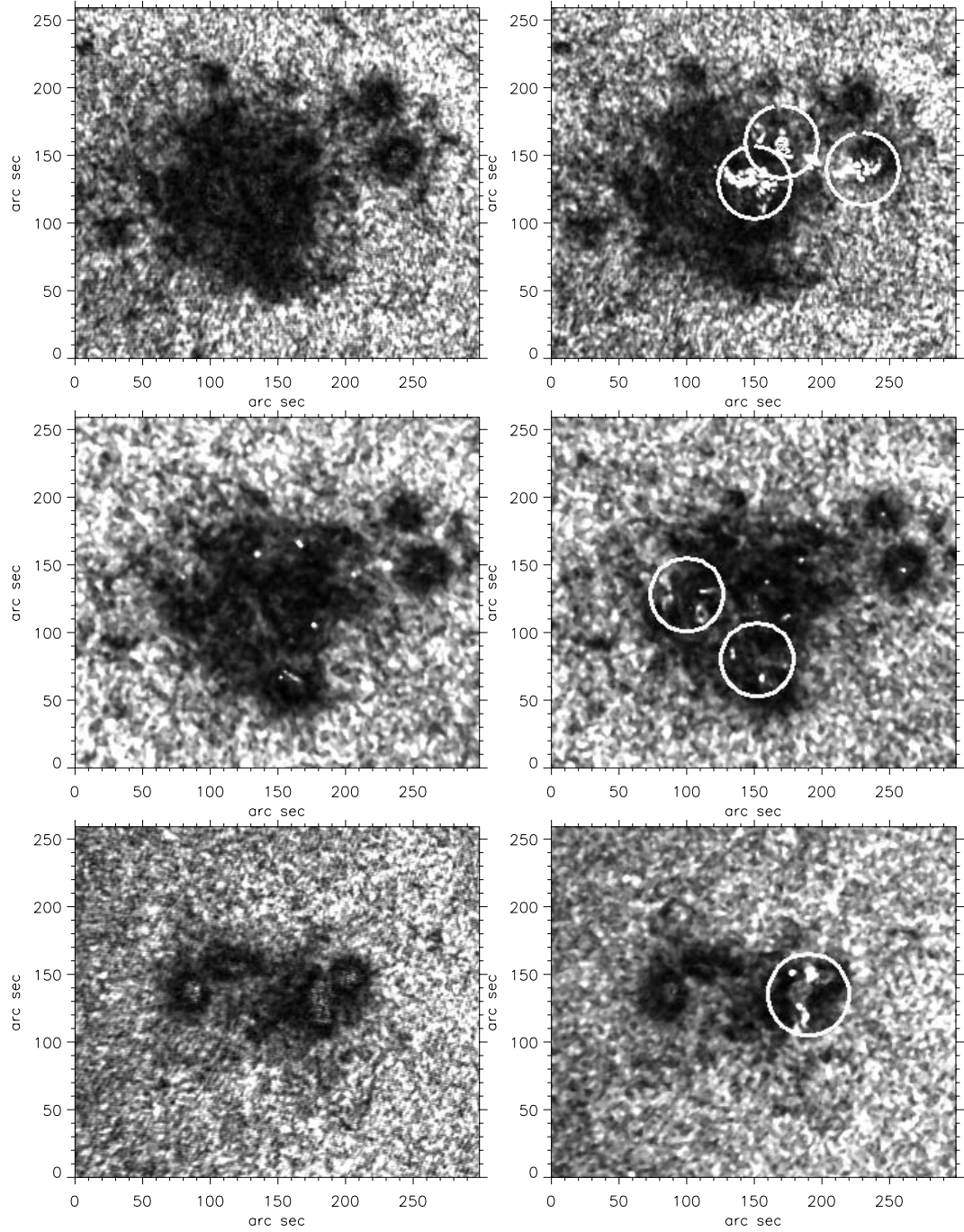


Figure 4.5: Same as Figure 4.4, but for the frequency band 5–6.5 mHz. The power maps on the left hand side have maximum (minimum) values of power  $25.54 \times 10^3$  (245.1),  $114.185 \times 10^3$  (213.846), and  $253.85 \times 10^3$  (242.896)  $\text{m}^2 \text{s}^{-2}$ , while for the right hand side images the values are  $258.07 \times 10^3$  (199.358),  $40.352 \times 10^3$  (275.154) and  $182.748 \times 10^3$  (265.769)  $\text{m}^2 \text{s}^{-2}$ , from top to bottom, respectively. The encircled regions show the location of enhanced power.



quiet Sun (Hindman and Brown, 1998, and references therein). However, the reduction of power in 2–4 mHz band in active regions is accompanied by a slight increase in high frequency power (5–6.5 mHz) in comparison with the quiet Sun spectrum (Venkatakrishnan, Kumar, and Tripathy, 2002, and references therein). In the present study, we analyse the effect of a flare on velocity oscillations in active regions. Therefore, we separate the aforesaid frequency bands for our analysis. The procedure followed for producing a power map is as follows. First, we took a data cube of filtered Doppler images of the entire time series as mentioned in Section 4.2. We have then computed the temporal power spectra for individual pixels without averaging for time duration of two hours before the flare and similarly for two hours during and after the flare. At this stage, the time axis turns out to be the frequency axis. Now, we average the power images in the frequency regimes 2–4 mHz and 5–6.5 mHz, separately for pre-flare and post-flare sequences. The power maps for different days of observation are shown in Figures 4.4 and 4.5 for frequency regimes 2–4 mHz and 5–6.5 mHz, respectively. The left hand side images show the average power map obtained for an hour before the flare while the right hand side images are those obtained for an hour spanning the flare. In these power maps, the encircled regions are locations with enhanced power. The enhancement of power during the flare appears to be more pronounced in 5–6.5 mHz band as compared to 2–4 mHz band. In all these events, it is recognizable that there is little or no enhancement in the 2–4 mHz band. It is clearly seen that most of the locations in the active region appear dark in the power map, indicating absorption of power in the given frequency band. However, in the case of 2003 Oct 29 data, we do observe that some individual pixels in the quiet and active region appear bright before the flare in 5–6.5 mHz band. These could be noise appearing due to the bombardment of high energetic particles to the CCD pixels.

In order to estimate momentum in the enhanced power regions, we have used the integrated power over the pixels with enhanced signals (encircled regions shown in Figure 4.5) in the 5–6.5 mHz band. For a typical density value in the

line forming region  $\approx 10^{-8}$  gm cm $^{-3}$ , we have obtained momentum budget of  $\sim 5.07 \times 10^{23}$ ,  $\sim 4.32 \times 10^{21}$ , and  $\sim 1.22 \times 10^{22}$  dyne s for 2003 October 28 and 29, and 2001 April 6 flare events, respectively, in the 5–6.5 mHz band. This value is close to the momentum budgets for smaller M-class flares as has been deduced by Zarro *et al.* (1988) and Canfield *et al.* (1990).

### 4.3.3 *rms* map of velocity signals

In order to establish the causal correlation between the enhancement of the power obtained in power maps and the flare, we have computed the root mean square velocity map (*rms* map). These images are computed from the subtracted Dopplergrams. We have used the one hour data centered at flare occurrence time. First, the mean velocity image has been obtained and then the *rms* image. In Figure 4.6, the left hand side images show the *rms* map of the velocity signals obtained for an hour before the flare and right hand side images are those for an hour spanning the flare for the events of 2003 October 28 and 29, and 2001 April 6, from top to bottom, respectively. These *rms* maps show that there is enhancement of velocity signals at various locations of the active region during the flare events. This can be readily seen by comparing the *rms* maps obtained during the flare with those before the flare (left hand side images). It should be noted that these enhancements are exactly in the same position as that found in the power images of 5–6.5 mHz band. On 2003 October 28, these velocity enhancements look like two ribbons on either side of a neutral line, as usually seen in H $\alpha$  observations of solar flares. These velocity enhancements are spatially located on one side between 130–160 arc sec in x-direction and between 120–140 arc sec in y-direction. The another enhanced region is located between 150–250 arc sec in the spatial x-direction and 130–160 arc sec in the spatial y-direction. Similarly, on 2003 October 29, the enhancement in the signal can be seen between 50–150 arc sec in the spatial x-direction, diagonal to the map. On 2001 April 6, the enhancement position is at 190 arc sec in the spatial x-direction. The advantage of this *rms* map is that it shows the changes which have occurred in time and also it shows the

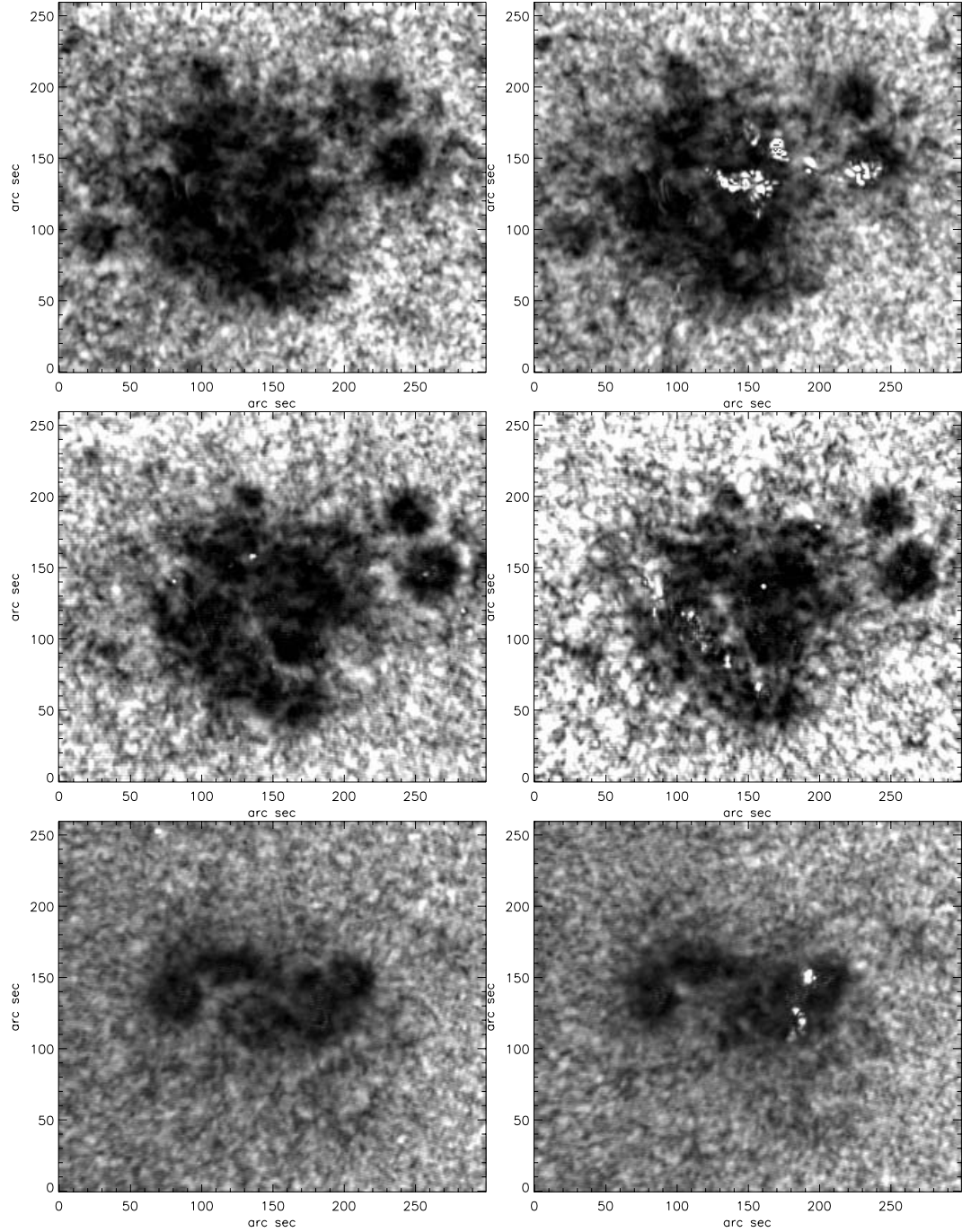


Figure 4.6: Root mean square ( $rms$ ) images computed from the Dopplergrams for 2003 October 28 and 29, and 2001 April 6 events, from top to bottom, respectively. Left hand side images are the  $rms$  maps obtained for an hour before the flare events, while the corresponding right hand side images are obtained for an hour spanning the flare.

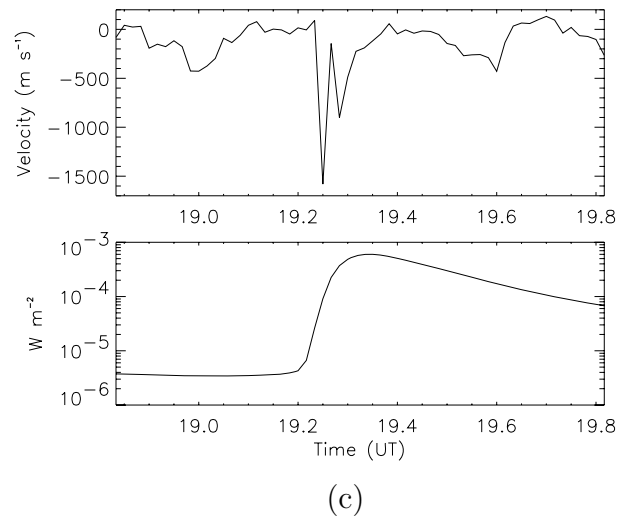
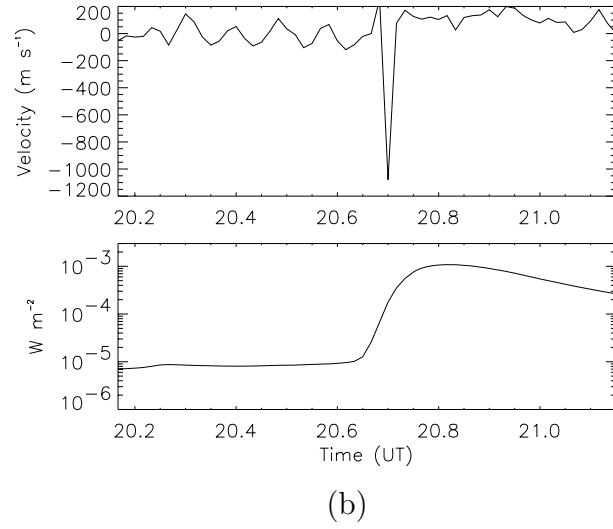
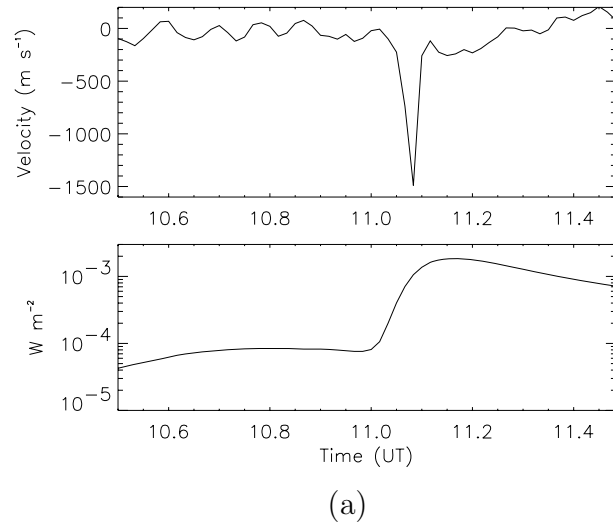


Figure 4.7: (a) The plot showing the velocity signals of a single pixel obtained before, during and after the flare event for the data of 2003 October 28. The bottom plot shows the GOES X-ray flux. (b) Same as (a), but for the event of 2003 October 29. (c) Same as (a), but for the event of 2001 April 06.

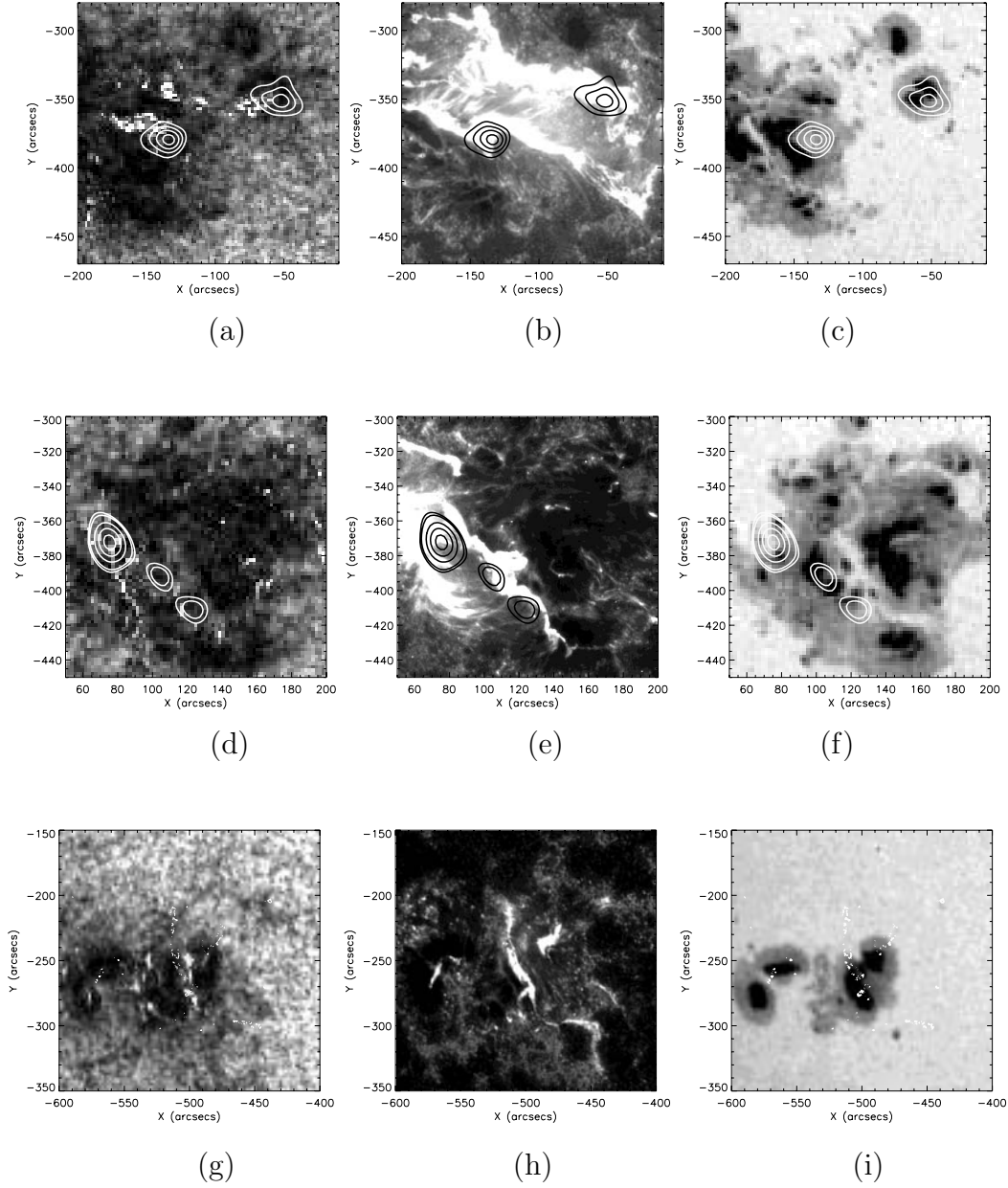


Figure 4.8: (a) The contours of RHESSI hard X-ray flux in the range of 100–300 keV, during the time interval 11:07–11:08 UT overlaid upon the *rms* Doppler image of 2003 October 28 flare. The contour levels are 90%, 70%, 50% and 30% of the maximum count. (b) The same contours overlaid upon the TRACE 1600 Å image observed at 11:28 UT. (c) RHESSI contours overlaid upon the MDI intensity image. (d), (e) and (f) are same as (a), (b) and (c) but for the data of 2003 October 29. The contour levels are 90%, 70%, 30% and 25% of the maximum count between the time interval 20:42–20:43 UT. The TRACE 1600 Å image was observed at 21:08:53 UT. (g) and (i) show the contours of the loop brightening observed in the TRACE 1600 Å flare overlaid upon the *rms* image and MDI intensity image of the 2001 April 6 flare event. (h) The TRACE 1600 Å image obtained at 20:03 UT is shown for comparison.

location of these changes in the active region. The *rms* map represents average power over the all acoustic frequencies present in the data. In the *rms* map, one can also notice that the sunspot region is dark compared to the surrounding region of the spot, which is because of the absorption of acoustic modes in the sunspots as compared to the quiet region. However, the locations of acoustic emissions in the active region are bright. The coincidence of the positions of the velocity enhancements in both the *rms* maps and power maps suggest that these enhancement in velocity signals are due to flare. Further, we examine the amplitude of velocity signals during the flare in the aforesaid bright pixels for all the flare events. In Figure 4.7, we show some examples for those pixels which appear bright in the *rms* map. These velocity signals are obtained by subtracting the mean velocity signal from the observed total Doppler signal. The velocity signals show sudden jump above background velocity, close to the peak time of GOES X-ray flux. These timings are different for different pixels, which is because as the flare kernel moves onward it may excite velocity signals at different locations. In Figure 4.7, the excited velocity signal comes down close to the background level after a sudden jump. However, for the events of October 28 and 29, 2003, the background signal decreases or increases by about 200 m/s after the jump in the excited velocity signal. This kind of little enhancement in the background signal after the flare can be seen in most of the pixels which are in and around the bright regions of the *rms* map.

In order to examine the positions of the enhanced velocity signals with respect to the hard X-ray positions, we used the RHESSI hard X-ray images in the range 100–300 keV. We then overlaid the contours of these hard X-ray signals on the *rms* images. Unlike the *rms* images obtained above, here we used the full-disk, derotated and subtracted Dopplergrams for *rms* image extraction. This is for easy alignment of the *rms* images with the RHESSI and TRACE images. We also overlaid the contours of hard X-ray on the TRACE 1600 Å images to examine the positions of the loops and the hard X-ray flux positions. Figures 4.8(a), (b) and (c) show the contours of RHESSI hard X-ray flux on the *rms* velocity image, the TRACE 1600 Å image and MDI intensity image,

respectively, for the 2003 October 28 flare event. Figures 4.8(d), (e) and (f) show the same for the 2003 October 29 flare event. In the case of 2001 April 6 event, the RHESSI images are not available and hence we overlaid the contours of the loops observed in TRACE 1600 Å on the *rms* image and MDI intensity image, which may be the position of the hard X-ray flux. Figures 4.8(a) and (d) show that brightening in the *rms* image occurs near maxima of the hard X-ray flux. Even in the case of the flare on 2001 April 6, the brightening in the *rms* image coincides with the loop brightening of TRACE 1600 Å image. On 2003 October 28, the enhanced velocity positions are not completely correlated with the hard X-ray positions. The reason behind the lack of good correlation could be explained as follows. The RHESSI started observing the flare (after its night) at 11:07 UT, however the flare had started much before this time (09:51 UT). Thus, RHESSI observations could have missed the positions of hard X-ray source regions during the peak time in the given energy band. The hard X-ray source region moves as the reconnection site moves (Krucker, Hurford, and Lin, 2003; Bogachev, Somov, Kosugi, and Sakao, 2005). Since the flare started much before the RHESSI observations whereas MDI covered the whole event at a cadence of 1 min, the different excited positions in velocity are observable in MDI data, however RHESSI might have missed the corresponding positions in the hard X-ray. In the next Chapter, we use ARIES H $\alpha$  images as a proxy for hard X-ray and obtain extremely interesting results.

## 4.4 Summary and Discussions

The study of velocity enhancements during X-class flares in the active regions NOAA 10486 and 9415 on 2003 October 28 and 29, and 2001 April 6, respectively, showed the following results:

- (1) Transient change in velocity signals have been observed, which appear to precede the peak time of the GOES soft X-ray flux, but occur after the onset of the SXR flare.
- (2) These enhanced velocity signals are close to the vicinity of hard X-ray

source regions.

(3) The enhancement in the velocity signal is found in the frequency regime 5–6.5 mHz, while little or no enhancement is observed in 2–4 mHz band.

The hard X-ray emissions have their origin from the non-thermal bremsstrahlung of accelerated electrons in solar flares (Brown, 1971; Hudson, 1972). The large flux of non-thermal energetic electrons can heat the chromospheric plasma (Fisher, Canfield, and McClymont, 1985), and this sudden heating causes thermal instability which expands the chromospheric plasma to the temperature of the corona. This will happen when the hydrodynamic expansion time scale is larger than the heating time scale (Fisher, Canfield, and McClymont, 1985). Further, the increase in plasma pressure will cause explosive evaporation of the chromospheric plasma into the corona and then downward settlement as chromospheric condensation (Fisher, 1989), as has been evidenced in red wing asymmetry of  $H\alpha$  line profiles. The downward propagating plasma and shock waves ahead of plasma were assumed to be the agents delivering momentum to the photosphere which can result in observed excited acoustic signature. The excited velocity signals appear as red-shifted in those locations for short duration.

The global  $p$ -modes that are observed to be always present on the Sun are excited by turbulence in the convection zone (Goldreich and Kumar, 1990, and references therein, Stein and Leibacher, 1974) and are modified in active regions due to absorption of acoustic waves by magnetically inhomogeneous media (Braun, Duvall and LaBonte, 1988). In addition to this continuous source of excitations, transient phenomena like flares can contribute additional energy to these modes. Even if a small fraction of the energy released by flare is transferred to oscillations in active region, it can increase the amplitude of oscillation significantly. However, the photosphere and magnetic field in active region provides a boundary condition for the  $p$ -modes and any source of additional energy from the external agent may affect these oscillations for short spans, as these can not be sustained by the cavity. This can lead to the



enhanced velocity oscillations during flare events. Infact, the enhancement of power in 3 minute band is a clear indication of the “wake” (Rae and Roberts, 1982) of the chromospheric response at the acoustic cut-off frequency (Lamb, 1932) to a pressure impulse .

On the other hand, there are some evidences about the Ni I 6768 Å line profile turning into emission during strong X-class flares (Qiu and Gary, 2003). The non-thermal electrons can produce heating at the foot-points of the magnetic field lines. Using non-LTE calculations, Ding, Qiu and Wang (2002) found that the Ni I 6768 Å line may appear in emission in the presence of strong electron beam in a cool atmosphere like sunspots. They also found that even if the atmosphere gets hot in the absence of energetic particles, the line profile may not turn into emission. If the line profile turns into emission during the flare, then there is a possibility of sudden change in the velocity signal. This change in velocity signal persists till its source dies down. To examine this, one needs to have the spectral line information of line from which the Dopplergrams have been obtained. The future space based missions like Solar-B may help in this context. In any case, one need to study more about the velocity oscillations in active regions during the flares.

# Chapter 5

## Signature of photospheric “Doppler ribbons” beneath $H\alpha$ flare ribbons observed during an intense 4B/X17.2 solar flare

### 5.1 Introduction

$H\alpha$  flare ribbons are the sites of the impact of electron beams on chromospheric material. The resulting chromospheric evaporation is manifested as a brightening in  $H\alpha$ . This brightening occurs because the ionization of the H-atom by the electron beam impact is followed by recombination to various energy levels of the hydrogen atom, including the 3<sup>rd</sup> level. The transition from level 3 to level 2 results in  $H\alpha$  emission. The bremsstrahlung radiation generated by deceleration of the electrons while striking the target (chromosphere) produces hard X-ray emission (Brown, 1971), while the gyrosynchrotron emission due to motion of electrons along magnetic fields produces microwave radiation (Hudson, 1972). All these classic signatures of the electron beam impact were seen at enhanced levels in the “super active region” NOAA active region 10486 which appeared on the solar disk during October 2003 and produced a lot of

space weather related activity (Gopalswamy, 2005). In addition, some interesting photospheric disturbances were also reported in this active region in the form of acoustic “ripples” (Kosovichev, 2006) as well as post impact enhancement of amplitude of acoustic  $p$ -modes (Ambastha *et al.*, 2006). Kosovichev and Zharkova (1998) reported the first detection of “solar quakes” inside the Sun observed during X2.6 flare of 9 July 1996 using the Dopplergrams obtained from Michelson Doppler Imager (MDI: Scherrer *et al.*, 1995) onboard the Solar and Heliospheric Observatory (SOHO: Domingo, Fleck, and Poland, 1995). In this Chapter, an another interesting photospheric phenomenon is reported, viz., “Doppler ribbons” or localized velocity enhancements, which were seen to accompany the  $H\alpha$  ribbons during the 4B/X17.2 class flare of 28 October 2003 (peak at  $\sim 11:04$  UT) in SOHO/MDI Dopplergrams.

## 5.2 The observational data

We chose the data of active region NOAA 10486 obtained on 28 October 2003. The active region NOAA 10486 was one of the largest groups of sunspots observed in the declining phase of solar cycle 23. It appeared on the east limb of the Sun on 23 October 2003 in the southern hemisphere. This complex active region belonged to  $\beta\gamma\delta$  class and produced several X-class and M-class flares during its passage on the solar disk. On 28 October 2003, a major flare of 4B/X17.2 class occurred in this active region when it was located near the central meridian (S17E13). This was one of the largest flares of solar cycle 23, which occurred near the Sun’s center and produced extremely energetic emission almost at all wavelengths from  $\gamma$ -ray to radio-waves. The flare was associated with a bright/fast-halo Earth directed CME, strong type II, type III and type IV radio bursts, and an intense radio burst. This flare was also observed with space based solar observatories viz., SOHO, TRACE (Handy *et al.*, 1999) and several other ground based observatories viz., Udaipur Solar Observatory (USO) and Aryabhata Research Institute of Observational Sciences (ARIES) in India in  $H\alpha$  wavelength (Ambastha, 2006; Uddin, Chandra,

and Ali, 2006).

We have used data from SOHO/MDI and ARIES for the analysis of this event. The  $H\alpha$  data from ARIES remained nearly free from saturation effects due to large dynamic range of CCD camera used in the observations and was therefore useful on photometry of flare kernels. The details of the data are given as follows:

### 5.2.1 SOHO/MDI data

We have used full disk MDI Dopplergrams (spatial resolution of  $\sim 1.9$  arcsec per pixel) between 11:00–11:15 UT observed in Ni I 6768 Å line with a cadence of 60 s in order to examine the enhanced velocity signals in this active region during the aforesaid “super flare” (peak  $\sim 11:04$  UT) on 28 October 2003. The active region was tracked using heliographic co-ordinates in the full disk Dopplergrams, which were interpolated to a  $1''$  pixel size. We have also used the co-temporal white light images and magnetograms from MDI for our study.

### 5.2.2 ARIES data

Co-temporal  $H\alpha$  images from ARIES have been used as a proxy for hard X-ray data, since RHESSI (Lin *et al.*, 2002) did not observe during the peak time of the flare ( $\sim 11:04$  UT). The ARIES observations were done using 15 cm, f/15 Coudé Solar Tower Telescope equipped with Bernard Halle  $H\alpha$  filter and Wright Instrument CCD camera system (16 bit,  $385 \times 576$  pixel, pixel size = 22 micron square). With the help of barlow lens the image is magnified twice, so a resolution of  $\sim 1$  arcsec per pixel is achieved. The observed filtergrams were corrected using dark current and flat field images taken during the observations. All images were re-registered.

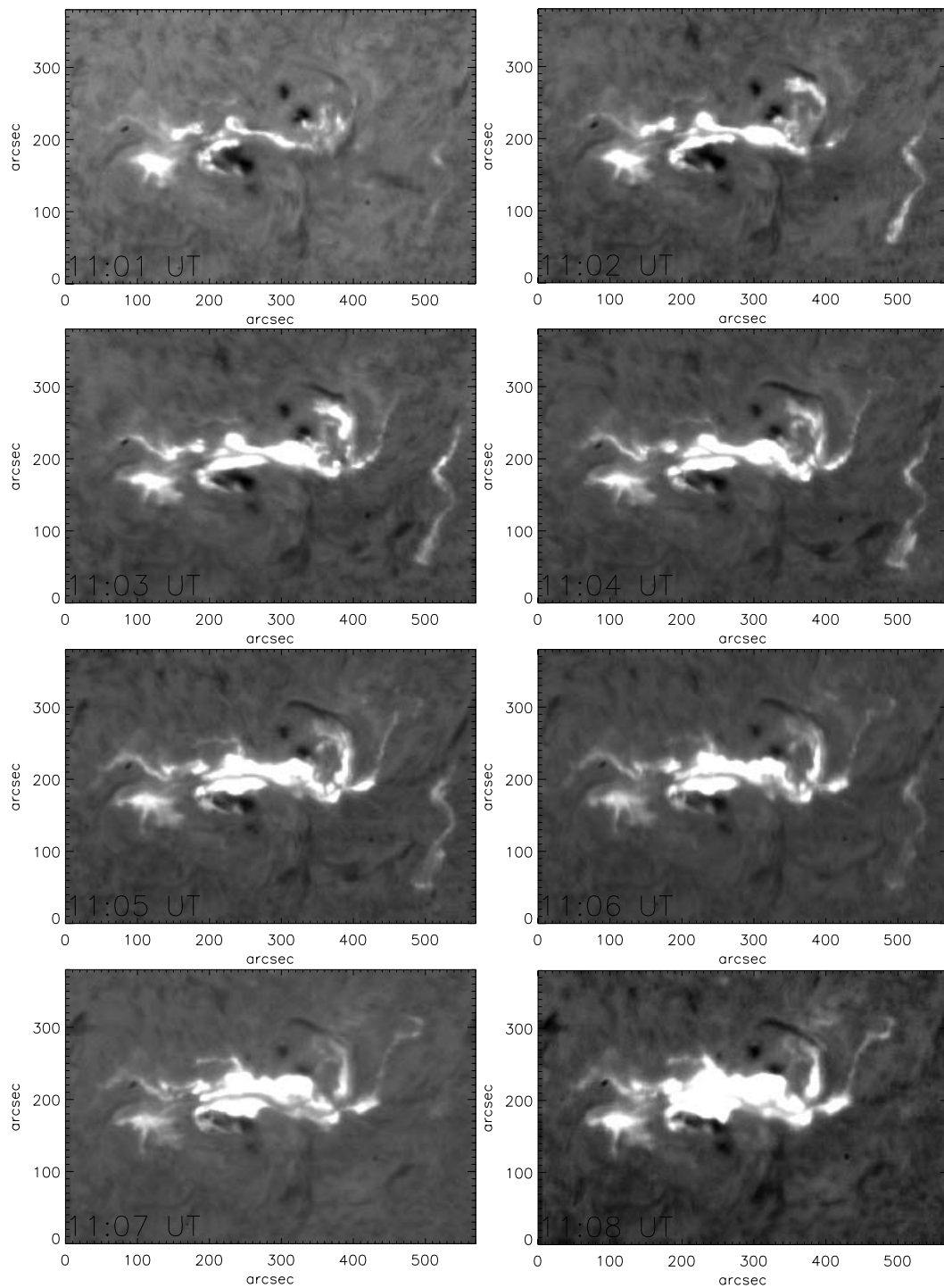


Figure 5.1: Sequence of H $\alpha$  filtergrams observed at ARIES during 11:01–11:08 UT showing the temporal evolution of the 4B flare in the active region NOAA 10486 on 28 October 2003.

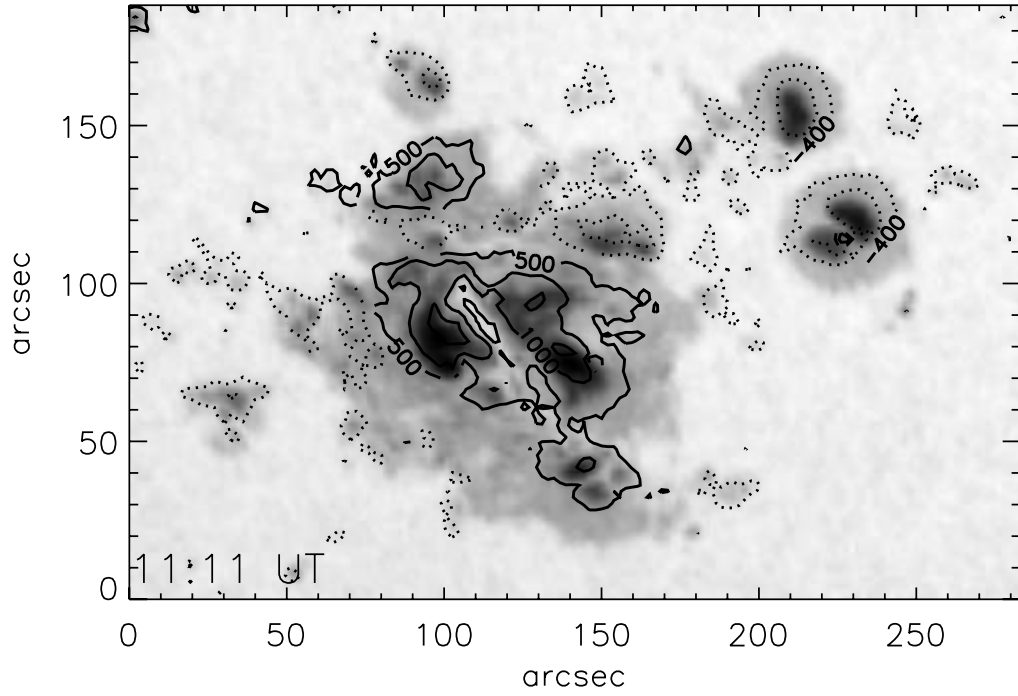


Figure 5.2: MDI white light image of active region NOAA 10486 at 11:11 UT on 28 October 2003 overlaid with the contours of magnetic fields from the simultaneously observed magnetograms. The contours drawn with solid lines are for North polarity while that drawn with dotted lines depict South polarity.

## 5.3 Analysis and Results

### 5.3.1 $H\alpha$ observations

The temporal evolution of the flare in  $H\alpha$  between 11:01–11:08 UT is shown in Figure 5.1. The sequence of  $H\alpha$  images shows large scale mass motions, darkening of filaments and brightening at many places in the active region before the flare onset. The first image taken well before flare at 01:28 UT showed three highly twisted long sigmoid filaments, which started eruption before the onset (11:00 UT) of 4B/X17.2 class flare. The eruption of these filaments continued during the flare. The flare shows multi-ribbon structure in  $H\alpha$ . It consists of two main parallel ribbons along the sigmoid filament in opposite magnetic polarity regions. These parallel  $H\alpha$  ribbons show the separation as shown by a typical two ribbon flare, however the ribbon separation speed is relatively very high  $\sim 70$  km/s in this case.

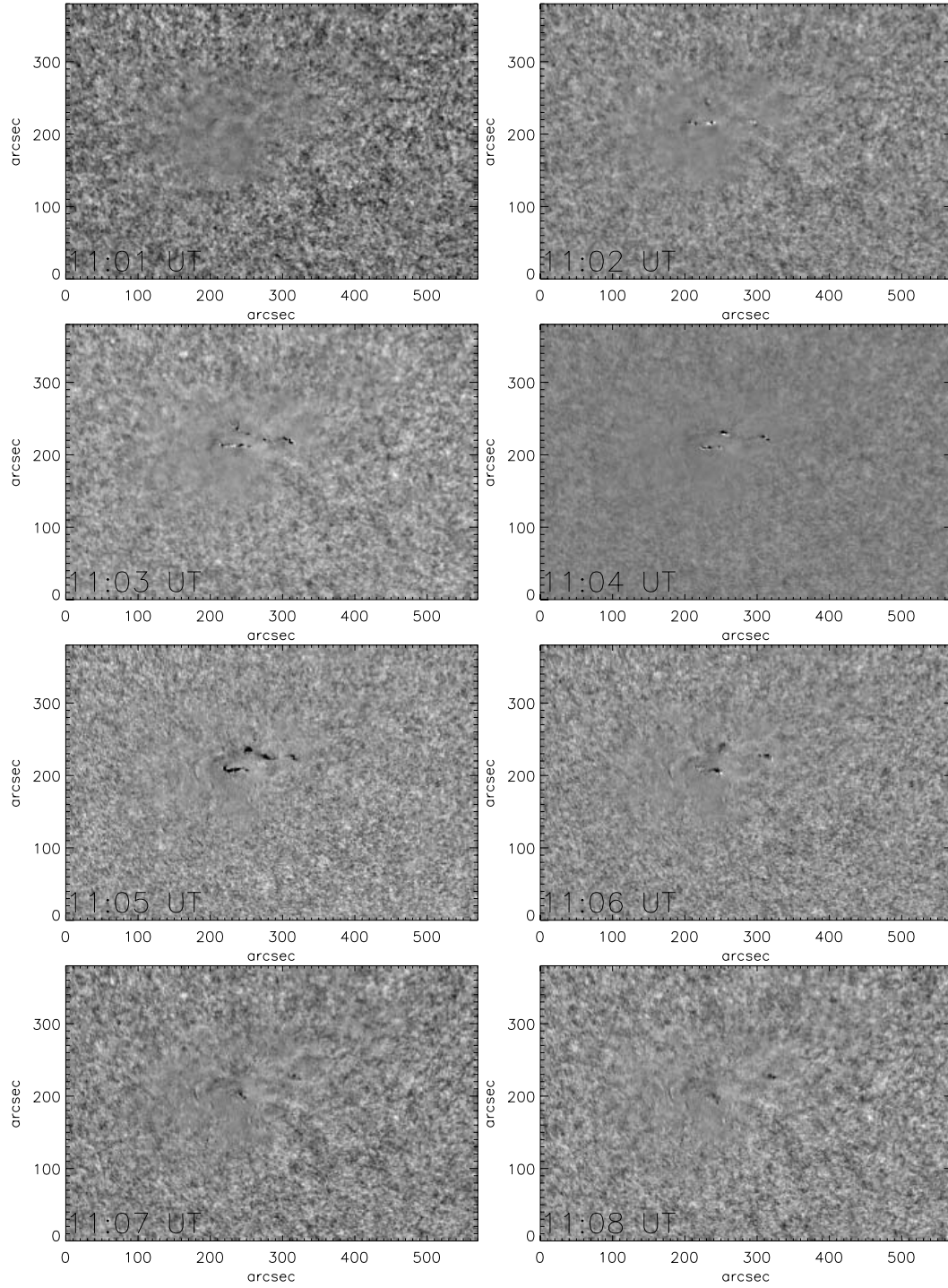


Figure 5.3: Sequence of MDI Dopplergrams observed during 11:01–11:08 UT. The patchy region in the images depicts the location of the active region with suppressed velocity signals. However, the photospheric velocity enhancements in the active region during this super flare appear in the form of Doppler ribbons analogous to the  $H\alpha$  flare ribbons as seen in the patchy region.

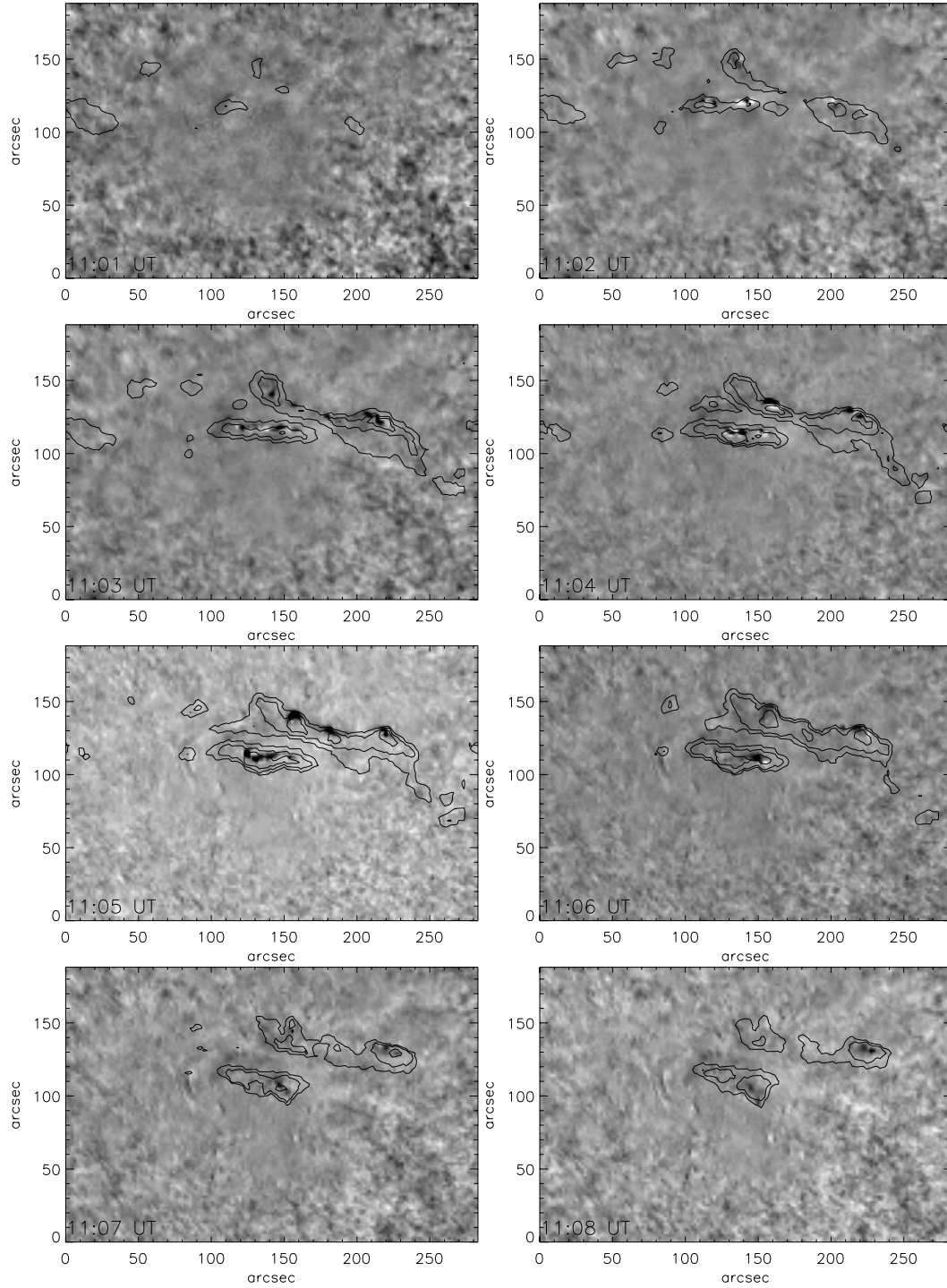


Figure 5.4: Sequence of MDI Dopplergrams overlaid with the  $H\alpha$  flare intensity contours observed during 11:01–11:08 UT. The contours are drawn at levels of 40%, 60%, and 80% of the peak value in  $H\alpha$  intensity. The photospheric velocity enhancements in the active region during the flare appear in form of Doppler ribbons and exactly match the location of  $H\alpha$  flare ribbons in space, and approximately in time.



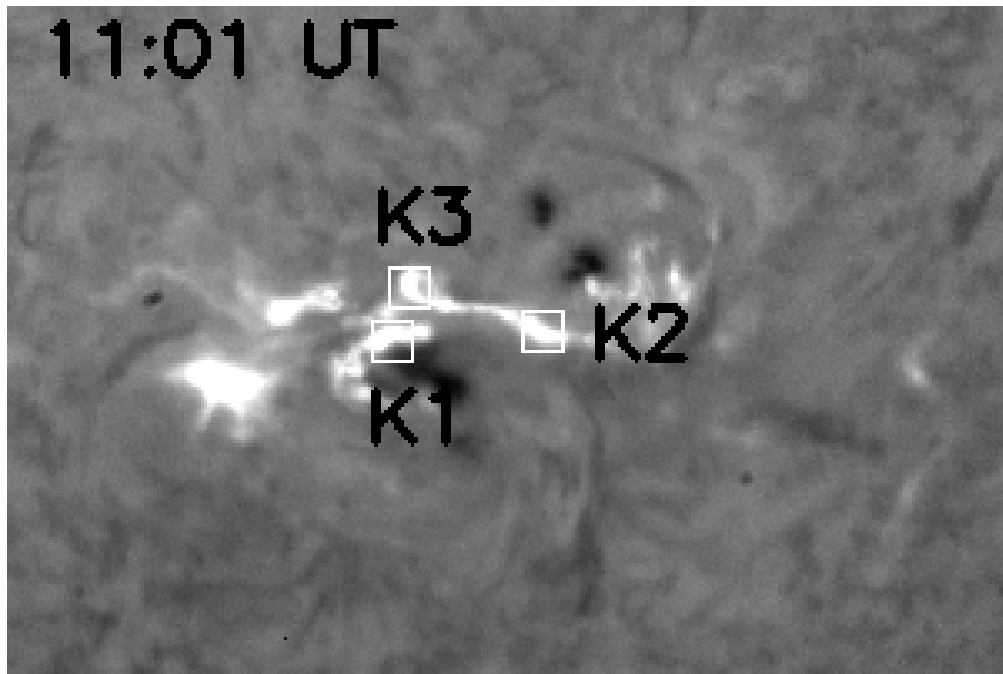


Figure 5.5:  $H\alpha$  filtergram obtained at ARIES at 11:01 UT on 28 October 2003 showing the locations of the flare kernels (K1, K2, & K3) in the active region NOAA 10486.

### 5.3.2 SOHO/MDI observations

The super active region NOAA 10486 was having a complex morphology. In Figure 5.2, we show the MDI white light image of this active region overlaid with the contours of the magnetic fields from simultaneous MDI magnetogram. This picture clearly reveals the complex magnetic structure of the active region. A close inspection of the Dopplergrams from MDI during the impulsive phase of the flare (11:01–11:08 UT) revealed “Doppler ribbons” analogous to the  $H\alpha$  flare ribbons. The morphology of these Doppler ribbons is clearly visible when the sequence of Dopplergrams between 11:01–11:08 UT are subtracted from the Doppler image taken at 11:00 UT. In Figure 5.3, we show the sequence of aforesaid subtracted Dopplergrams which clearly depict the Doppler ribbons being excited during the impulsive phase of this super flare. In fact, the velocity flows are known to be suppressed in the active regions, and hence we observe a patchy region with diminished velocity signals corresponding to the location of the active region (Figure 5.3). On the other hand, we observe “ribbons” in the active region during the flare, which appear similar to the  $H\alpha$  flare ribbons

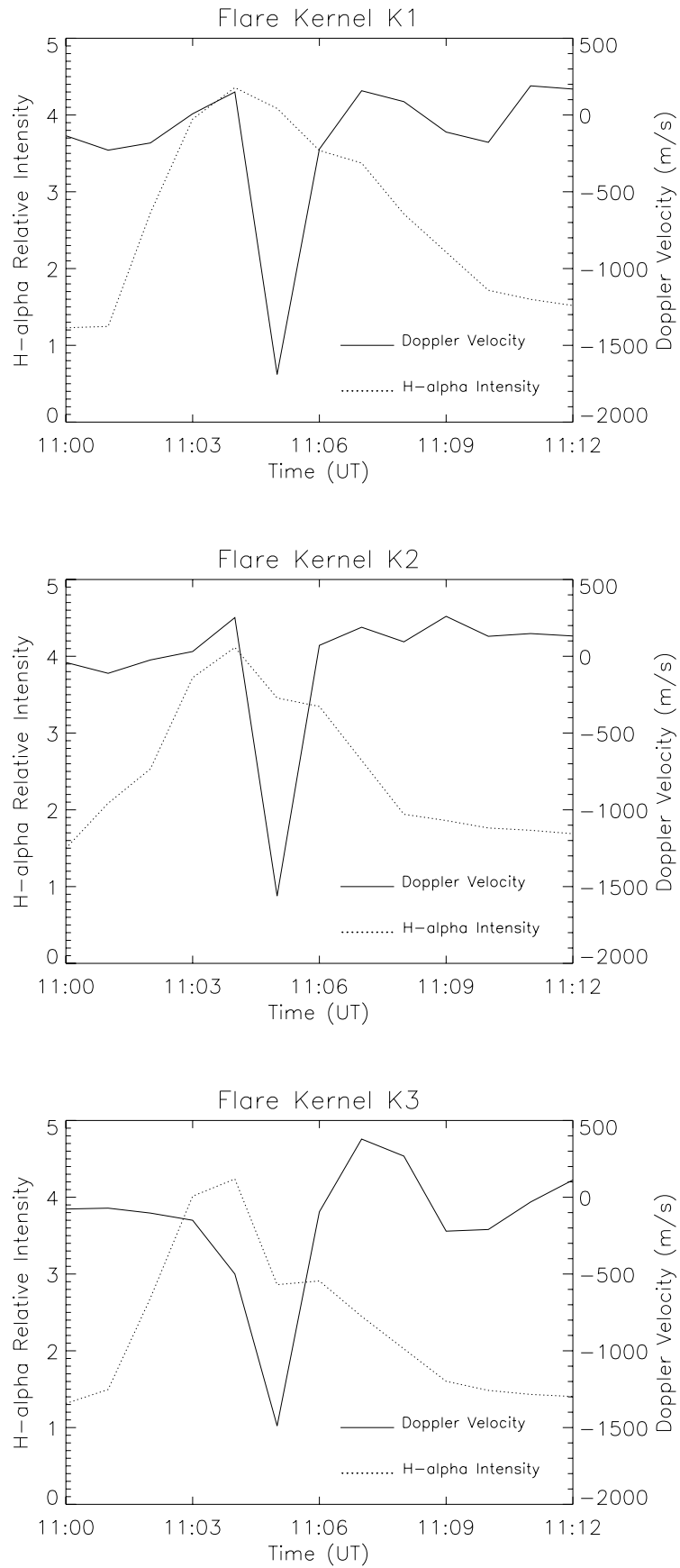


Figure 5.6: Plots of Doppler velocity and H $\alpha$  relative intensity in the localized positions of the flare kernels depicted in Figure 5.5. It is seen that the peak of velocity enhancement ( $\sim 11:05$  UT) follows the peak time in H $\alpha$  intensity ( $\sim 11:04$  UT).

depicted in Figure 5.1.

### 5.3.3 Correlation between SOHO/MDI observations and $H\alpha$ observations

The rarely visible “Doppler ribbons” in this event of “super flare” are correlated with the  $H\alpha$  ribbons observed during this flare. For this purpose, we have co-aligned the MDI Doppler images with the  $H\alpha$  images in space and time between 11:01 UT and 11:12 UT. Figure 5.4 shows the contours of  $H\alpha$  flare intensity drawn over the difference Doppler images (excess velocity over the Dopplergram obtained at 11:00 UT, c.f., Figure 5.3) for the period 11:01–11:08 UT. It is clearly seen that the enhancements of velocity signals appearing in the form of “ribbons” exactly match the location of  $H\alpha$  flare ribbons in space, and approximately in time. This is why we have named these velocity structures as “Doppler ribbons”, which is in fact a rare phenomenon observed during this major flare event of solar cycle 23.

Further, we have identified three flare kernels (K1, K2, and K3) in  $H\alpha$  which are depicted in Figure 5.5. A raster of  $3\times 3$  pixels is selected in the center of each of the aforesaid kernels to study the correlation between the variations of  $H\alpha$  flare intensity and velocity flows in these locations. The temporal evolution of Doppler velocity and  $H\alpha$  flare intensity during 11:01–11:12 UT in these localized positions have been plotted in Figure 5.6, which shows a 1 minute delay of the peak in velocity flows ( $\sim 11:05$  UT) relative to the peak time of  $H\alpha$  flare intensity ( $\sim 11:04$  UT) in all the three flare kernels.

## 5.4 Discussions and Conclusions

There are two plausible physical interpretations for the Doppler enhancement accompanying the  $H\alpha$  ribbons. The “Doppler signal” could have been produced by a distortion of the line profile that is expected to accompany major flares (Qiu, and Gary, 2003). In this case, the source function for line formation in the atmosphere is disturbed by the transient alterations of relative popula-

tions of the atoms which interact with the electrons that are able to penetrate through the chromosphere and reach the photosphere. In the absence of line profile information, we cannot make a definitive statement about this. On the other hand, we could make reasonable inferences on an alternative scenario based on other circumstantial evidence. For example, the detection of acoustic ripples (Kosovichev, 2006) and the post flare enhancement in  $p$ -mode amplitudes (Ambastha *et al.*, 2006) must be related to a localized pressure enhancement followed by atmospheric oscillations in the wake of the pressure pulse. Likewise, Kumar and Ravindra (2006) report on transient enhancements in the amplitude of 3 minute oscillations in photosphere at locations of enhanced velocity signals in active region NOAA 10486, as well as in other active regions. Kumar and Ravindra (2006) invoke the physical scenario involving pressure pulse generated by downward propagating shock wave from the site of chromospheric evaporation that was originally proposed by Fisher, Canfield, and McClymont (1985) and later discussed in detail by Fisher (1989). Of course, one cannot rule out the possibility of both effects acting together. Line profiles recorded during intense flares will clearly demarcate the contribution from line profile distortion as opposed to that caused by pressure enhancement. Once this contribution is eliminated, then the remaining pressure enhancement can be used to model the downward propagating shock wave from the site of chromospheric evaporation. Precise timing information on the commencement of  $H\alpha$  brightening and start of the photospheric Doppler enhancement can also be used to measure the speed of the downward propagating shock wave. Assuming that the shock travels with the speed of sound ( $\sim 7$  km/s), the observed lag of  $\sim 60$  s implies a height of  $\sim 400$  km of the evaporation site above the photosphere, which coincides with the base of the chromosphere. Likewise, the excitation of 3 minute oscillations by the flare, as seen by Kumar and Ravindra (2006) is consistent with the response of the atmosphere to a pressure impulse in the form of a “wake” at the acoustic cut-off frequency (Lamb, 1932; Rae, and Roberts, 1982). The combination of all the evidences is therefore in favour of the “Doppler ribbon” being a manifestation of a pressure impulse striking

the photosphere, following explosive evaporation in the chromosphere. The fact that these Doppler ribbons are not observed commonly also indicates that the electron flux from the flare must be extraordinarily large to be able to produce a discernible effect in the photospheric Doppler signal.

# Chapter 6

## Summary, Conclusions and Future plans

The prime idea of this research work is to identify and understand the morphology, dynamics and influence of the localized inhomogeneities in the solar atmosphere at different length-scales and at different heights. The large-scale inhomogeneities appear in the form of magnetic features, like, sunspots, filaments, supergranulations, faculae and plages etc., whereas the small-scale magnetic features include the pores, fibrils, spicules, granulations, network and intranetwork regions. These inhomogeneities evolve with the solar cycle and give rise to interesting events. Some of these events are very rare, such as detection of photospheric “Doppler ribbons” and “solar quakes” during intense solar flares as has been widely discussed in this thesis. The study of such events can enhance our knowledge about the basic astrophysical processes taking place in the Sun.

The aforesaid investigations could be done by resolving the fine structures of these inhomogeneities in multi-wavelengths at different scale heights of the solar atmosphere from photosphere to corona through the chromosphere and transition region. These observations could be accomplished by both, space based and ground based observatories. Space based observations are free from atmospheric effects; however they are short lived and expensive. On the other hand, ground based observations are stable, however they are affected by

Earth’s atmospheric turbulence. The atmospheric turbulence or “seeing” could be well estimated using established techniques. In this thesis, we have extensively used solar  $H\alpha$  images to quantify “seeing” at the lake site of USO and established the efficacy of using small imaging telescopes even for initial site surveys for large ground based observational facilities. The estimates of “seeing” obtained in this analysis helped in determining the aperture of a Multi-Application Solar Telescope (MAST) proposed for USO. It also helped in the design and development of an Adaptive optics (AO) system at USO, which will be basically used for improving the resolution of ground based imaging system by correcting the perturbed wave-front passing through the Earth’s turbulent atmosphere.

In this Chapter, we summarize Chapter-wise, the results of the thesis and then present the overall conclusions. Further, we briefly describe our future plans. In the introduction, we briefly described the importance of the study of evolution of inhomogeneities in the solar atmosphere with the solar cycle. We then briefly reviewed the various types of evolution of inhomogeneities in the solar atmosphere with an emphasis on the rarely observed phenomena and their impact on latest developments in the area of solar physics.

## 6.1 Present Work

### 6.1.1 Site characterization using solar $H\alpha$ images

The observations taken with ground based telescopes is limited by the perturbations introduced by the atmospheric turbulence. Generally, atmospheric turbulence is characterized by a spatial scale ‘ $r_0$ ’ known as Fried’s parameter (Fried, 1965, 1966a, and 1966b). It is interpreted as the size over which the *rms* variance of the phase fluctuations is one  $\text{rad}^2$ , that corresponds to a Strehl ratio of 0.33 (Rodier, 1981). Strehl ratio is defined as the ratio of the observed peak intensity at the detection plane of a telescope or other imaging system from a point source compared to the theoretical maximum peak intensity of a perfect imaging system working at the diffraction limit. In a long exposure

image, the transfer function of an image is the product of telescope transfer function and atmospheric transfer function. Atmospheric transfer function is represented as  $\exp(-3.44(\lambda f/r_0)^{5/3})$ , where  $f$  is the spatial frequency. By knowing the value of  $r_0$ , we can theoretically obtain the transfer function of the atmosphere. Deconvolution of the long exposure image using this theoretical transfer function can improve the images to the extent permitted by the noise. Speckle interferometry is another important image restoration technique used in ground based imaging systems for high resolution observations. It uses theoretical models for estimation of the speckle transfer functions. These models need the knowledge of seeing parameter of the particular site. Further, the knowledge of Fried's parameter for a given site helps not only in reconstruction of high resolution images, it also helps in designing and building an Adaptive optics (AO) system.

The Chapter II is concerned with the measurement of atmospheric “seeing” in terms of the ‘Fried’s parameter’. This parameter gives the quantitative measure of astronomical seeing of the given site and hence severely influences the quality of the recorded image in ground based observations, the larger its value, the better is the image quality. For this purpose, short exposure (3 ms) high resolution  $H\alpha$  (6563 Å) images of the Sun taken in burst mode with the 15 cm refractor spar telescope located at the lake site of Udaipur Solar Observatory (USO) have been extensively used to quantify the seeing conditions prevailing at the lake site during the different months of the year. Spectral ratio technique (von der Lühe, 1984) has been used to estimate the Fried’s parameter ( $r_0$ ) at this site. This study has been carried out daily on hourly basis during 4:30–10:30 UT over the months January–June of the years 2005 and 2006 in order to understand the diurnal and seasonal variations in  $r_0$  at this site. It is noteworthy to mention that the lake was dry during the observing period in 2005, while it overflowed during our observations in 2006 due to good monsoon rains. The seeing in the presence of water shows improvement in  $r_0$  by about 1.0 cm with respect to previous year’s dry condition and mean  $r_0$  varies between 4.0–4.5 cm as evident from the data obtained between January–June,



2006. Thus, the episodic conditions of the lake provided an unique opportunity to study the atmospheric “seeing” in two different conditions. The estimates of  $r_0$  obtained in our analysis helped in determining the optimum size of the Multi-Application Solar Telescope (MAST) proposed for USO. It also helped in the design and development of a proto-type Adaptive optics (AO) system at USO.

There is a more practical lesson that we learn from our study. Hitherto, most site surveys (e.g., Hill *et al.* (2006)) used scintillometry for monitoring the seeing since the scintillometers are eminently portable. However, our study establishes the efficacy of using small imaging telescopes even for the initial site surveys. This is because modern  $H\alpha$  filters e.g., Coronado solar filters (<http://www.coronadofilters.com>) are relatively inexpensive and can be easily attached to the entrance aperture of compact telescopes designed for solar observations, which are available with such manufacturers. Further, CCD prices are also declining. Hence, small telescopes, equipped with  $< 1 \text{ \AA}$  entrance filters centered at  $H\alpha$  and fast CCD cameras could be readily deployed for measuring  $r_0$  in an unambiguous manner. For exceptionally good sites where  $r_0 > D$ , the telescope aperture, we can register large FOVs and then use angle of arrival fluctuations within isoplanatic patches to estimate  $r_0$ . Another lesson learnt from our study is that our dome contributes nearly 2 arc-sec of seeing. This estimate arises from the square root of the difference of the squares of best and worst seeing for both the years. Thus, we can expect the mean seeing to be about 2 arc-sec at the lake site of USO by observing without the dome. This has been planned for MAST. The local government has also planned to maintain the water level in the lake through ambitious water supply projects for Udaipur.

### 6.1.2 An Image Stabilization System for solar observations at USO

The turbulence in the Earth's atmosphere causes rapid random motion of the images at the focus of ground based telescopes. This leads to a degraded image in a typical long exposure image lasting a few seconds. Techniques like speckle imaging perform post-processing of noisy short exposure images and have proven capability of achieving diffraction limited imaging. Adaptive optics attempts to correct for the degradation caused by the atmosphere in real time using opto-mechanical elements. As a result, in the case of point sources, it is possible to focus the light over a small area in the focal plane of the telescope for a long duration and thus ability to sense faint stars over the sky background is enhanced. In addition to the high spatial resolution, the possibility to stabilize images at the entrance slit of spectrographs renders high signal to noise ratio and spectral resolution. Even a rudimentary adaptive optics system correcting for the image motion alone is capable of achieving diffraction limit under good seeing conditions.

In an image stabilization system (also known as tip-tilt or correlation tracking system), a small portion (typically  $10 \times 10$  arc-sec<sup>2</sup>) of a short exposure (typically  $< 10$  ms) image is cross-correlated with a previously recorded reference image. Subsequent images are correlated with the same reference image. This reference image needs to be updated within the time scale of evolution of the solar feature used as a reference. However atmospheric conditions change more rapidly than the time taken for the feature to evolve hence we change the reference image every 10 seconds or so to make best use of the atmospheric conditions. The cross-correlation extracts the shift of the instantaneous image with respect to the reference image in two orthogonal directions. These shifts are used to calculate and feed appropriate voltages to the tip-tilt mirror so that its surface closely approximates to the instantaneous global tilt of the wave-front. As the global tilt is removed from the wave-front, after being reflected off the mirror, the random image motion is arrested. This results in a stable

output in the science camera and thus allows for long exposures.

Several solar adaptive optics systems are either developed or being developed at various observatories around the world (Rimmele, 2000; Scharmer *et al.*, 2003; von der L  he *et al.*, 2003; Keller, Plymate, and Ammons, 2003). Unlike stellar adaptive optics systems, most of the solar adaptive optics systems operate in the visible region of the electromagnetic spectrum. The scintillation is normally ignored, while the global tilts of the distorted wave-front are corrected with the help of tip-tilt mirror system and the local tilts are corrected using deformable mirrors which are available in the form of either thin membrane mirrors or solid bi-morph mirrors. A special aspect of solar adaptive optics systems is that the region of scientific investigation itself -usually small scale features (pores, granulations, and small sunspots etc.) riding on an extended background (quiet photosphere/ continuum), is used as the reference in a much wider spectral bandwidth centered away from the spectral region of interest. In spite of the hurdles caused by the day time seeing conditions which are arguably worse than their night time counterparts, images recorded with robust solar adaptive optics systems coupled with post processing techniques reveal finest details ever seen on the solar surface at visible wavelengths (Scharmer *et al.*, 2002).

USO is currently involved in building a Multi-Application Solar Telescope (MAST) for solar observations. As is the case with any of the modern solar telescopes, the MAST would be equipped with an adaptive optics system that operates in the Visible and Near IR (<http://www.prl.res.in/~uso/mast.pdf>). As a preparatory exercise, a prototype project for developing and demonstrating the feasibility of a Solar Adaptive Optics (SAO) system at USO was started in January 2003. As a preparatory exercise, a prototype project for developing and demonstrating the feasibility of SAO system at USO is under progress.

As far as the laboratory demonstration of the Adaptive optics system is concerned, in the first phase, an Image Stabilization System (ISS: tip-tilt system) that corrects for the lowest order wave-front aberration has been demonstrated. In this Chapter, we describe the details of this proto-type ISS which has been successfully demonstrated (Sridharan *et al.*, 2005; Kumar *et al.*, 2005). In the

second phase, the development of an Adaptive optics system that includes wave-front sensing and correction using a membrane mirror is in progress (Bayanna *et al.*, 2005, 2007).

Our ISS consists of a high speed camera (955 frames per second) and frame grabber system for sensing the overall tilt of the wave-front, a piezo-controlled mirror for correcting the tilt and an Intel Pentium 4 computer operating on Linux platform for controlling various devices. The software for operating the system is based on C-language. The first results indicating the capability of the system to limit the image motion within a fraction of the diffraction limit are presented. The system has a closed loop correction bandwidth in the range of 70 to 100 Hz. The root mean square image motion in the closed loop is about 0.1 arc-sec and is better than that in the open loop operation by a factor of 10 to 20. The hardware and software developments and key issues concerning optimum system performance have been addressed along with possible future improvements. The images obtained with a ‘science camera’ through G-band filter ( $\lambda = 430.2$  nm ; pass-band = 1 nm) shows improvement in  $r_0$  in closed loop relative to open loop observations.

### **6.1.3 Study of enhanced velocity signals observed during major solar flares**

It is well known that solar flares release large amount of energy within few minutes to hours. Apart from high energy radiation, it also produces a large amount of energetic particles which move at high speeds. Several researchers have put their effort to understand the mechanism involved in these explosive events occurring in the solar atmosphere. The major aspect of such investigations involved looking for changes in magnetic flux, magnetic shear, magnetic helicity and magnetic energy etc. before and after the flares.

Apart from searching for the cause of the flare, people have also looked at the consequence of the flares in the solar atmosphere and one chief thrust area has been the study of the effect of a flare on solar oscillations, especially on the

$p$ -mode oscillation frequency and power in the associated active region. These global oscillations are present on the Sun all the time, with maximum power in the 3 mHz frequency band for velocity oscillations. These global modes are excited by the turbulence in the convective layer. However, reduced velocity power in 3 mHz band is seen in sunspots as compared to the quiet part of the Sun, whereas enhancement in high frequency power in these active regions have been reported (Hindman and Brown, 1998; Venkatakrisnan, Kumar, and Tripathi, 2002) during non-flaring conditions. Sunspots are thus known to absorb the  $p$ -mode power (Braun, Duvall, and LaBonte, 1987), however this situation could well be altered during the flares.

Wolff (1972) suggested that large solar flares can stimulate the free modes of oscillation of the entire Sun. Haber *et al.* (1988) have reported that there is an average increase in the power of intermediate degree  $l$ , after the flare. At the same time, Braun and Duvall (1990) could not detect the excitation of acoustic waves from an X- class flare. Kosovichev and Zharkova (1998) have reported signature of seismic waves (solar quakes) during solar flare. Following this result, Donea, Braun and Lindsey (1999) found an acoustic source associated with a flare using seismic images. They found a considerable flare induced acoustic power in 3.5 mHz band. The flare also induced power in 6 mHz band. Further, they report that 6 mHz flare signature lags the 3.5 mHz by  $\sim 4$  min. Application of ring diagram analysis technique to several flare producing active regions showed that power of  $p$ -modes appear to be larger when compared to that in non-flaring regions of similar magnetic field strength (Ambastha, Basu, and Antia, 2003). Using helioseismic holography technique, Donea and Lindsey (2005) have reported emission of seismic waves from large solar flares which have occurred in active region NOAA 10486 on 2003 October 28 and 29. They found many compact acoustic sources associated with the foot-points of the coronal loops.

In this Chapter, we study the enhanced velocity signals in NOAA active regions 10486 and 9415 which appear during flares, and are co-temporal with the GOES soft X-ray flux. These active regions have produced major X-class

flares and hence are ideal sites for studying the effect of flares on velocity oscillations. Also, we present each of the selected events in decreasing order of flare strength. We have used Fast Fourier Transform based power spectral images to study the acoustic power in the active region in different frequency regimes during the flare event. The enhanced velocity signals appeared during the rise time of the GOES soft X-ray flux. These signals are located close to the vicinity of the hard X-ray source regions as observed with RHESSI. The power maps of the active region show enhancement in the frequency regime 5–6.5 mHz, while there is feeble or no enhancement of these signals in 2–4 mHz frequency band.

The hard X-ray emissions have their origin from the non-thermal bremsstrahlung of accelerated electrons in solar flares (Brown, 1971; Hudson, 1972). The large flux of non-thermal energetic electrons can heat the chromospheric plasma (Fisher, Canfield, and McClymont, 1985), and this sudden heating causes thermal instability which expands the chromospheric plasma to the temperature of the corona. This will happen when the hydrodynamic expansion time scale is larger than the heating time scale (Fisher, Canfield, and McClymont, 1985). Further, the increase in plasma pressure will cause explosive evaporation of the chromospheric plasma into the corona and then downward settlement as chromospheric condensation (Fisher, 1989), as has been evidenced in red wing asymmetry of  $H\alpha$  line profiles. The downward propagating plasma and shock waves ahead of plasma were assumed to be the agents delivering momentum to the photosphere which can result in observed excited acoustic signature. The excited velocity signals appear as red-shifted in those locations for short duration.

The global  $p$ -modes that are observed to be always present on the Sun are excited by turbulence in the convection zone (Goldreich and Kumar, 1990, and references therein, Stein and Leibacher, 1974) and are modified in active regions due to absorption of acoustic waves by magnetically inhomogeneous media (Braun, Duvall and LaBonte, 1988). In addition to this continuous source of excitations, transient phenomena like flares can contribute additional

energy to these modes. Even if a small fraction of the energy released by flare is transferred to oscillations in active region, it can increase the amplitude of oscillation significantly. However, the photosphere and magnetic field in active region provides a boundary condition for the  $p$ -modes and any source of additional energy from the external agent may affect these oscillations for short spans, as these can not be sustained by the cavity. This can lead to the enhanced velocity oscillations during flare events. Infact, the enhancement of power in 3 min band is a clear indication of the “wake” (Rae and Roberts, 1982) of the chromospheric response at the acoustic cut-off frequency (Lamb, 1932) to a pressure impulse .

On the other hand, there are some evidences about the Ni I 6768 Å line profile turning into emission during strong X-class flares (Qiu and Gary, 2003). The non-thermal electrons can produce heating at the foot-points of the magnetic field lines. Using non-LTE calculations, Ding, Qiu and Wang (2002) found that the Ni I 6768 Å line may appear in emission in the presence of strong electron beam in a cool atmosphere like sunspots. They also found that even if the atmosphere gets hot in the absence of energetic particles, the line profile may not turn into emission. If the line profile turns into emission during the flare, then there is a possibility of sudden change in the velocity signal. This change in velocity signal persists till its source dies down. To examine this, one needs to have the spectral line information of line from which the Dopplergrams have been obtained. The future space based missions like Solar-B may help in this context.

#### **6.1.4 First detection of photospheric “Doppler ribbons” during an intense 4B/X17.2 solar flare**

The Chapter V describes the first detection of a photospheric “Doppler ribbons” associated with an intense 4B/X17.2 solar flare. The “super active region” NOAA Active Region 10486 which appeared on the solar disk in October 2003 produced lot of space weather related activity. This was one of the largest flares of solar cycle 23, which occurred near the Sun’s center and

produced extremely energetic emission almost at all wavelengths from  $\gamma$ -ray to radio-waves. The flare was associated with a bright/fast-halo Earth directed CME, strong type II, type III and type IV radio bursts, and an intense radio burst. This flare was observed with space based solar Observatories viz., SOHO, TRACE and several other ground based Observatories including USO and ARIES in India in  $H\alpha$  wavelength. Here, we report the first detection of an interesting solar photospheric phenomenon, viz. “Doppler ribbons” or localized velocity enhancements, which were seen to accompany the solar chromospheric H-alpha ribbons during super flare. These velocity enhancements exactly match the H-alpha brightness enhancements in space, and are delayed by approximately 1 minute in time. We interpret these Doppler enhancements as due to plasma shock being launched at the site of explosive chromospheric evaporation, which reaches the photosphere after approximately 1 minute. The excitation of 3 minute oscillations in the photosphere after the flare, as discussed in the Chapter IV, is a clear signature of the response of the solar atmosphere to a pressure pulse in the form of a “wake”. Such Doppler ribbons have not been detected following weaker flares. Thus, the circumstance of the abnormally high electron flux available in the 4B/X17.2 flare of 28 October 2003, has given rise to this rare phenomenon.

## 6.2 Future Directions

### 6.2.1 High resolution observations with MAST and SOLAR-B/ Hinode

The ISS integrated with Shack Hartman Wavefront Sensor (SHWFS) and deformable mirror is planned to be deployed on the 50 cm Multi-Application Solar Telescope (MAST) proposed to be installed at the lake site of USO. We are planning to have a spectrograph, a filtergraph and a polarimeter as back-end instruments for MAST. Our solar adaptive optics system will allow us to obtain good quality images and spectra using this 50 cm telescope. MAST is



expected to be operational by the mid of the year 2009. This period will be in the ascending phase of solar cycle 24. Thus, MAST will be able to observe the evolution of inhomogeneities as the cycle progresses. From our study, we have realized that lake with water supports good seeing, so we hope to have good results from MAST equipped with an adaptive optics system with the lake filled with water. The local government has also planned to maintain the water level in the lake through ambitious water supply projects for Udaipur. Thus, we shall be able to observe more “interesting events” taking place in the solar atmosphere as the next solar cycle 24 progresses.

It is well known that a 50 cm aperture space telescope named SOLAR-B/Hinode has started observing the Sun in visible and X-ray wavelength regions since November 2006. The images taken with this telescope is looking into the fine details of the Sun’s structure. The simultaneous data from Hinode and MAST will be used in future studies related to solar atmosphere.

# Appendix:A

## Code for estimating the image motion in Image Stabilization System:

Sum of absolute differences (SAD) method is used to estimate the shifts of the subsequent images with respect to the reference image. MMX instructions are used to implement the code. The following instruction set shows the code for estimating the SAD for the given shift vectors  $dx$  and  $dy$ . After estimating the SAD for all possible shifts in all directions, parabolic interpolation is used to get the image motion in sub-pixel accuracy. The following code segment estimates the shifts within the central  $64 \times 64$  pixels of the CCD window. Similarly, the code can be extended to bigger window sizes.

```
int sae(int dx, int dy)
{
    int is, iy; /* loop counters */
    int csae = 0; /* accumulators for difference */
    uint32_t c1 = 0;
    uint8_t *ip, *rp; /* pointers to appropriate rows */

    for (iy=96;iy<NY-96;iy++) {
        ip = &crimag[iy*NX+96];
        rp = &refim[(iy+dy)*NX+96+dx];
        asm ("movq (%1), %%mm1 \n\t"
            "psadbw (%2), %%mm1 \n\t"
            "movq 8(%1), %%mm0 \n\t"
            "psadbw 8(%2), %%mm0 \n\t"
            "paddw %%mm0, %%mm1 \n\t"
            "movq 16(%1), %%mm0 \n\t"
            "psadbw 16(%2), %%mm0 \n\t"
```

```

“paddw %%mm0, %%mm1 \n\t”
“movq 24(%1), %%mm0 \n\t”
“psadbw 24(%2), %%mm0 \n\t”
“paddw %%mm0, %%mm1 \n\t”
“movq 32(%1), %%mm0 \n\t”
“psadbw 32(%2), %%mm0 \n\t”
“paddw %%mm0, %%mm1 \n\t”
“movq 40(%1), %%mm0 \n\t”
“psadbw 40(%2), %%mm0 \n\t”
“paddw %%mm0, %%mm1 \n\t”
“movq 48(%1), %%mm0 \n\t”
“psadbw 48(%2), %%mm0 \n\t”
“paddw %%mm0, %%mm1 \n\t”
“movq 56(%1), %%mm0 \n\t”
“psadbw 56(%2), %%mm0 \n\t”
“paddw %%mm0, %%mm1 \n\t”
“movd %%mm1,%0 \n\t”
“emms \n\t”
: “=g” (c1)
: “r” (rp), “r” (ip)
);
csae = csae + c1; }
return csae;
*****

```

# Appendix:B

## Theory of controllers:

**Definitions of  $P$ ,  $I$  &  $D$ :** A control system (Murrill, 1981) can be represented by the block diagram shown in the sketch below. In our case, the input to the controller (or the error signal,  $e$ ) is the residual shift  $X(t)$  in the image plane and the output of the controller (or manipulated variable,  $m$ ) is voltage ( $V$ ) being applied to the actuators.

In a Proportional controller, the output voltage is proportional to the input or the shift. Hence,

$$V \propto X \quad (6.2.1)$$

or,

$$V = P.X \quad (6.2.2)$$

Where,  $P$  is a constant known as “Proportional gain” of the system.

In an Integral controller, the rate of change of its output voltage is proportional to the shift in the pixels.

$$(dV/dt) \propto X \quad (6.2.3)$$

or,

$$V = I \int X.dt \quad (6.2.4)$$

where,  $I$  is a constant known as “Integral constant”.

In a Derivative Controller, the output voltage is proportional to the rate of change in shifts (in pixel units).

$$V \propto (dX/dt) \quad (6.2.5)$$

or,

$$V = D.(dX/dt) \quad (6.2.6)$$

where,  $D$  is a constant known as “Derivative constant”.

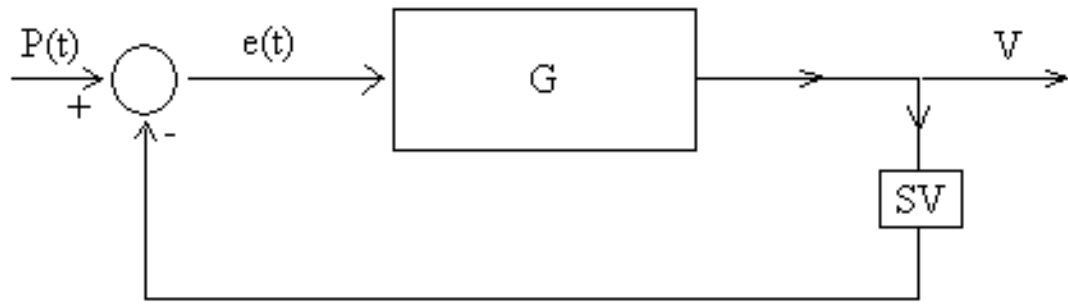


Figure 6.1: Block diagram of a feedback controller:  $P(t)$  is the perturbation,  $e(t)$  is the error signal,  $G$  is the gain of the system,  $SV$  is the sensed value and  $V$  is the controller output.

We are using *PID* type control in the Image Stabilization System.

\*\*\*\*\*

# Bibliography

- [1] Ambastha, A. (2006) Photospheric, chromospheric and helioseismic signatures of a large flare in super-active region NOAA 10486, *J. Astrophys. Astron.*, 27, 255-265.
- [2] Ambastha, A., Basu, S., and Antia, H. M. (2003) Flare-induced excitation of solar  $p$ -modes, *Solar Phys.*, 218, 151-172.
- [3] Ambastha, A., Hagyard, M. J., and West, E. A. (1993) Evolutionary and flare-associated magnetic shear variations observed in a complex flare-productive region, *Solar Phys.*, 148, 277-287.
- [4] Ballesteros, E., Collados, M., Bonet, J. A., Lorenzo, F., Viera, T., Reyes, M., and Rodriguez Hidalgo, I. (1996), Two-dimensional, high spatial resolution, solar spectroscopy using a correlation tracker. I. Correlation tracker description, *Astron. Astrophys. Supp. Ser.*, 115, 353.
- [5] Beckers, J. M., Liu, Z., Jin, Z. (2003) ATST seeing monitor: February 2002 observations at Fuxian lake, *SPIE*, 4853, 273-284.
- [6] Beckers, J. M. (2001) A seeing monitor for solar and other extended object observations, *Exp. Astron.*, 12, 1-20.
- [7] Beckers, J. M., Mason, J. (1998), Site surveys for a large solar telescope, *SPIE*, 3352, 858-867.
- [8] Beckers, J. M., Leon E., Mason, J., Wilkins, L. (1997) Solar scintillometry: Calibration of signals and its use for seeing measurements, *Solar Phys.*, 176, 23-36.

- [9] Beckers, J.M. (1993), Adaptive Optics for Astronomy: Principles, Performance, and Applications, *Ann. Rev. Astron. Astrophys.*, 31, 13-62.
- [10] Bell, E. F., Hill, F., Harvey, J. W. (1999), Estimation of seeing quality using low-resolution solar image data, *Solar Phys.*, 185, 15-34.
- [11] Bhatnagar, A. (2006), Why Study the Sun?, *J. Astrophys. Astron.*, 27, 59-78.
- [12] Bhatnagar, A., and Livingston, W. (2005), Fundamentals of Solar Astronomy, *World Scientific Publishing Company, Singapore*.
- [13] Bogachev, S. A., Somov, B. V., Kosugi, T., and Sakao, T. (2005), The motions of the hard X-ray sources in solar flares: Images and statistics, *Astrophys. J.*, 630, 561-572.
- [14] Braun, D. C., and Duvall, Jr., T. L. (1990),  $p$ -mode absorption in the giant active region of 10 March, 1989, *Solar Phys.*, 129, 83-94.
- [15] Braun, D. C., Duvall, Jr., T. L. and Labonte, B. J. (1988), The absorption of high-degree  $p$ -mode oscillations in and around sunspots, *Astrophys. J.*, 335, 1015-1025.
- [16] Braun, D. C., Duvall, Jr., T. L. and Labonte, B. J. (1987), Acoustic absorption by sunspots, *Astrophys. J.*, 319, L27-31.
- [17] Brown, J. C. (1971), The deduction of energy spectra of non-thermal electrons in flares from the observed dynamic spectra of hard X-ray bursts, *Solar Phys.*, 18, 489-502.
- [18] Canfield, R. C., Zarro, D. M., Metcalf, T. R., and Lemen, J. R. (1990), Momentum balance in four solar flares, *Astrophys. J.*, 348, 333-340.
- [19] Corripio, A. B. (2000), Tuning of Industrial Control Systems, *Instrument Society of America, Research Triangle park, N.C., USA*.

- [20] Ding, M. D., Qiu, J., and Wang, H. (2002), Non-LTE calculation of the Ni I 676.8 nanometer line in a flaring atmosphere , *Astrophys. J.*, 576, L83-86.
- [21] Domingo, V., Fleck, B., and Poland, A. I. (1995), The SOHO Mission An overview, *Solar Phys.*, 162, 1-37.
- [22] Donea, A. -C, and Lindsey, C. (2005), Seismic emission from the solar flares of 2003 October 28 and 29, *Astrophys. J.*, 630, 1168-1183.
- [23] Donea, A. -C, Braun, D. C., and Lindsey, C. (1999), Seismic images of a solar flare, *Astrophys. J.*, 513, L143-146.
- [24] Fisher, G. H., Canfield, R. C., and McClymont, A. -N. (1985), Flare loop radiative hydrodynamics Part Six Chromospheric evaporation due to heating by nonthermal electrons, *Astrophysical J.*, 289, 425-433.
- [25] Fisher, G. H. (1989), Dynamics of flare-driven chromospheric condensations, *Astrophys. J.*, 346, 1019-1029.
- [26] Fried, D. L. (1966a), Limiting resolution looking down through the atmosphere, *J. Opt. Soc. Am.*, 56, 1380-1384.
- [27] Fried, D. L. (1966b), Optical resolution through a randomly inhomogeneous medium for very long and very short exposures, *J. Opt. Soc. Am.*, 56, 1372-1379.
- [28] Fried, D. L. (1965), Statistics of a geometric representation of wavefront distortion, *J. Opt. Soc. Am.*, 55, 1427-1435.
- [29] Goldreich, P. and Kumar, P. (1990), Wave generation by turbulent convection, *Astrophys. J.*, 363, 694-704.
- [30] Goode, P. R., Wang, H., Marquette, W. H., Denker, C. (2000), Measuring seeing from solar scintillometry and the spectral ratio technique, *Solar Phys.*, 195, 421-431.



- [31] Gopalswamy, N. (2005), Introduction to violent Sun-Earth connection events of October-November 2003, *J. Geophys. Res.*, 110, A09S00 1-6, doi 10.1029/2005 JA011268.
- [32] Gosain, S., Venkatakrishnan, P., Venugopalan, K. (2006), Design and status of a Solar Vector Magnetograph (SVM-I) at Udaipur Solar Observatory, *J. Astrophys. Astron.*, 27, 285-292.
- [33] Haber, D. A., Toomre, J., and Hill, F., Gough, D. O. (1988), Local effects of a major flare on solar five-minute oscillations, *in Seismology of the Sun and Sun-like stars*, ESA-SP286, 301-304.
- [34] Hagyard, M. J., Stark, B. A., and Venkatakrishnan, P. (1999), A search for vector magnetic variations associated with the M-class flares of 10 June 1991 in AR 6659, *Solar Phys.*, 184, 133-147.
- [35] Hindman, B. W., and Brown, T. M. (1998), Acoustic power maps of solar active regions, *Astrophys. J.*, 504, 1029-1033.
- [36] Hill, F. *et al.* (2006), Site testing for the Advance Technology Solar Telescope, *SPIE*, 6267, 59-63.
- [37] Hudson, H. S. (1972), Thick-target processes and white light flares, *Solar Phys.*, 24, 414-428.
- [38] Keller, C. U., Plymate, C., and Ammons, S. M. (2003), Low-cost solar adaptive optics in the infrared, in S. Keil, and S. Avakyan (eds.) *Innovative Telescopes and Instrumentation for Solar Astrophysics*, *SPIE*, 4853, 351-359.
- [39] Kolmogorov, A. N. (1941), *Dan. S. S. S. R.*, 30, 229.
- [40] Kosovichev, A. G. (2006), Properties of flares-generated seismic waves, *Solar Phys.*, 238, 1-11.
- [41] Kosovichev, A. G., and Zharkova, V. V. (1998), X-ray flare sparks quake inside the Sun, *Nature*, 393, 317-319.

- [42] Krucker, Sam, Hurford, G. J., and Lin, R. P. (2003), RHESSI hard X-ray imaging spectroscopy of the large gamma-ray flare of 2002 July 23, *Astrophys. J.*, 595, L107-110.
- [43] Kumar, Brajesh, Venkatakrishnan, P., Raja Bayanna, A., and Venugopalan, K. (2007), Site characterization using solar H $\alpha$  images, *Solar Phys.*, 241, 427-437.
- [44] Kumar, Brajesh and Ravindra, B. (2006), Analysis of enhanced velocity signals observed during solar flares, *J. Astrophys. Astron.* 27, 425-438.
- [45] Kumar, Brajesh, Sridharan, R., Raja Bayanna, A., and Venkatakrishnan, P. (2005), Preliminary results on the calibration and control of an Adaptive optics system, *Bull. Astron. Soc. India*, 33, 413.
- [46] Labeyrie, A. (1976), High-resolution techniques in optical astronomy, in E. Wolf (ed.) *Progress in Optics* XIV, 47, North-Holland, Amsterdam.
- [47] Lamb, H. (1932), *Hydrodynamics* (Cambridge: Cambridge University Press).
- [48] Lara, A., Gopalswamy, N., and DeForest, C. (2000), Change in photospheric magnetic flux during coronal mass ejections, *GeoPhys. Res. Lett.*, 27, 1435-1439L.
- [49] Lin, R. P. *et al.* (2002), The Reuven Ramaty High-Energy Spectroscopic Imager (RHESSI), *Solar Phys.*, 210, 3-32.
- [50] Li, H., Sakurai, T., Ichimoto, K., and Ueno, S. (2000), Magnetic field evolution leading to solar flares II. Cases with high magnetic shear and flare-related shear changes, *Publ. Astron. Soc. Japan*, 52, 483-497.
- [51] Mathew, S. K., Bhatnagar, A., Prasad, C. D., Ambastha, A. (1998), Fabry-perot filter based solar video magnetograph, *Astron. Astrophys. Suppl. Ser.*, 133, 285-292.

- [52] Metcalf, T. R., Leka, K. D., and Mickey, D. L. (2005), Magnetic free energy in NOAA Active Region 10486 on 2003 October 29, *Astrophys. J.*, 623, L53-56.
- [53] Moon, Y. -J., *et al.* (2002), A statistical study of two classes of CMEs, *Astrophys. J.*, 581, 694-702.
- [54] Murril, P. W. (1981), Fundamentals of process control theory, *Instrument Society of America, Research Triangle park, N.C., USA*.
- [55] Niblack, W. (1986), An Introduction to Digital Image Processing, *Prentice Hall International, New Jersey, USA*.
- [56] Press, H. W., Teukolsky, S. A., Vetterling, W. T., and Flannery, B. P. (1993), Numerical Recipes in FORTRAN; The art of scientific computing, *Cambridge University Press, New Delhi, India*.
- [57] Qiu, J., and Gary, D. E. (2003), Flare-related magnetic anomaly with a sign reversal, *Astrophys. J.*, 599, 615-625.
- [58] Rae, I. C. and Roberts, B. (1982), Pulse propagation in a magnetic flux tube, *Astrophys. J.*, 256, 761-767.
- [59] Raja Bayanna, A. , Kumar, Brajesh, Louis, R. E., Venkatakrishnan, P., and Mathew, S. K. (2007), *J. Astrophys. Astron.*, submitted.
- [60] Raja Bayanna, A., Mathew, Shibu K., Venkatakrishnan, P., Kumar, Brajesh, and Sridharan, R. (2005), in *International conference on Optics and Opto-electronics*, IRDE-DRDO, Dehradun, India.
- [61] Rao, C. H., Jing, W. H., Ling, N., Beckers, J. M. (2001), An analysis of the observed contrast of solar surface granulations, *Ch. Astron. Astrophys.*, 25, 439-445.
- [62] Rimmele, T.R., Balasubramaniam, K.S., and Radick, R.R., (1999), eds. High Resolution Solar Physics: Theory, Observations, and Technique, *ASP Conf. Ser.*, Vol. 183.

- [63] Rimmele, T. (2000), Solar Adaptive optics, in ed. (P. L. Wizinowich) *Adaptive Optical Systems Technology, SPIE* **4007**, 218-231.
- [64] Roddier, F. (1981), The effects of atmospheric turbulence in optical astronomy, in Wolff, E. (ed.) *Progress in Optics*, 19, 281-376.
- [65] Roggeman, M.C., Welsh, B.M., and Fugote, R.Q. (1997), Improving the resolution of ground-based telescopes, *Rev. of Modern Phys.*, 69, 2, 437-504.
- [66] Rutten, R. J., Hammerschlag, R. H., Bettonvil, F. C. M., Sutterlin, P., de Wijn, A. G. (2004), DOT tomography of the solar atmosphere .I. Telescope summary and program definition, *Astron. Astrophys.*, 413, 1183-1189.
- [67] Sakurai, T., Shibata, K., Ichimoto, K., Tsuneta, S., and Acton, Loren W. (1992), Flare-related relaxation of magnetic shear as observed with the soft X-ray telescope of YOHKOH and with vector magnetographs, *Publ. Astron. Soc. Japan*, 44, L123-127.
- [68] Scharmer, G. B., Shand, M., Löfdahl, M. G., Dettori, P. M., and Wang, W. (2000), Workstation based solar/ stellar Adaptive optics system, *SPIE*, 4007, 105.
- [69] Scharmer, G. B., Gudiksen, B. V., Kiselman, D., Lofdahl, M. G., van der Voort, H. M. R. (2002), Dark cores in sunspot penumbral filaments, *Nature*, 420, 151-153.
- [70] Scharmer, G. B., Dettori, P., Lofdahl, M. G., and Shand, M. (2003), Adaptive optics system for the new swedish solar telescope, in S. Keil, and S. Avakyan (eds.) *Innovative Telescopes and Instrumentation for Solar Astrophysics, SPIE*, 4853, 370-380.
- [71] Scherrer, P. H. *et al.* (1995), The solar oscillations investigation Michelson Doppler Imager, *Solar Phys.*, 162, 129-188.

- [72] Seykora, E. J. (1993), Solar scintillation and the monitoring of solar seeing, *Solar Phys.*, 145, 389-397.
- [73] Solanki, S. K. and Ruedi, I. (2003), Spatial and temporal fluctuation in sunspots derived from MDI data, *Astron. Astrophys.*, 411, 249-256.
- [74] Sridharan, R., Bayanna, A. R., Kumar, Brajesh, and Venkatakrishnan, P. (2005), An image stabilization system for solar observations, *Bull Astron. Soc. India*, 33, 414.
- Sridharan, R., and Raja Bayanna, A. (2004), Low-order adaptive optics for the meter aperture solar telescope of Udaipur Solar Observatory, *SPIE*, 5171, 219-230.
- [75] Sridharan, R., Raja Bayanna, A., Srivastava, N., Kumar, B., Ravindra, B., Gupta, S. K., Jain, N., Ambastha, A., and Venkatakrishnan, P. (2003), Performance evaluation of an adaptive optics system, *Bull. Astron. Soc. India*, 31, 455.
- [76] Sridharan, R., Raja Bayanna, A., and Venkatakrishnan P. (2003), in W. Brandner, and M.Kasper (eds.) “*Science with Adaptive Optics*”, *ESO Astrophysics Symposia*, Proceedings of the ESO workshop held at Garching, Germany, 16-19 September 2003, Springer, 132.
- [77] Sridharan, R., Venkatakrishnan, P., Verma, V. K. (2002), Estimation of Fried’s parameter from specklegrams of solar features, *Solar Phys.*, 211, 395-406.
- [78] Srivastava, N., Mathew, S. K. (1999), A digital imaging multi-slit spectrographs for measurement of line-of-sight velocities on the Sun, *Solar Phys.*, 185, 61-68.
- [79] Stein, R. F., and Leibacher, J. (1974), Waves in the solar atmosphere, *Ann. Rev. Astron. Astrophys.*, 12, 407-435.

- [80] Uddin, W., Chandra, R., and Ali, S. S. (2006), Extremely energetic 4B/X17.2 flare and associated phenomena, *J. Astrophys. Astron.*, 27, 267-276.
- [81] Venkatakrishnan, P., Kumar, B., and Tripathy, S. C. (2002), Variation of acoustic power with magnetic field as seen in GONG+ data, *Solar Phys.*, 211, 77-81.
- [82] Venkatakrishnan, P. *et al.* (2004), *MAST document*: <http://www.prl.res.in/~uso/mast.html>.
- [83] von der Lühe, O., Soltau, D., Berkefeld, T., and Schelenz, T. (2003), Kaos: Adaptive optics system for the vacuum tower telescope at teide observatory, in eds. (S. Keil, and S. V. Avakyan) *Innovative Telescopes and Instrumentation for Solar Astrophysics*, *SPIE*, 4853, 351-359.
- [84] von der Lühe, O. (1993), Speckle imaging of solar small scale structure. I - Methods, *Astron. Astrophys.*, 268, 374-390.
- [85] von der Lühe, O. (1984), Estimating Fried's parameter from a time series of an arbitrary resolved object imaged through atmospheric turbulence, *J. Opt. Soc. Am.*, A1, 510-519.
- [86] Wang, T., Xu, A., and Zhang, H. (1994), Evolution of vector magnetic fields and vertical currents and their relationship with solar flares, *Solar Phys.*, 155, 99-112.
- [87] Wolff, C. L. (1972), Free oscillations of the Sun and their possible stimulation by solar flares, *Astrophys. J.*, 176, 833-841.
- [88] Young, A. T. (1971), Seeing and Scintillation, *Sky and Telescope*, September, 139.
- [89] Zarro, D. M., Canfield, R. C., Strong, K. T., and Metcalf, T. R. (1988), Explosive plasma flows in a solar flare, *Astrophys. J.*, 324, 582-589.

# List of Publications

## I. Papers in Journals:

1. *Site characterization using solar H $\alpha$  images*, Brajesh Kumar, P. Venkatakrishnan, A. Raja Bayanna, and K. Venugopalan, *Solar Phys.*, **241**, 427-437 (2007).
2. *Analysis of enhanced velocity signals observed during solar flares*, Brajesh Kumar, and B. Ravindra, *J. Astrophys. Astron.*, **27**, 425-438 (2006).

## II. In Conference Proceedings:

1. *An image stabilization system for solar observations*, R. Sridharan, A. Raja Bayanna, R. E. Louis, Brajesh Kumar, P. Venkatakrishnan, and S. K. Mathew, *SPIE*, submitted (2007).
2. *Development of a low-order Adaptive optics system at Udaipur Solar Observatory*, A. Raja Bayanna, Brajesh Kumar, R. E. Louis, P. Venkatakrishnan, and S. K. Mathew, *J. Astrophys. Astron.*, submitted (2007).
3. *On the enhanced velocity signals observed during solar flares*, Brajesh Kumar, P. Venkatakrishnan, and K. Venugopalan, in “*SOHO 18/GONG 2006/HELAS I: Beyond the spherical Sun*”, eds: M. Thompson, and K. Fletcher, **ESA SP-624**, 65-69 (2006).
4. *Development of a low-order Adaptive optics system at Udaipur Solar Observatory*, A. Raja Bayanna, S. K. Mathew, P. Venkatakrishnan, Brajesh Kumar, and R. Sridharan, in “*International conference on Optics and Optoelectronics*”, held at IRDE (DRDO), Dehradun, India, **PP-AO-1** (2005).
5. *A study of the effect of flare on acoustic oscillations using wavelet analysis*, B. Ravindra, and Brajesh Kumar, *Bull. Astron. Soc. India*, **33**, 355 (2005).
6. *An image stabilization system for solar observations*, R. Sridharan, A. Raja Bayanna, Brajesh Kumar, P. Venkatakrishnan, *Bull. Astron. Soc. India*, **33**, 414 (2005).
7. *Preliminary results on the calibration and control of an Adaptive optics system*, Brajesh Kumar, R. Sridharan, A. Raja Bayanna, and P. Venkatakrishnan, *Bull. Astron. Soc. India*, **33**, 413 (2005).